

Alma Mater Studiorum – Università di Bologna

DOTTORATO DI RICERCA IN

Meccanica e Scienze Avanzate dell'Ingegneria

Ciclo XXXI

**Settore Concorsuale: 09/C1**

**Settore Scientifico Disciplinare: ING-IND/08**

Development and experimental validation of a knock-induced damage model and real-time implementation of model-based strategies to control knock intensity in boosted gasoline engines

**Presentata da**

**Dott. Nahuel Rojo**

**Coordinatore Dottorato**

**Prof. Ing. Marco Carricato**

**Supervisore**

**Prof. Ing. Nicolò Cavina**

**Esame finale anno 2019**

## Abstract

This PhD thesis reports the main activities carried out during the 3 years long “Mechanics and advanced engineering sciences” course, at the Department of Industrial Engineering of the University of Bologna. The research project title is “Development and analysis of high efficiency combustion systems for internal combustion engines” and the main topic is *knock*, one of the main challenges for boosted gasoline engines. Through experimental campaigns, modelling activity and test bench validation, 4 different aspects have been addressed to tackle the issue.

The main path goes towards the definition and calibration of a knock-induced damage model, to be implemented in the on-board control strategy, but also usable for the engine calibration and potentially during the engine design.

Ionization current signal capabilities have been investigated to fully replace the pressure sensor, to develop a robust on-board close-loop combustion control strategy, both in knock-free and knock-limited conditions. Water injection is a powerful solution to mitigate knock intensity and exhaust temperature, improving fuel consumption; its capabilities have been modelled and validated at the test bench.

Finally, an empiric model is proposed to predict the engine knock response, depending on several operating condition and control parameters, including injected water quantity.



# Index of contents

Introduction.....	1
<b>1 Knock Damage.....</b>	<b>2</b>
1.1 Introduction.....	2
1.2 Literature review .....	2
1.3 Experimental Setup .....	3
1.3.1 Test Bench .....	4
1.3.2 Piston Analysis .....	4
1.4 Experimental Data .....	8
1.4.1 Engine boundary and control parameters.....	8
1.4.2 Measured induced damage on pistons .....	10
1.5 Physical overview and experiment design .....	12
1.5.1 Knock effects .....	12
1.5.2 Piston temperature .....	12
1.5.3 Spark advance, heat transfer and knock intensity .....	12
1.6 1-D piston temperature model.....	15
1.6.1 Oil convection coefficient estimation.....	20
1.6.2 Thickness estimation .....	21
1.6.3 Specific thermal flux correlation .....	22
1.6.4 Piston temperature model calibration results .....	24
1.6.5 Oil pressure variation effect .....	27
1.6.6 Piston skin temperature .....	28
1.7 Knock damage model .....	31
1.7.1 Damage model calibration results.....	33
1.8 Control implementation .....	35
1.9 Validation.....	37
1.9.1 Piston temperature model .....	38
1.9.2 Damage model.....	40
1.9.3 Heat flow estimation .....	41
1.10 Conclusions.....	43
1.11 References .....	44
<b>2 ION-based combustion control .....</b>	<b>46</b>
2.1 Introduction.....	46
2.2 Ionization current signal.....	47
2.2.1 Ion sensing circuit.....	47
2.2.2 Ionization .....	48
2.2.3 Knock .....	48

2.2.4 Other Ion Signal Features .....	49
2.3 Experimental setup.....	49
2.4 Spark Advance Controller Development .....	50
2.4.1 In-Cylinder Pressure Controller Layout .....	51
2.4.2 Ion Current Controller Development .....	52
2.5 Experimental Validation .....	54
5.1 In-cylinder Pressure Controller Experimental Results.....	54
2.5.2 Ion Current Controller Experimental Results .....	56
2.5.3 Comparison between Pressure- and Ion-based Control .....	56
2.6 Pre-Ignition detection.....	57
2.6.1 Test 1 .....	58
2.6.2 Dwell integral index.....	59
2.6.3 Test 2 .....	61
2.6.4 Pre-Ignition Phase.....	63
2.7 Conclusions.....	64
2.8 References .....	65
<b>3 Water Injection .....</b>	<b>67</b>
3.1 Introduction.....	67
3.2 Water injection and knock model .....	67
3.2.1 Model layout.....	68
3.2.2 Water injection modelling parameters .....	68
3.2.3 Knock model .....	71
3.2.4 Modelling results .....	74
3.3 Experimental tests.....	75
3.3.1 Experimental setup.....	76
3.3.2 Experimental results.....	77
3.4 Conclusions.....	79
3.5 References .....	80
<b>4 Knock Model .....</b>	<b>81</b>
4.1 Introduction.....	81
4.2 Experimental tests.....	82
4.3 MAPO statistical analysis.....	83
4.4 Knock model .....	85
4.4.1 Engine speed variation .....	87
4.4.2 MAPO50 Calculation.....	89
4.4.3 Lambda Multiplier .....	91
4.4.4 Water Injection Multiplier .....	92
4.5 Knock Model Results .....	94
4.5.1 Log-normal PDF Parameters.....	94

4.6 Conclusions.....	95
4.7 References.....	95
4.8 Appendix.....	96
Conclusions.....	99

## Introduction

Knocking combustion is one of the major limiting factors for the efficiency of spark ignited engines. This kind of anomalous combustion is triggered by high pressure and temperature levels and its occurrence is carefully avoided (or tolerated in very small extent) since it is associated to dramatic consequences on the engine.

Because of its stochastic nature, which is reflected in an unfamiliar statistical distribution, because of the difficulties during the measurement, which is heavily affected by the sensor position and frequency response, by the engine concept, by the index definition, *knock* is often surrounded by a halo of mystery. For the same reasons, it can be a very challenging topic to deal with, especially in a research context. The first chapter, describes the current state of the central research activity carried out during these 3 years, which tries to understand, quantify and predict the undesired and damaging effects induced by knocking combustions. This allows to control, calibrate and design the gasoline engine in such a way to convert part of the reliability margin into efficiency, and furthermore it finally enables the estimation of that margin.

The second chapter deals with the on-board measurement of the in-cylinder conditions. An accurate and robust feedback is essential to control the desired operating conditions, but the pressure sensor can still be an unaffordable solution for some product ranges. Instead, ionization current signal can be a good compromise between cost and signal-to-noise ratio, since it provides information both about knock intensity (like accelerometer does, for example) and combustion phasing, allowing the estimation of most of the performance indexes which can be calculated with the pressure signal.

The third chapter, instead, investigates the efficiency increase that can be achieved through the delivery of water in the combustion chamber. Water injection is a well-known technology, but it has been relegated to specific applications (aeronautic, motorsport), where water consumption was probably the last of the problems and efficiency increase not the first objective. The benefits of a lower knock tendency and reduced exhaust temperature are evaluated, in relation to the involved water quantities, since water availability in passenger cars and customer acceptance are the main issues to successfully apply this technology.

The fourth and last chapter proposes a relatively simple empiric knock model, to be used to predict knock intensity. This kind of tool is the last piece of the jigsaw, which completes my research path and which grants the development of a smart and effective combustion control strategy, able to realize the desired combustion mode in every operating condition.

# 1 Knock Damage

## 1.1 Introduction

This chapter concerns what was the main research activity within my PhD course, which was focused on the knock damage modelling and on the understanding of its mechanisms. The objective of such model is to predict engine damage (piston damage in particular) as a function of the in-cylinder pressure history. The applications of this model can be diverse:

- Firstly, it can be used to (re)define the knock level thresholds adopted during the engine calibration process, which partly affects the design process too (i.e. compression ratio). Apparently, most of the car manufacturers are using similar criteria, sometimes also with the same “numbers”. In any case, the definition, the choice of the maximum knock level to be considered during the engine calibration, when it does not coincide with the definition of KLSA, it is mainly a creative process.
- A perfectly calibrated engine, with the mentioned thresholds, is powerless to detect fuel knock resistance and engine ageing. Hence, an additional safety margin is taken when transferring the calibration of the sample engine to the production ECU. If the engine control system implements a knock control strategy, this is almost certainly protective only. A damage model, if implemented in the spark advance control strategy, can target a predefined damage level, pursuing the maximum reliability-limited efficiency and considering the whole life of the engine and the relevant operating condition variables.
- Finally, depending on the physical content of the resulting model, it can be used in the design process of the piston geometry and boundary conditions.

Such model is natively control-oriented, hence it does not necessarily have to be deeply based on the involved physics. This is because an implementable real-time control strategy requires a relatively simple algorithm, with a consequent low computational effort. Moreover, some of the involved mechanisms, such as the interaction between the in-cylinder charge within a knocking combustion and the piston surface, cannot be directly measured, but only hypothesised through their observable effects. Therefore, certain aspects need to be simplified, at least in this stage. On the other hand it is clear that, the higher the physical content, the higher the predictivity and the transferability of the model.

## 1.2 Literature review

It is well known that pistons, also in their normal use, simultaneously undergo different and complex damage mechanisms such as fatigue, wear, oxidation, etc. Pistons need to withstand significant mechanical loads, due to combustion pressure, and additional thermal stresses, due to the local heat flux which causes surface temperature oscillations and non-uniform temperature distribution [1.1, 1.2]. Moreover, pistons themselves are part of the combustion chamber, which means their service temperature might exceeds 300 °C on the crown [1.3]. Since pistons are highly thermomechanical loaded components, many researches are focused on the thermomechanical fatigue damage of pistons [1.4-1.6], and on its modelling [1.7] while other studies deal with wear damage and scuffing of both piston skirt and piston rings [1.8-1.11]. Very few studies, instead, are available about the specific damage mechanisms induced by knocking combustion and the relationship between different knocking levels and corresponding piston damage.

It is reported in literature that severe knock can significantly damage the combustion chamber components, such as cylinder heads, cylinder liners, and above all pistons [1.12-1.16]. The causes of this damage are probably the increased heat flux and the high and localised thermomechanical stresses occurring during the process [1.13, 1.17].

The limited literature data available on knocking combustion damage show that the possible damages on pistons include erosion at piston top land and crown, lands fracture, blow-by channel with subsequent power loss, piston seizure and jammed or broken rings in the most severe cases [1.13]. In the author experience, however, most of the catastrophic failure that are traditionally attributed to knock (such as piston seizure, formation of blow-by channels, ring gap closure, lands fracture...) are not merely caused by knock itself, but are rather the result of repeated, persistent knocking combustions, which grow in intensity, finally turning into mega-knock or preignition [1.18, 1.19].

Nates, in [1.20], describes a fatigue cycle due to alternation in the shock waves and thermal expansion effects, where both contributions are assumed to have the same order of magnitude. Finally, the fatigue mechanism is the responsible for the observed erosion.

Some authors [1.17] highlight that the observed erosive surface destruction, very much resembles the damage caused by cavitation on the blades of water pumps and turbines. The cause of erosion seems mainly related to the direct shock pressure waves, while minor attention is focused on the effect of thermal stresses. However, the destruction of the thermal boundary layer [1.17] leads to a sharp increase in the convective heat transfer coefficient, thus causing high heat flux to the walls. This influences the temperature profiles and, therefore, the size and tribology of the components; moreover, it can lead to a significant loss in material strength (mainly in the case of aluminium pistons) favouring a consequent mechanical damage.

Since the term “knock” is still deeply related to unfavourable consequences, the current guideline in engine calibration is that knock must be totally and carefully avoided [1.21], even if the strategies to prevent knock (namely to decrease the compression ratio, to retard the spark timing, to use cooled Exhaust Gas Recirculation [1.21]) strongly penalise engine efficiency. However, as already reported by Nates et al. in the '90s [1.12, 1.13, 1.15], it is worth pointing out that only when exceeding a certain threshold knock compromises engine functionality. Light knock is not harmful and might be even beneficial in terms of both engine efficiency and low emissions: if light knock is accepted, in fact, the engine operating point can be shifted towards the maximum efficiency conditions.

The rising questions are therefore: “Which is the knocking threshold not to be exceeded to avoid damage?” And above all: “Are there engine parameters/indexes which can be related to knock damage?” [1.12, 1.13, 1.15, 1.22, 1.23].

The mechanisms of damage induced by knock on the combustion chamber components are not currently fully understood. Moreover, the development of a knock index directly related to the damage induced on engine components, and the corresponding methodology to identify proper diagnostic threshold values, is still an open and crucial challenge

In order to provide thorough answers, a careful experimental campaign is necessary, focusing both on the variation of single knocking parameters during bench tests and on the analysis of corresponding pistons damage. Extreme knocking conditions in the experimental campaign are not of scientific interest, since the aim is not to study the deleterious effects of knock, but to slightly increase knocking intensity from the “safe calibration area”, to determine the acceptable damage on pistons.

### 1.3 Experimental Setup

Long stationary tests have been conducted on a V8 GDI turbocharged engine, in controlled knocking conditions. For a predetermined test duration, all the operative parameters, including knock intensity, are kept constant (as far as possible), to be associated to the measured induced effects on pistons. Indeed, all the operated pistons have been examined after the operation, to identify all the relevant information related to knock damage.

### 1.3.1 Test Bench

Every cylinder is equipped with side-mounted in-cylinder pressure sensors, and as standard equipment the engine is equipped by ionization current sensing system. Both the pressure and the ionization current signals have been logged at high frequency (200 kHz) throughout the whole experimental activity. Pressure is, of course, the starting point for this activity, since is to be considered one of the most accurate information that can be extracted by the combustion chamber. But, in a second stage, all the combustion parameters needed for control purposes (i.e. needed by the damage model) are to be replaced by the equivalent ones obtained by the ionization signal, if possible.

The engine operated one bank at a time, due to test bench limits; so every test involves just 4 cylinders, 4 pressure (and ion) signals and 4 (eventually damaged) pistons.

Figure 1.1 describes the loop used to control knock intensity: the combustion analyser communicates via CAN the cycle-by-cycle knock indexes (MAPO, Maximum Amplitude of Pressure Oscillation) to a RCP (Rapid Control Prototyping device), which communicates to the ECU the spark advance corrections, exploiting the existing communication between the ECU and the ionization current analysis module (not used in this loop).

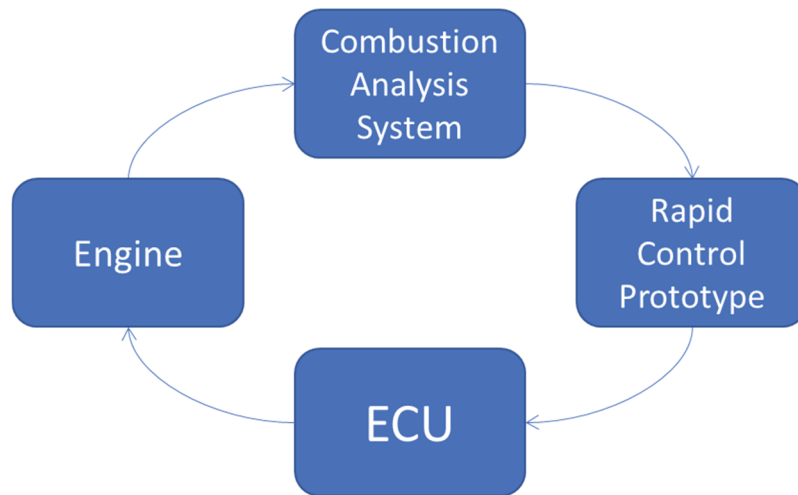


Figure 1.1 – Engine control loop used during the experiments to control knock intensity through the spark advance.

The communication is fast enough for the ECU to actuate the calculated correction, based on the last combustion, to the incoming cycle and every cylinder is controlled independently.

### 1.3.2 Piston Analysis

All the activity related to the damage measurement and material properties identification has been carried out by the colleague Eleonora Balducci, which research activity is focused on metallurgy and failure analysis. Hence, a quick overview is here presented, while more details can be found in the published literature [1.23, 1.24].

#### 1.3.2.1 Hardness Measurements

A typical analysis for heat treated pistons, is the hardness measurement. Indeed, heat treated aluminium alloys undergo a significant decay of mechanical properties (and so hardness) due to coarsening of precipitates, when exposed at temperatures above 200°C [1.25-1.27]. In particular, the tested pistons are made of a near eutectic Al-Si-Cu-Ni-Mg alloy and heat-treated to the T7 condition.

By characterising the hardness decay behaviour, which has been done in a first stage of the activity, it is possible to estimate the mean operation temperature of the area involved by the measurement.

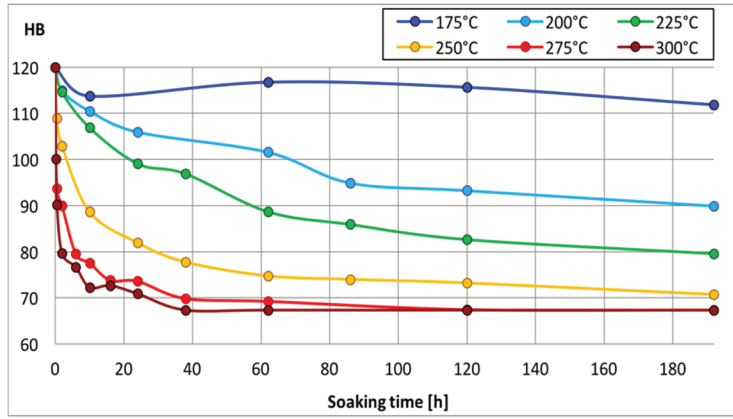


Figure 1.2 – HTT (hardness-temperature-time) curves for the aluminium alloy.

In Figure 1.2, the material decay is reported as a function of time and temperature [1.24]. The data reported in Figure 1.2 has been fitted, in order to obtain a monotonic function (the positive slope that can be observed here and there are to be attributed to measurement uncertainty and non-perfect material repeatability). The left plot in Figure 1.3 represents the fitted data, while the right plot describes the decay speed, expressed in Brinell lost per hour, as a function of the current hardness and temperature.

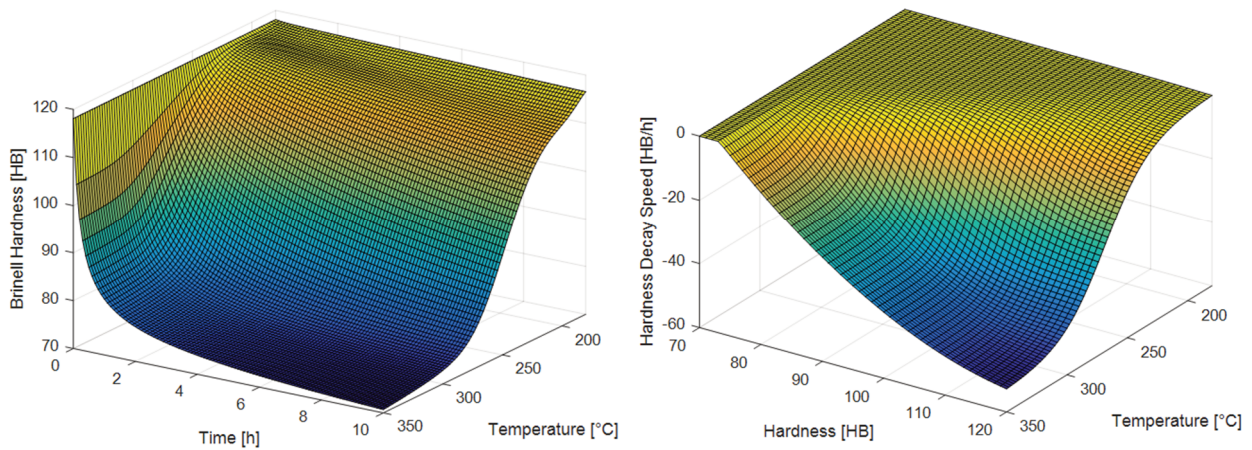


Figure 1.3 – Fitted HTT (Hardness-Temperature-Time) behaviour (left) and the corresponding differential form (right), describing the hardness decay speed depending on hardness and temperature.

The hardness as a function of time and temperature is actually an integral representation of the decay phenomenon, analytically described by Equation (1.1), while instantaneous temperature and hardness are supposed to be the independent variables governing the decay.

$$HB = HB_{start|t_0} + \int_{t_0}^{t_1} \frac{dHB(HB, T)}{dt} dt \quad (1.1)$$

The integral approach (Figure 1.2 and left plot in Figure 1.3) is still very useful to estimate the mean equivalent temperature depending on the residual measured hardness and the operation time, while the decay speed  $\frac{dHB(HB, T)}{dt}$  which has been calculated from the previous fitting, can be used to estimate the hardness decay for a generic temperature history and for a generic initial hardness. Even if the test bench tests are conducted in stationary conditions and the piston temperature can be assumed almost constant during the operation, the “differential” approach should be more accurate (an oscillating temperature profile generates a higher decay w.r.t. to the correspondent mean temperature) and more



generic, theoretically allowing the hardness estimation for every temperature history (engine speed, load, etc.).

The material characterization and the proposed modelling involve Brinell hardness measurement (with 2.5 mm diameter indenter and 62.5 kgf load, according to ASTM E 10-08 standard). The initial hardness of every piston has been evaluated before the engine assembling through 4 Brinell hardness measurements as well, in the bottom part not to alter the crown surface, as shown in the left picture in Figure 1.4. Since the microstructure of this forged pistons is very homogeneous, the mechanical properties, and so the hardness, is supposed to be uniform throughout the piston.

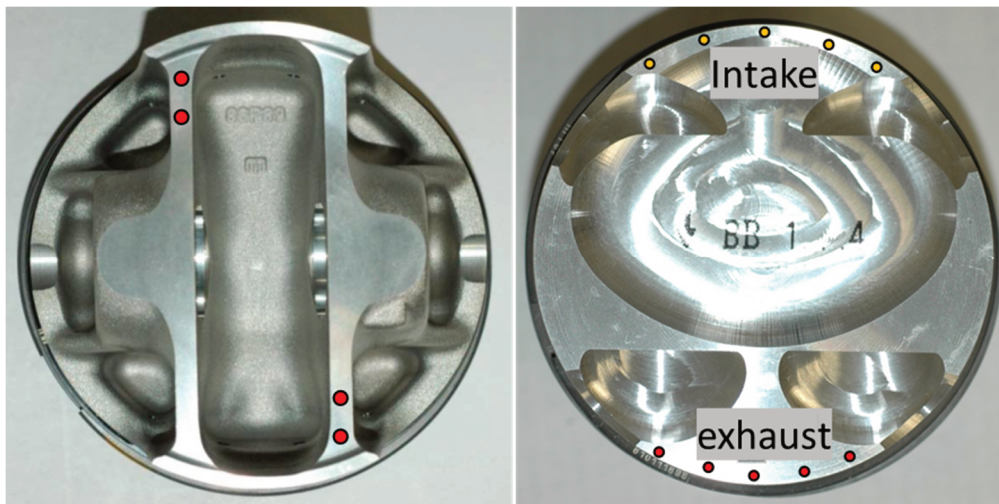


Figure 1.4 – initial Brinell hardness measurements (left) and post-operation Vickers hardness measurements (right).

Instead, micro-Vickers hardness measurements (with 1 kgf load and 10 s dwell time) have been performed to quantify the post-operation hardness decay, due to the higher flexibility w.r.t. Brinell hardness. Indeed, since the micro-Vickers imprint is smaller, it allows to investigate areas very close to edges or to other imprints. Micro-Vickers measurement locations are shown on the right side of Figure 1.4 (5 imprints for each side, intake and exhaust). Then, a conversion between the two scales is needed, which is possible due to the high correlation existing between them, as shown in Figure 1.5.

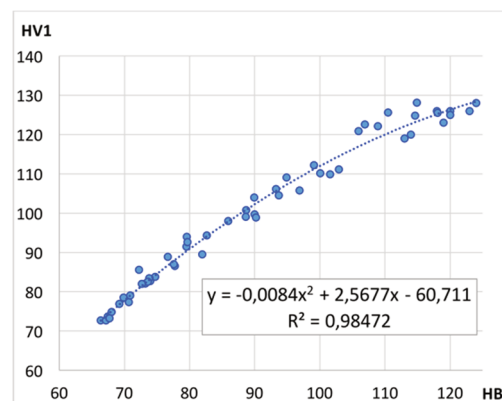


Figure 1.5 –Regression function between Vickers and Brinell hardness values, used for conversion from one scale to the other.

### 1.3.2.2 Damage Estimation

The damage evaluation covers many aspects and several measurements have been carried out to numerically quantify the damage induced by knock on every tested piston.

Many effects are attributable to knocking combustions, as described in literature, but limited to the specific case and to synthesize, the main observed effects are:

- Overheating of the interested areas: per se this is not directly considered as a damage, but the consequences are measurable on the residual hardness;

- Erosion: it is the main damage mechanism, measurable through roughness measurement and visual analysis. In this sense, the roughness index which results having the highest sensitivity is RzD, according to DIN 4768. In particular, since the roughness of the new piston is relatively low, eroded areas are characterized by an increasing roughness index with the knock intensity. Some attempts have been made to measure the extension of the eroded area. The erosion mechanism involves both the anodized surfaces in correspondence of the 1<sup>st</sup> ring groove and the naked aluminium alloy;
- Reduction of the 1<sup>st</sup> ring groove gap: due to combined effect of higher piston temperature and the mechanical action of the pressure waves induced by knock, the thinnest and cantilevered portion of the top-land area interested by knock, tends to bend in the direction of reducing the ring gap. This measurement has been made through gauge blocks before and after the operation, for some of the pistons.
- Polishing in the valve pocket edges. This effect could be explained as a consequence of local overheating, consequent thermal expansion and then contact with the liner. Another possible concurrent explanation can be the local deformation due to the shock waves impact: the same action responsible for the erosion and for the top land bending (which causes the ring gap reduction) can possibly compress the material, resulting in a positive radial deformation and again inducing the contact with the liner. Both possibilities will be investigated in the future through circumferential profilometry.

Some limitations apply to these measurements: typical roughness evaluation is defined within a straight line and the chosen one cannot necessarily be representative of the average roughness of the eroded area. Moreover, depending on the measuring instrument, the measurement can be performed in very specific zones only. Consequently, it can be hard to perform several measurements and the few performable may not involve the most “interesting” area. Then, since erosion is not observed in the same exact location every time, the line selected for the measurement is partly arbitrary.

The border between eroded and integer surface is not clear-cut, so the extension evaluation of the eroded area has a level of arbitrariness as well.

Some attempts have been made in estimating the eroded area by means of digital image processing, confirming that the process cannot be completely automatized and the user contribution (and dependence) is not negligible. Figure 1.6 reports an example of image filtering used to estimate eroded area, starting from the top left to the bottom right.

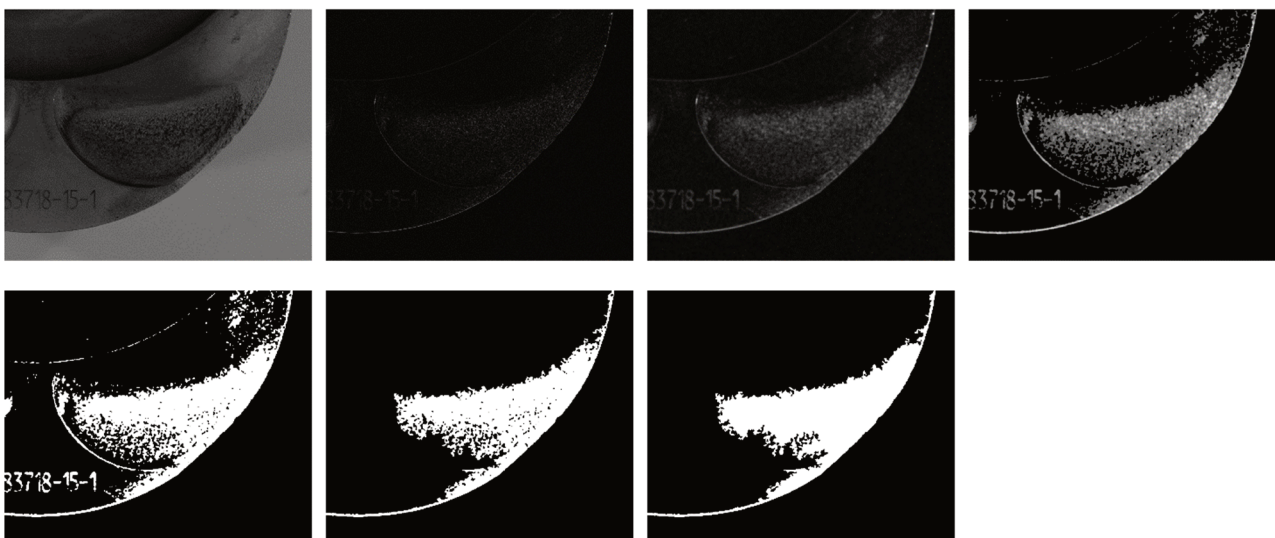


Figure 1.6 – Example of consecutive digital image filtering, used to estimate the eroded area. In the top-left picture, the original picture, in the bottom-right the final binarized image highlighting the eroded surface.

The first and current approach regarding the damage analysis is to define a single synthetic index able to synthesize the total induced damage, considering all the mentioned effects (erosion severity and functional undermining), to be used to calibrate the damage model.

Currently, a systematic estimation of the damage is under definition and a subjective evaluation, which considers all the mentioned effects, is used. The scale goes from 0 (no damage) to 10 (maximum damage observed in the considered pistons). The use of a subjective quantity is currently the main limit of this approach, but in its defence, it can be stated that:

- the resulting ranking is relatively shareable and clear: in most of the cases the kind of damage is the same and easily comparable, so that a failure analysis engineer or a skilled engine technician would agree with this assignment
- the measured damage index is well correlated with roughness measurements, extension of the eroded area and reduction of the 1<sup>st</sup> ring gap.
- a systematic definition of the index would inevitably rely on measurements affected by some degree of arbitrariness.

## 1.4 Experimental Data

### 1.4.1 Engine boundary and control parameters

To calibrate the models proposed in the next sections, 6 sets have been considered. One “set” includes 4 pistons (1 bank of the V8 engine), operated in stationary conditions, in terms of engine speed, load, lambda, knock intensity target, fuel RON, for a predetermined duration (with one exception), and the whole pressure history of every cylinder.

Every set would require a detailed explanation of the choices about the test conditions, here an overview is provided.

In the majority of the cases, knock intensity has been controlled by a control strategy very similar to a PI controller, targeting a predefined percentile (98<sup>th</sup> or 99.5<sup>th</sup>) level of the considered knock index, MAPO, defined by:

$$MAPO = \max(|P_{BP\ filter}|) \tag{1.2}$$

Where  $P_{BP\ filter}$  is the band-pass filtered pressure signal, within an appropriate angular window.

In Table 1.1, some average operation parameters are reported, in terms of engine speed and load, adopted fuel, total duration of the test, maximum pressure and knock levels (normalized for confidentiality reasons) and the adopted control strategy.

The desired behaviour of the controller is not to be too aggressive on the spark advance correction. Since in knocking conditions high MAPO percentiles, like the ones considered, are characterized by high variability, is not worth to try (and it is impossible) to control a “constant” value. On the author opinion, in stationary conditions, the best way to control a “constant” knock level is by a “constant” spark advance, so in practice little variations of the spark advance are required to achieve on average the desired knock level. Then there is the question if a high percentile of the considered knock index is the right parameter to be considered and controlled. MAPO (high) percentile is a wide spread metric for knock intensity evaluation, it is convenient to make comparisons and it results having a high sensibility to high values (in the sense that they are far from the mean value). The high sensibility is the same responsible for the high variability, which can be compensated with a wide statistical basis, which is the case. With the definition of a damage model, you can think of overcome, at least partially, such limits.

Another control strategy has been tested, denoted “Frequency” in Table 1.1, to demonstrate and quantify the role of the local density of knocking combustions. The note “1/50 > 11.9” describes a strategy which is controlling about 49 cycles in non-knocking conditions by applying a corresponding low SA (Spark Advance)

and waits for one cycle with MAPO > 11.9 % while applying a higher SA. On the other hand, 6/300, means that the controller waits for 6 cycles with MAPO over 11.9 % (with high SA), and rests 294 cycles with no-knock SA. The expected outcome (which was basically missed) was to have more damage on this last condition, due to the higher local density of knocking events and the corresponding skin overheating, even if the average ratio of cycles with MAPO > 11.9 % is the same in both cases.

Cylinder 5 in set 6 sx was controlled in the same way, but without the counter feedback, because the head-mounted pressure sensor was not available. The sensor on the spark plug was considered for the post-processing, but not for the control since the measured intensity is affected by the measurement location. A posteriori, some pressure analysis is possible and useful information about the damage mechanisms, even if not directly correlated to the pressure history, is available.

Set 6 sx experienced different knock levels, between the first 5 and the following 10 hours. This is because the developing intermediate damage models suggested to cover other knock intensity ranges.

Table 1.1 – Operating conditions for all the tested pistons.

SET	Speed/ Load	Fuel	Duration	Cyls	MAPO 99.5 [%]	PMAX [%]	Control	Target
SET 3 DX	4500 x 2200	RON = 95	14.8 h	cyl 1	25.1	52.8	PID Mapo98 =	11.9
				cyl 2	11.1	42.9	PID Mapo98 =	5.8
				cyl 3	26.3	50.9	PID Mapo98 =	11.9
				cyl 4	3.7	37.5	-	-
SET 4 SX	4500 x 2200	RON > 95	3.3 h	cyl 5	43.2	59.0	PID Mapo98 =	24.3
				cyl 6	38.7	64.4	PID Mapo98 =	24.3
				cyl 7	22.2	58.4	PID Mapo98 =	11.9
				cyl 8	11.9	50.4	PID Mapo98 =	5.8
SET 6 DX	4500 x 2200	RON 95	11 h	cyl 1	46.5	41.0	PID Mapo98 =	11.9
				cyl 2	100.0	2.2	Frequency	1/50, 36.6
				cyl 3	55.1	0.6	Frequency	1/50, 11.9
				cyl 4	58.0	0.0	Frequency	6/300, 11.9
SET 6 SX	4500 X 2200	RON = 95	5 h	cyl 5 *	49.0	27.8	Frequency	1/50
				cyl 6	27.2	48.7	PID Mapo98 =	11.9
				cyl 7	28.0	48.3	PID Mapo99.5=	36.6
				cyl 8	16.9	41.4	PID Mapo99.5=	15.0
			10 h	cyl 5 *	30.9	26.7	Frequency	1/50
				cyl 6	27.2	51.5	PID Mapo98 =	11.9
				cyl 7	32.5	53.2	PID Mapo99.5=	36.6
				cyl 8	43.6	55.4	PID Mapo99.5=	44.9
SET 7 SX	6000 X 2300	RON = 95	10 h	cyl 5	3.7	45.9	-	-
				cyl 6	23.0	59.9	PID Mapo99.5=	20.2
				cyl 7	28.0	60.8	PID Mapo99.5=	32.5
				cyl 8	43.2	66.4	PID Mapo99.5=	44.9
SET 8 SX	6000 X 2300	RON = 91	7.8 h	cyl 5	0.4	7.1	-	-
				cyl 6	34.6	23.1	PID Mapo99.5=	36.6
				cyl 7	48.6	26.3	PID Mapo99.5=	53.1
				cyl 8	69.1	26.9	PID Mapo99.5=	69.5
SET 9 SX	6000 X 2300	RON = 100	6.1 h	cyl 5	0.0	48.1	-	-
				cyl 6	16.0	87.3	PID Mapo99.5=	16.0
				cyl 7	28.4	95.9	PID Mapo99.5=	28.4
				cyl 8	40.3	100.0	PID Mapo99.5=	40.7

The use of different RON fuels, as will be described in the next section “1. 5 Physical overview and



experiment design”, is used to unlink the thermal load and the knock intensity. All this data, whatever the choices for the operating conditions, cover a wide domain in terms of pistons conditions and consist on a good database to calibrate the proposed models.

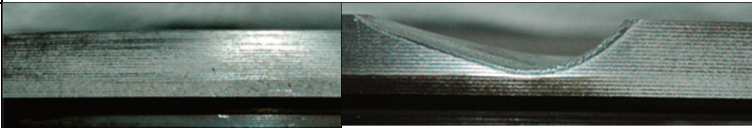
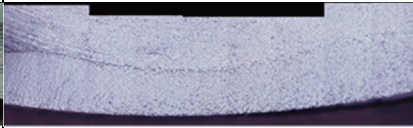
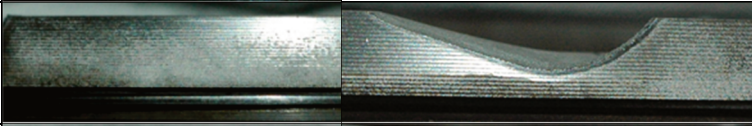

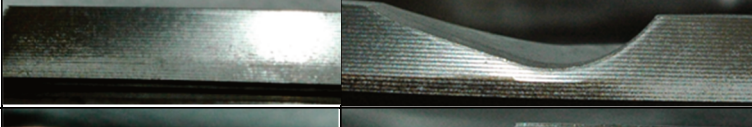
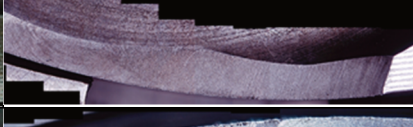


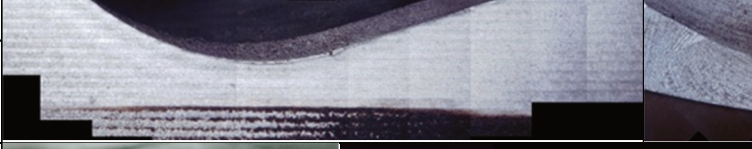
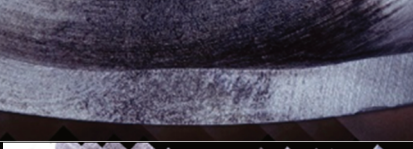
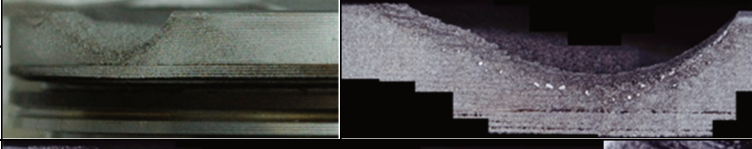
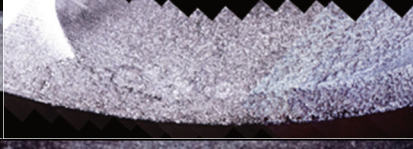
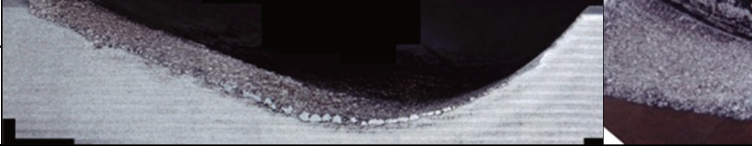

#### 1.4.2 Measured induced damage on pistons

All the mentioned operating conditions, different for every cylinder, induced a wide spectrum of effects on the operated pistons, from non-damaged to heavily damaged. To be noted that all the pistons were still perfectly functional and there was no decay in all the measurable test bench parameters (blow-by flow, indicated torque, etc.), so that the observed damage is purely attributable to knocking combustions (eventually to some undesired pre-ignition cycles), while there is no trace of secondary effects such as piston seizure or scuffing or ring seizure.


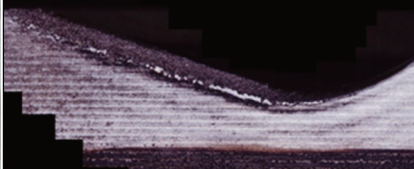

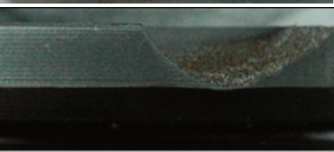
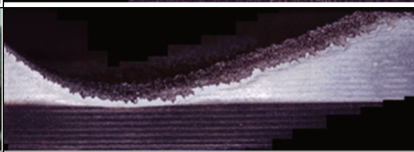

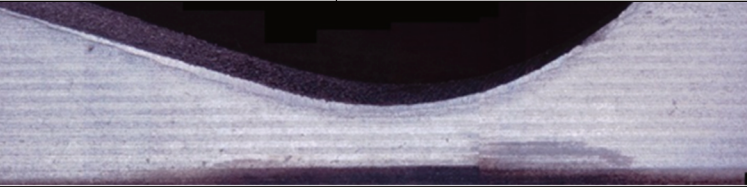
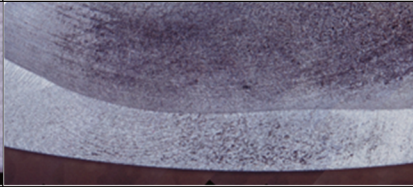


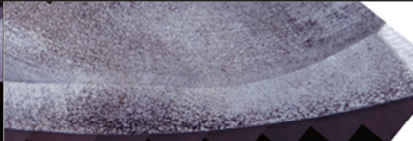


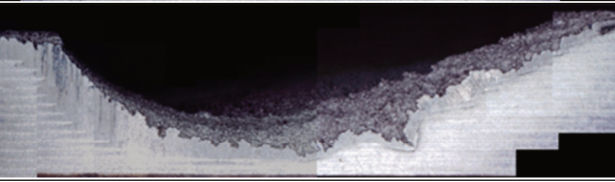
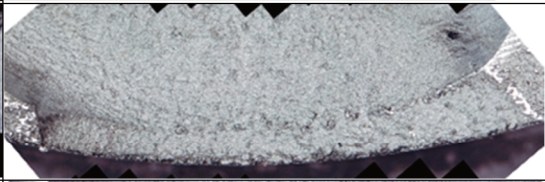
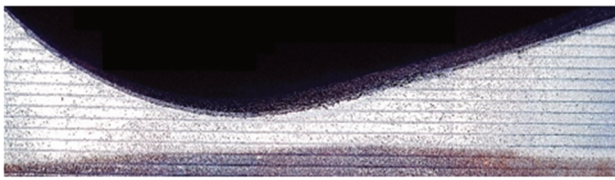
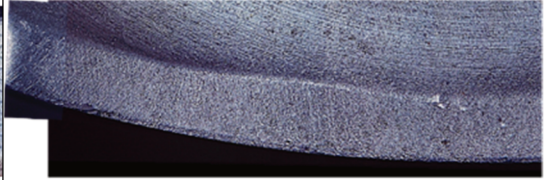
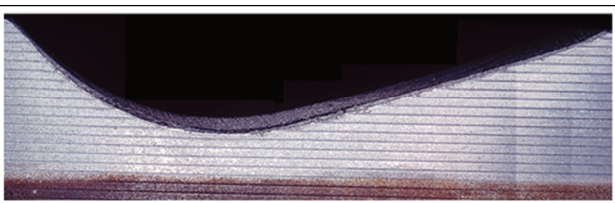
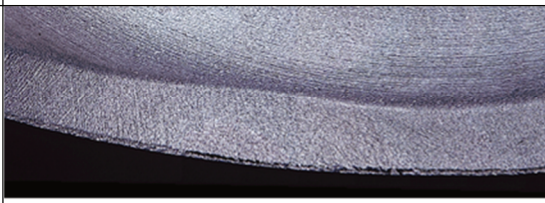
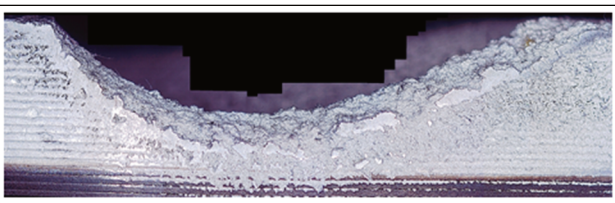
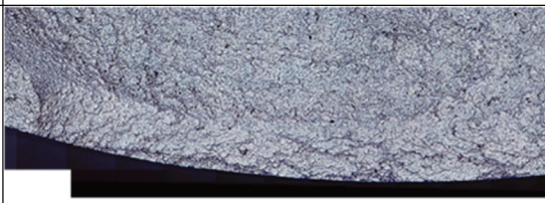
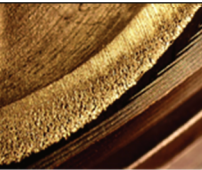
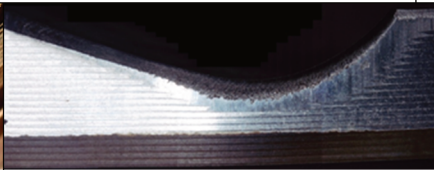
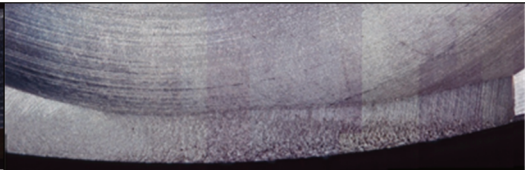
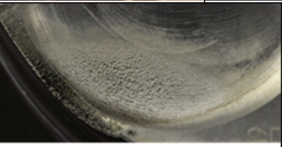


As described in “1.3.2 Piston Analysis”, several measurements have been conducted to quantify the induced damage, and the resulting damage index is partly subjective.

In Table 1.2, some pictures depicting the induced effects and the corresponding damage index are reported, for every damaged piston (non-damaged pistons are not reported).

Table 1.2 – Overview of the observed damage on the tested pistons.

Set, piston	Side view	Top view	Damage index
Set4 P5			3
Set4 P6			3
Set4			1
Set4 P8			0.5
Set 6 p1			0.8
Set 6 p2			8
Set 6 p3			3



Set 6 p4				3
Set 6 p5				3
Set 6 p7				0.8
Set 6 p8				2.5
Set 7 p7				1.5
Set 7 p8				6
Set 8 p6				1.2
Set 8 p7				2
Set 8 P8				10
Set 9 p7				3
Set 9 p8				5

## 1.5 Physical overview and experiment design

In this chapter, some hypothesis derived by the literature and the consequent considerations are agreed, in order to define a work flow and the methods requested by the problem.

### 1.5.1 Knock effects

According to and resuming the mentioned literature, knocking combustion is supposed to produce two concurrent effects on the piston surface:

- Thermo-mechanical stress, induced by shock waves and the corresponding high temperature gradient due to the boundary layer disruption. This mechanism is practically impossible to be measured and quantified: it would need to measure the mechanical stress or the deformation and eventually the instantaneous thermal flux directly in the material skin. Indeed, the pressure waves measured by the in-cylinder pressure sensor are extremely far from the yield stress of the piston material. The distance between the volume interested by the most severe reflection, eventually amplified by the geometric confinement, and the pressure sensor location, leaving aside the thermal contribution, assure that they (the measured and the actual stress) are totally different quantities. Basically, the transfer function between the “real” knock intensity and the pressure measurement is missing.  
Anyway, it can be stated that the two quantities are relatively well correlated, as can be correlated pressure signals acquired from distinct locations in the combustion chamber. Therefore, a typical pressure-based knock index should be a good indicator of what is actually stressing the piston surface. Moreover, since the boundary layer is perturbed by the same phenomenon, such index should be able to take into account for the thermal contribution (as a component of the thermo-mechanical stress) too.
- Overheating of the affected areas: for the afore-mentioned mechanism, a close succession of intense knocking combustion induces a global temperature increase, understood as a massive effect of the interested area of the piston (not necessarily the entire piston), while the single event is supposed to have an extremely local (skin) effect, due to the high mass and thermal conductivity of the piston. The knock intensity, estimated as far as possible, by the pressure signal, can be considered as an enhancer of the heat transfer. Consequently, the heat transfer rate (the heat transferred to the piston during a cycle) should depend both on the knock intensity and on the spatially-averaged in-cylinder conditions.  
In a previous work, [1.18], the correlation between the heat transfer increase and the knock level was demonstrated and partly quantified.

### 1.5.2 Piston temperature

Piston temperature must have a role in knock damage, since it determines the mechanical properties, the susceptibility of the piston material to be damaged by the stress induced by knock events. Basically, all the aluminium alloys have sensibly lower mechanical properties at high temperatures. Moreover, heat-treated alloys suffer permanent mechanical decay (over-ageing), depending on the duration of the exposure to high temperature.

Therefore, piston material properties depend on the instantaneous temperature and on the whole temperature history.

Being temperature so influent, it is of major importance to estimate piston temperature. The material decay itself, after being characterised, can be used to calibrate and validate a piston temperature model.

### 1.5.3 Spark advance, heat transfer and knock intensity

At this point, the focus moves back to the heat transfer process, since it is crucial for a physical piston temperature model. As hypothesised, heat transfer can be considered as the result of two contributions:



one is the “standard” amount transferred within a non-knocking combustion, while a further amount is given by the knocking operation. For a given charge motion, engine speed and load, A/F ratio (i.e. for a given operating condition of the engine), the heat transfer, in non-knocking conditions, is governed only by the temperature profile within the cycle, that can be increased by increasing the spark advance. Also a predefined knock intensity (seen as a statistical value) can be easily controlled with a quasi-static spark advance.

Now, the knock-free heat transfer rate and the knock-related contribution are supposed to be unknown and need to be calibrated, depending on the in-cylinder conditions and on the knock intensity, respectively. But, since both terms are depending only on the spark advance, for a given operating condition, it is very hard to characterize both. Substantially, supposing to conduct stationary tests where the resulting hardness on piston is converted in an equivalent mean local temperature and then potentially in the corresponding mean specific heat flux, it is not possible to decouple the two contributions, since they are rigidly depending on the same control variable (i.e. the spark advance).

Therefore, a further degree of freedom (or a control variable) is needed to alter the bond between in-cylinder conditions, determining the knock-free heat transfer rate, and knock intensity (i.e. knock occurrence), determining the contribution to heat transfer due to knock. Substantially knock sensitivity to spark advance needs to be modified or controlled, for the generic operating condition. There are potentially several ways to do this: for example, it is possible to adjust the air-to-fuel ratio, the intake temperature or the residuals concentration by modifying the valves timing. These solutions should give the possibility to vary continuously the knock sensitivity, but probably in a small range and with collateral effects on the charge temperature profile and trapped quantity. On these considerations, such solutions have not been investigated. The choice fell on varying the fuel octane number, which is a non-flexible solution (it cannot be varied with continuity during the tests, or it would require a relatively complex experimental setup), but it should have minor effects on charge temperature and trapped quantity, depending on the stoichiometric air-to-fuel ratio and LHV. In this way, it is possible to produce the same heat transfer rate with different knocking level, and vice versa.

This approach is needed also to quantify and calibrate the temperature role in the damage mechanism by controlling, for example, different piston temperatures but the same knock intensity. If, for example, pistons subjected to the same knock intensity show different induced damage levels, the piston temperature role in the damage mechanism is confirmed and it can be understood and modelled.

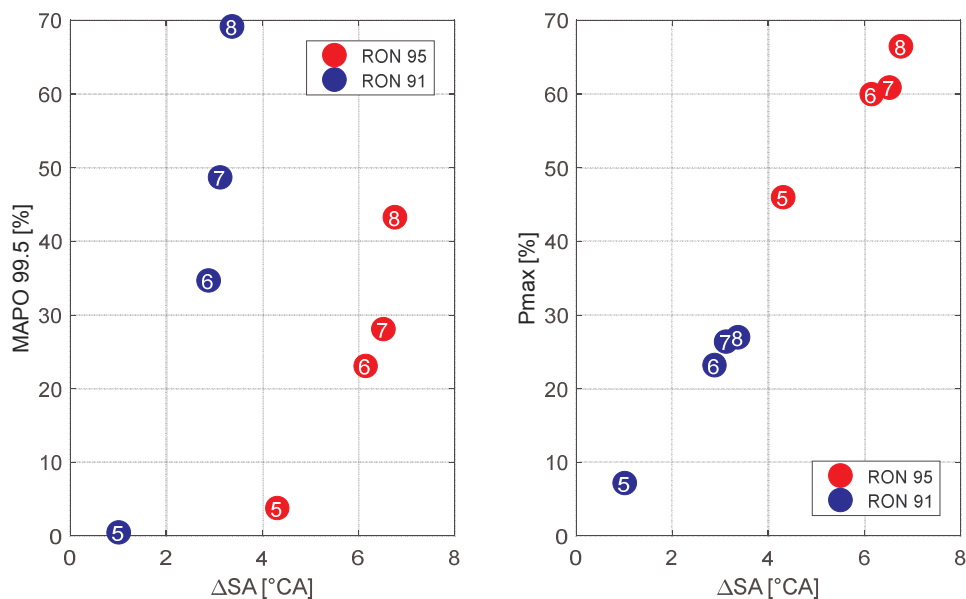


Figure 1.7 – Normalised knock level (average MAPO 99.5%) and maximum pressure level (average Pmax) depending on the average applied  $\Delta SA$ , for set 7 and 8, which operated with RON 95 and 91, respectively.



The desired effect is described in Figure 1.7, which has been discussed in [1.30]. The figure reports the average values of maximum pressure and knock intensity (estimated in terms of MAPO 99.5<sup>th</sup> percentile) as a function of the actuated spark advance difference throughout the test. On the right side of the figure, the linear dependence of the maximum pressure with the spark advance can be observed. As expected, the maximum pressure level dependence on the spark advance is basically not affected by the adoption of different fuels.

The maximum pressure, in this stage of the work, has been considered as an indicator of the thermal load. It has been preferred to the maximum temperature (or to an equivalent temperature, representative for the single combustion cycle) just for convenience, not to consider charge mass, composition and their uncertainties. However, a similar correlation between heat transfer rate and a temperature value rather than maximum pressure would have been needed (a conventional angle-resolved heat transfer model will be considered in a later stage). In [1.18], the close correlation between heat transfer and maximum pressure has been demonstrated.

On the left plot, instead, the correspondent knock intensity is reported, as a function of the spark advance. In this case, contrary to the maximum pressure, the resulting knock level response curve depending on the spark advance is shifted towards higher spark advance values for higher RON fuel.

In Figure 1.8, the resulting damage evaluation, where the higher value corresponds to the most damaged piston (as mentioned before, the damage scale is partly subjective but the ranking is hardly questionable), is described as a function of the estimated mean piston temperature (estimated by residual hardness measurements) and the average knock level. By comparing the pistons denoted by damage levels 2 and 6, it is clear how crucial can be the piston temperature in determining the piston resistance to knock action: the higher the piston temperature, the higher the induced damage for the same knock intensity. Similarly, even if the damage level difference is less pronounced, pistons denoted by damage levels 1.2 and 1.5 can be examined. It is then clear how this result can be considered when defining the cooling condition and the piston design, since a cooler piston results being more resistant to knock damage; the outlined qualitative linear iso-damage lines corresponding to levels 1.5, 3 and 6 can help in quantifying the temperature effect.

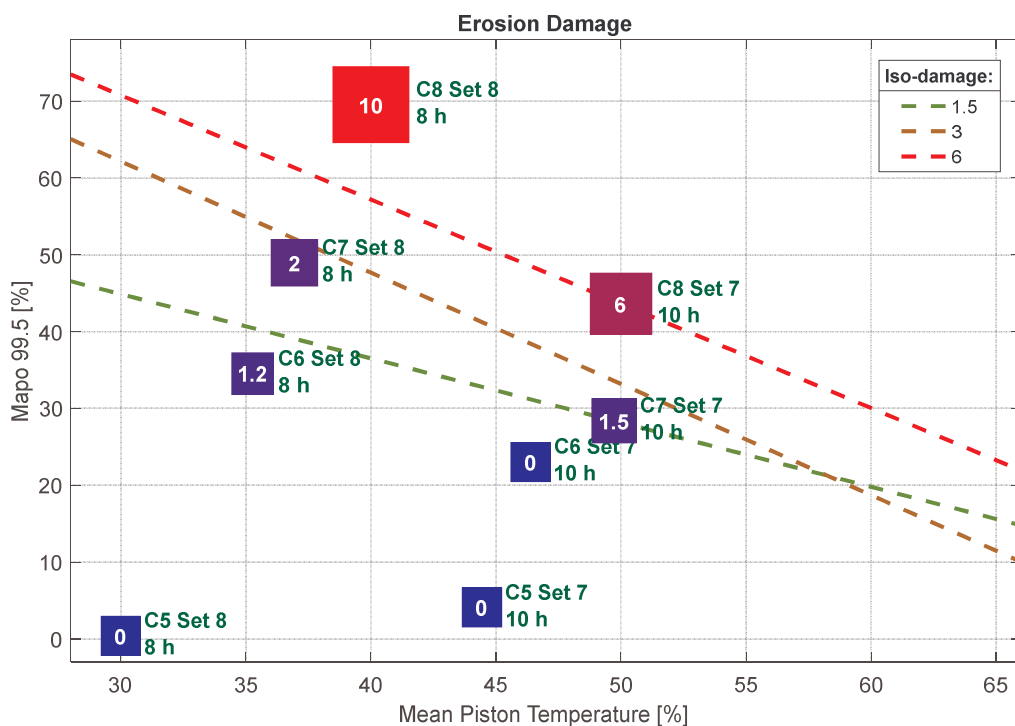


Figure 1.8 – Damage level (reported inside the squared markers) depending on the knock intensity (MAPO 99.5 %) and the mean piston temperature (estimated through hardness measurements).

At the same time, the estimated piston temperature (from hardness measurements), realized with different maximum pressure (representative of the thermal load in knock-free condition) and knock levels, decoupled by the use of different RON fuels, is theoretically sufficient to calibrate a piston temperature model and heat transfer rate through the piston as a function of maximum pressure and knock intensity.

With this approach, i.e. by using different fuels, by conducting stationary tests, by measuring residual hardness and induced knock damage, it is on paper possible to calibrate both the piston temperature and the damage models, with statistically relevant data.

### 1.6 1-D piston temperature model

In the previous section the piston temperature (i.e. superficial piston temperature on the combustion chamber side) has been considered as a mean quantity within the piston. As described in Figure 1.4, 10 post-operation hardness measurements are available for every piston, 5 for each side. In Figure 1.9, the measured (normalized) hardness values are reported for 3 pistons, showing non-uniformity of the temperature field, both on the intake and on the exhaust side. Location #3 corresponds, for both sides, to the measurement made on the thrust-antithrust axis.

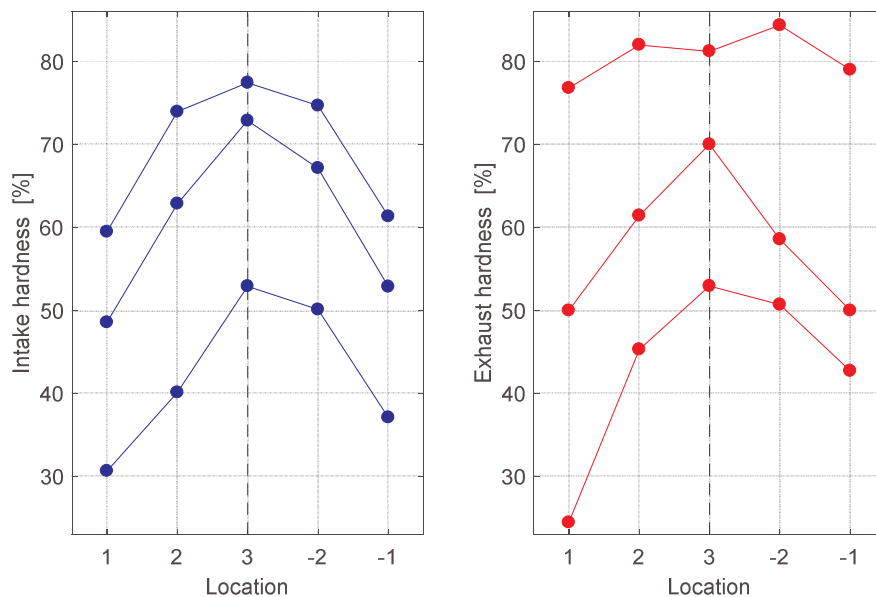


Figure 1.9 – Measured hardness field within the intake and the exhaust side for 3 pistons.

Since the temperature range is relatively wide, it can be of interest not to lose this information by averaging the hardness measurement. This can have multiple advantages:

- The damage appears to be localized, hence the damage model should be more accurate if the temperature of the damaged area could be considered;
- Residual hardness has a lower asymptotical value, which corresponds to the total loss of the precipitation strengthening. Because of the non-linearity of the ageing process with the temperature, not the hardness measurement but the estimated temperatures (corresponding to real different temperatures because of different locations) should be averaged. But because of the asymptote, the temperature estimation uncertainty increases as the hardness reduces. In extreme, to very high temperature areas correspond very similar hardness values, even if the temperatures are different. In this sense, considering a mean temperature value for a wide piston area (moreover for the whole piston) is not very appropriate;

- The same hardness measurement uncertainty can depend on the location within the piston, since the forging process can potentially generate a slightly non-uniform resistance in the piston material. Moreover, where the piston surface is characterized by a high temperature gradient, the measurement uncertainty is higher because of the uncertainty regarding the position of the hardness measurement ( $\pm 1$  mm w.r.t. the targeted location), while the measurement will be considered as taken in the nominal designated position.

These considerations have led to consider hardness measurements individually, or better location-dependent.

Within every side, the 5 measurements are symmetrical with respect to the thrust-antithrust axis (one is on the axis itself), as can be observed in Figure 1.10.

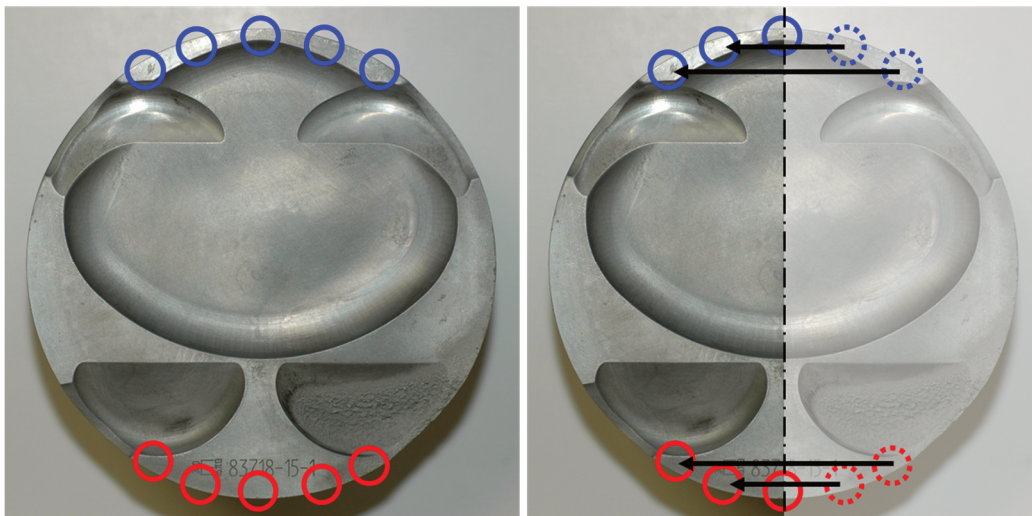


Figure 1.10 – Hardness measurements symmetry, used to average correspondent values.

The symmetry can be used to average the measurements. This way, as described on the right side of Figure 1.10, for every piston it is possible to consider 6 resulting hardness values, of which 4 are averaged, while the remaining 2 are on the thrust-antithrust axis. The spatial interpretation of the hardness measurements is propaedeutic to the following paragraph, which describes the temperature model.

The temperature model development is based on the following hypothesis:

- The heat transfer rate on the combustion chamber side (and probably on the oil side as well) changes order of magnitude within the cycle, but the skin piston temperature is supposed to have minor variations within the cycle, due to high conductivity and specific heat of the material. Because of this and especially considering the aim of such model (control), the considered time-step is the cycle duration.
- The exchange conditions between the gas and the piston crown are uniform throughout all the surface. More specifically, in this stage, the specific heat flux is imposed (Neumann boundary condition) and it depends on the in-cylinder conditions (maximum pressure and knock intensity). This means that the heat transfer is not depending on the surface temperature, which is not rigorous, but it should not have an important impact since the piston temperature is within a relatively small range compared to the gas space-averaged temperature. In a later stage, the exchange coefficient will be considered.
- The oil jet cooling is the only mechanism considered (it represents the 50-60 % according to [1.3]), so that the heat exchange through the ring belt and the skirt is neglected. These contributions are not negligible, but their calibration would require, for example, to conduct

tests with different coolant temperature (and to make the corresponding hardness measurements). This possibility will be further investigated.

- Consequently, oil injection under the piston is the only cooling mechanism considered by the model. The heat transfer mechanism between the piston and the oil is very complex and difficult to investigate even with proper test rigs. The whole piston bottom inner surface is supposed to be involved in the heat exchange process through the interaction with the oil spray which is produced as a consequence of the high speed, high turbulence and chaotic relative motion between the oil jet and the piston. But, due to the typical piston geometry and jet orientation (toward the intake and/or the exhaust side), most of the heat exchange (with the highest exchange coefficient) takes place in the surface directly hit by the oil jet. Hence, as suggested and confirmed by the hardness measurement, the higher the distance between the considered area and the oil jets, the higher the temperature. Such distance can be measured on the piston, even if with a certain amount of uncertainty since the definition of the impingement area is quite arbitrary, and it can be considered as a parameter of the temperature model.

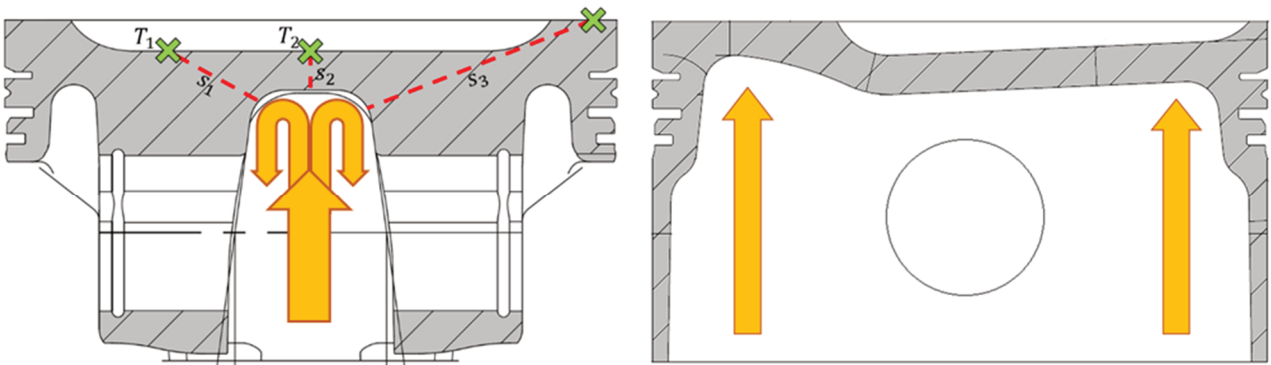


Figure 1.11 – Qualitative oil jets position and estimation of the measurement point distance from the oil-impinged surface.

- The ratio between the gas-exposed and the oil-impinged areas is unitary, which means that in stationary conditions the specific heat flux across the thickness is uniform, and the heat flux is mono-dimensional. Substantially, it is equivalent to a flat plate, but with differential thermal conductivity (because of the varying distance between the two sides in the real piston).

The result is a non-stationary finite-elements model (developed with the help of [28] and [29]), where the nodes are distributed along the thickness of the piston and an equivalent (calibratable) thickness is defining the location. The boundary conditions are the same for every location (thickness) considered:

- imposed heat flux on the gas side (Neumann condition)
- conductive heat transfer on the oil side (Robbins condition)

The temperature in the nodes  $T_t$  at time  $t$  are calculated by:

$$T_t = MM \setminus FF \tag{1.3}$$

With  $MM$  and  $FF$  are defined by:

$$MM = \frac{MC}{ts} + \alpha (MK + MH) \tag{1.4}$$

$$FF = \left[ \frac{MC}{ts} - (1 - \alpha)(MK + MH) \right] T_{t-1} + F \quad (1.5)$$

Where:

$\alpha$  defines the method: 0, 1, 0.5 for explicit, implicit and Crank-Nicholson, respectively

$ts$  is the time-step

$T_{t-1}$  is the temperature vector at the previous time-step  $t - 1$

$MC$  is the capacity matrix

$$MC = \frac{\rho c l}{2} \begin{pmatrix} 1 & 0 & 0 & 0 & 0 \\ 0 & 2 & 0 & 0 & 0 \\ 0 & 0 & 2 & 0 & 0 \\ 0 & 0 & 0 & 2 & 0 \\ 0 & 0 & 0 & 0 & 1 \end{pmatrix}$$

Where  $\rho$ ,  $c$  and  $l$  are the density, the specific heat and the elements length, respectively;

$MK$  is the conductivity matrix:

$$MK = \frac{\lambda}{l} \begin{pmatrix} 1 & -1 & 0 & 0 & 0 \\ -1 & 2 & -1 & 0 & 0 \\ 0 & -1 & 2 & -1 & 0 \\ 0 & 0 & -1 & 2 & -1 \\ 0 & 0 & 0 & -1 & 1 \end{pmatrix}$$

Where  $\lambda$  is the material conductivity;

$MH$  is the convective matrix:

$$MH = H_{oil} \begin{pmatrix} 0 & 0 & 0 & 0 & 0 \\ 0 & 0 & 0 & 0 & 0 \\ 0 & 0 & 0 & 0 & 0 \\ 0 & 0 & 0 & 0 & 0 \\ 0 & 0 & 0 & 0 & 1 \end{pmatrix}$$

Where  $H_{oil}$  is the convective coefficient at the oil-piston boundary;

$F$  is the vector of the loads:

$$F = \begin{pmatrix} q_{pist_t}\alpha + q_{pist_{t-1}}(1-\alpha) \\ 0 \\ 0 \\ 0 \\ H_{oil}T_{oil} \end{pmatrix}$$

$q_{pist_t}$  is the specific heat flux at the gas-piston boundary at time  $t$ ;

$q_{pist_{t-1}}$  is the specific heat flux at the gas-piston boundary at time  $t-1$ ;

$T_{oil}$  is the oil temperature.

As for the previous work [1.30] and as already mentioned, the mean value of the specific heat flux within the combustion cycle,  $q_{pist}$ , is imposed on the gas side and it is estimated by a linear correlation, to be calibrated, with the maximum pressure of the cycle. This is supposed to be valid in non-knocking combustions, while an additional contribution is given by knock, but with a local effect. For this engine and for the investigated operating conditions, the damage was observed in the exhaust side, so this is the location where knock occurs. Consequently, the knock-related heat transfer contribution is to be considered only in the exhaust side. Figure 1.12 reports the mean temperatures in the intake and in the exhaust side, even if the averages will no longer be considered for the aforementioned reasons, estimated by the hardness measurements for sets 7 and 8 (the same considered in Figures 1.7 and 1.8). In both sets, knock intensity is increasing from cylinders 5 to 8 (cylinders 5 are knock-free) and the general trend of the temperature is to be attributed to the maximum pressure increase, due to higher spark advance. The knock contribution to the heat transfer can be observed in the decreasing of temperature difference between the exhaust and the intake side as the knock intensity increases. Indeed, it can be noticed that the Pmax increase between cylinder 6 and 7 and between 7 and 8, for both sets, is very little, due to the steep knock behaviour. The temperature estimation on the intake side is linearly increasing with the maximum pressure, while on the exhaust side there is a further contribution increasing with the knock intensity. This is a further confirmation of the localized effect, both in terms of damage and increased thermal flux.

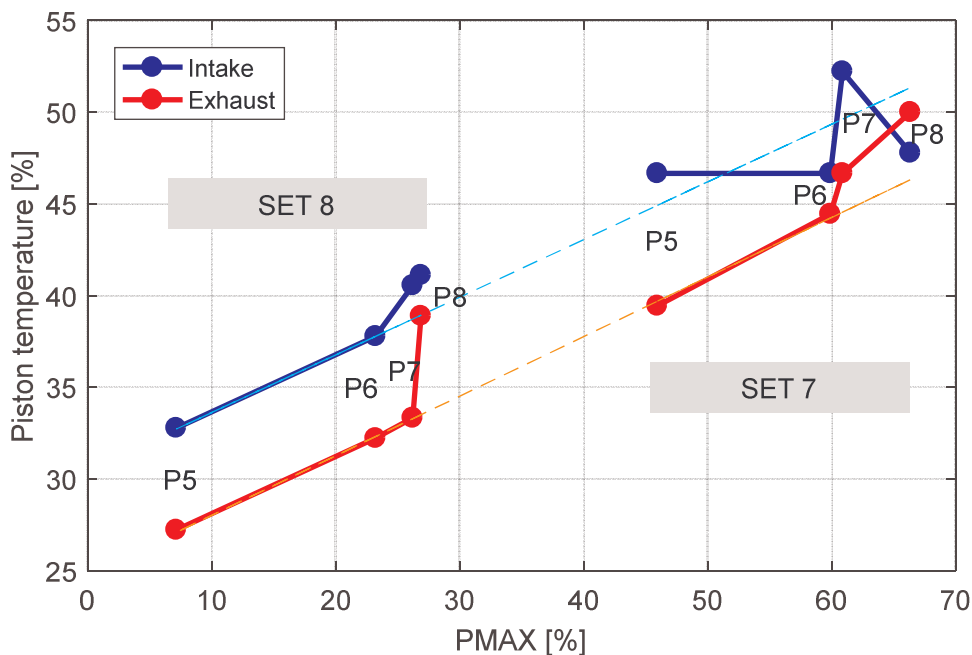


Figure 1.12 – Piston temperature in the intake and in the exhaust side depending on the maximum pressure level, for set 7 and 8.

The knock thermal contribution has been modelled as a multiplication factor, to be applied exclusively in the exhaust side, which linearly increases with knock intensity.

The equivalent thickness  $l$  is, in theory, a measurable value, but due to the simplified hypothesis and to the uncertainty in performing such measurement, it could bias the model calibration, or it can be a powerful calibration parameter. If this is the case, at least 1 of the 6 thickness values has to be fixed, not to over-parametrize the problem.

Since the data collected in the activity involves 2 different engine speeds, quantity which has not been mentioned until now, it can be considered as a further variable of the model. In this sense,  $q_{pist}$  is then a function of  $P_{max}$  and RPM, and  $H_{oil}$  is a function of RPM (or constant).

### 1.6.1 Oil convection coefficient estimation

In the described problem there are at least 2 unknown quantities:  $q_{pist}$  (or better its functional dependence on  $P_{max}$ ) and  $H_{oil}$ . The convection coefficient on the oil side or, equivalently, the specific power on the gas side needs to be imposed, in order to identify the other quantity.

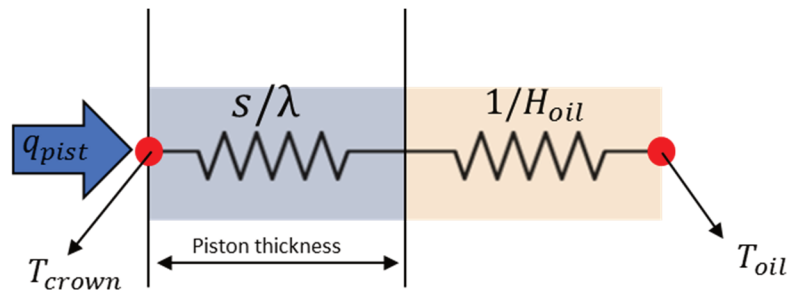


Figure 1.13 – Schematic representation of the heat transfer problem through thermal resistances series.

$$H_{oil} = \frac{1}{\frac{T_{crown} - T_{oil}}{q_{pist}} - \frac{s}{\lambda}} \quad (1.6)$$

The heat transfer problem is represented in Figure 1.13, where the piston and the oil-piston interface are 2 thermal resistances connected in series. In stationary conditions,  $H_{oil}$  can be calculated through Eq. \_\_\_ from piston temperature, piston thickness  $s$  and specific power  $q_{pist}$ .

By analysing data recorded with NTC (Negative Temperature Coefficient) technology, for the same engine, an estimation of  $H_{oil}$  has been calculated. In particular, the data used contains for different engine speeds:

- 4 piston crown temperature measurements
- Total power transferred to the water  $Q_{wall}$ , calculated on inlet-outlet water temperature difference and flow
- Oil temperature

By assuming the value of  $q_{pist}/q_{wall}$ , (i.e. the fraction between the heat transferred from the gas to the piston and the total power transferred to the water, including friction losses) and  $\lambda$ , and by estimating the values of  $s$ , 4 independent trends of  $H_{oil}$  can be calculated as a function of the engine speed, as described in Figure 1.14. The fraction between  $q_{pist}$  and  $q_{wall}$  has been chosen equal to 0.2. This hypothesis is not verified, but it is necessary to have an estimation of the heat transfer rate. An error on this parameter will affect all the following results, but not the applied approach.



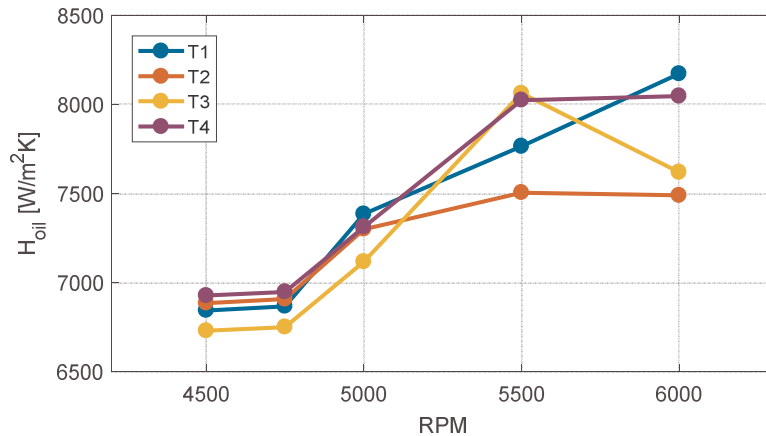


Figure 1.14 – Convective coefficient estimations considering 4 different temperature measurements, for different engine speeds.

The 4 estimations are very similar, both in terms of values and trends, confirming that the 1-D approach is feasible. The apparent dependence of the 4 convective coefficients on the engine speed visible in Figure 1.14, can be a consequence of the simplified approach, while the ratio  $q_{pist}/q_{wall}$  is probably varying with the engine speed as well. Because of this,  $H_{oil}$  has been supposed independent on engine speed and equal to  $7320 \text{ W/m}^2\text{k}$  (referred to the piston crown piston surface, being 1 the ratio between the surfaces).

### 1.6.2 Thickness estimation

In this section the method used to estimate the equivalent thickness for every measurement point is described. High accuracy is not required and cannot be expected, since, as mentioned, 5 thickness values over 6 will be calibrated and because of the simplified approach.

All the measurement points are very close to one of the 2 oil jets, so just the closest oil jet has been considered to estimate the piston thickness (the other option is to consider the parallel sum of the distances from both oil jets, with similar results). Using the mechanical 2-D drawing, distances in 2 perpendicular planes can be measured, then the total distance can be calculated applying the Pythagorean theorem.

In Figure 1.15 the method is described. The total distance,  $Int\_1\_xyz$ , can be directly measured from the cross-section view (left side of Figure 1.15). The minimum distance between the oil-washed surface and the measure point is considered. For measure points "2" and "3", distances are considered on the x-y plane (top-bottom view on the right) and on the x-z plane (cross-section on the left).

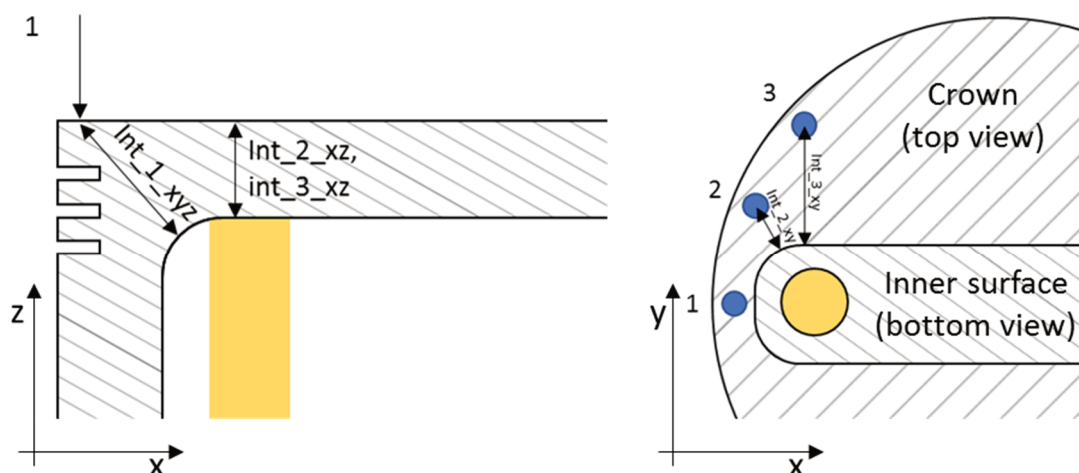


Figure 1.15 – Thickness estimation example.



In Table 1.2 the measured distances and the resulting total distance for the 6 points are reported.

Table 1.2 – Measured distances between the oil-impinged surface and the nominal hardness measurement locations, for every location.

measure point	Oil-measure point distances [mm]		
	xz	xy	total xyz
int_1	(13.1)	-	13.1
int_2	8.5	6.8	10.9
int_3	8.5	14.3	16.6
<b>exh_1</b>	<b>(8.5)</b>	-	<b>8.5</b>
exh_2	4.8	6.1	7.8
exh_3	4.8	12.6	13.5

Now, the total thickness corresponding to point 1 on the exhaust side (exh\_1) is considered as having the lowest uncertainty and it has been fixed (equal to 8.5 mm), while the other values will be identified by the calibration process (as explained before, at least one thickness value has to be imposed).

In Table 1.3 all the quantities involved in the model are summarized and categorised as measured, known or to be calibrated.

Table 1.3 – Overview of the quantities involved in the piston temperature model.

Parameters/functions	Value	Unit	Measured quantities	Unit
$\rho$	2740	$kg/m^3$	HV_int_1	HV
$c$	890	$J/kgK$	HV_int_2	HV
$\lambda$	140	$W/mK$	HV_int_3	HV
s_int_1	?	mm	HV_exh_1	HV
s_int_2	?	mm	HV_exh_2	HV
s_int_3	?	mm	HV_exh_3	HV
s_exh_1	8.5	mm	$T_{oil}$	$^{\circ}C$
s_exh_2	?	mm	Engine speed	RPM
s_exh_3	?	mm	Pmax	bar
$H_{oil}$	7320	$W/m^2K$	MAPO	bar
$q_{pist}(Pmax, RPM, MAPO)$	?	$W/m^2$		

### 1.6.3 Specific thermal flux correlation

The specific power model,  $q_{pist}(Pmax, RPM, MAPO)$ , is defined as a linear function of Pmax and RPM; moreover, for the exhaust side, it is multiplied by a term linearly increasing with MAPO:

$$q_{pist} = (a Pmax + b RPM + c)K_{MAPO} \quad (1.7)$$

Where

$$\begin{aligned} K_{MAPO} &= 1 && \text{in the intake side} \\ K_{MAPO} &= \max(MAPO - 4, 0)d && \text{in the exhaust side} \end{aligned} \quad (1.8)$$

And  $a, b, c, d$  are to be identified.

$K_{MAPO}$  definition is thought as a line with positive slope, passing through  $MAPO = 4$  and saturating at 0. The meaning is that cycles with a MAPO value lower than 4 (a brute and arbitrary threshold to distinguish knocking and non-knocking cycles) are not increasing the nominal  $q_{pist}$  value, while higher values of MAPO are amplifying such amount. Figure 1.16 gives a qualitative idea of the resulting function.

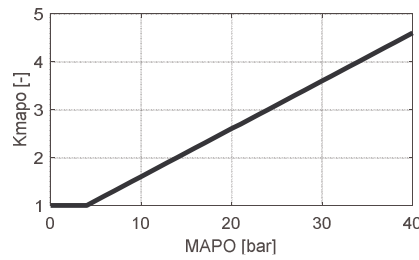


Figure 1.16 – Heat transfer enhancer depending on knock intensity.

In Figure 1.17 the calibration process is summarized. The recorded combustion indexes (Pmax and MAPO) are vectors describing the whole pressure history (one value for every combustion cycle) experienced by the piston. The piston temperature model estimates the temperature history (one value for every cycle) for every measurement point. Then, the material hardness decay model (refer to “1.3.2.1 Hardness Measurements” for more details) estimates the hardness history for every measurement point and finally the residual hardness values are compared to the measured ones. This applies in parallel to every tested piston. To minimize the cost function, which is defined as the sum of all the absolute errors, for every piston, for every measure point, `fminsearch` function from the MATLAB optimization toolbox has been used.

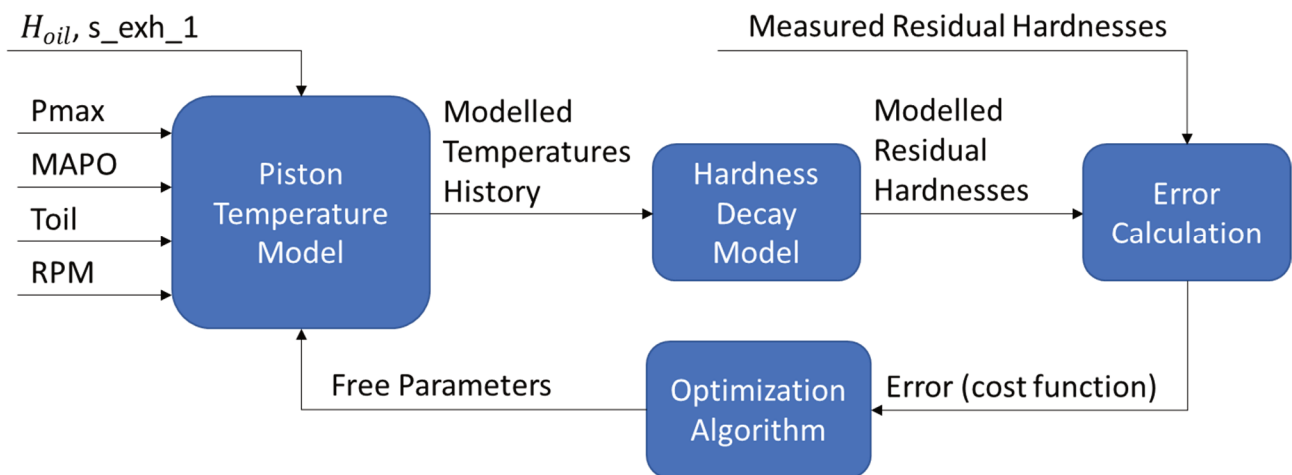


Figure 1.17 – Calibration process for the piston temperature model.

The calculation of the whole hardness history, for a given temperature profile, is the most time-consuming. Potentially, the average temperature over time (for every measure point) can be considered instead of the whole history, if the modelled temperature is substantially stationary, and the direct calculation (1 iteration) of the residual hardness can be performed as a function of the mean temperature and the duration. But since the temperature profile is an oscillating signal, and it results in a slightly lower residual hardness w.r.t considering the constant temperature profile because of the non-linear behaviour of the material, the cycle-by-cycle temperature and the corresponding hardness decay have been preferred and considered.

Since the calculations were supposed to be iterated many times during the activity, some attention has been paid on the efficiency of the codes. To have an idea of the performance of the code (and of the real-time capability), an i-7 2.3 GHz laptop performs  $1.7e5$  cycles per second calculating the cycle-by-cycle temperature and  $1.1e5$  cycles per second estimating the corresponding hardness decay.

### 1.6.4 Piston temperature model calibration results

The following figures show the comparison between the measured and the modelled hardness values after the model calibration, the correspondent error and the position of the measure point on the piston crown. In the left plot, the starting hardness is also reported, which has been measured before mounting the pistons on the engine. Vickers hardness measurements, those on the piston crown, have been converted to Brinell hardness, through the correlation described Figure 1.5. This way, the starting, residual and modelled hardness are expressed with the same units.

The data presented is divided into sets (4 pistons for every sets) and the coloured band on the background stands for the engine speed: blue for 4500 RPM and red for 6000 RPM.

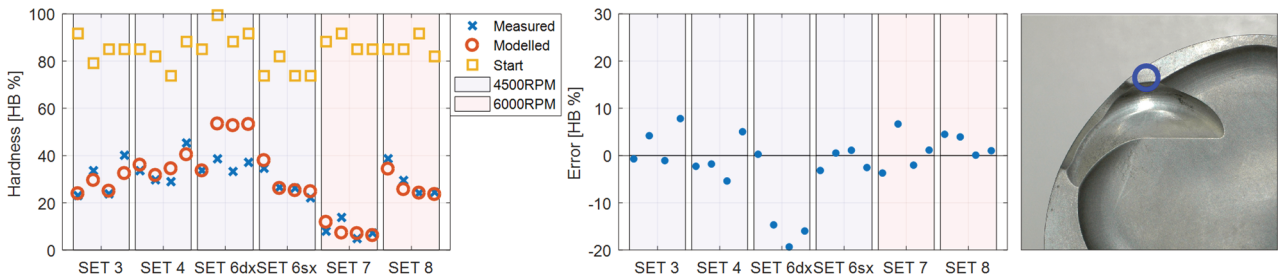


Figure 1.18 - Intake position 1: measured and estimated hardness values and the corresponding error (normalized units).

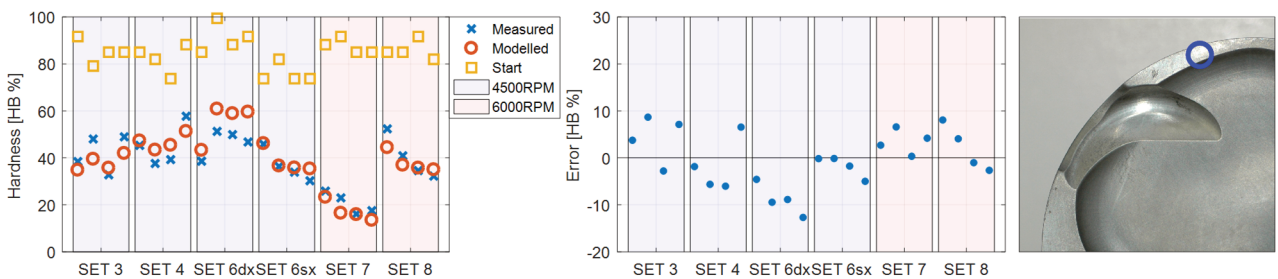


Figure 1.19 - Intake position 2: measured and estimated hardness values and the corresponding error (normalized units).

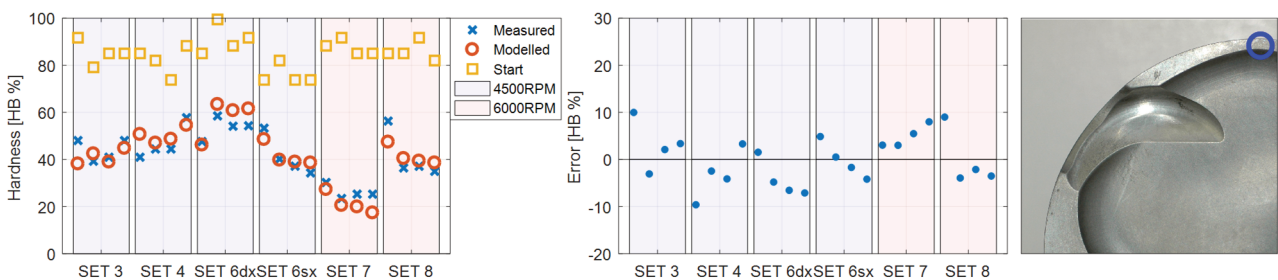


Figure 1.20 - Intake position 3: measured and estimated hardness values and the corresponding error (normalized units).

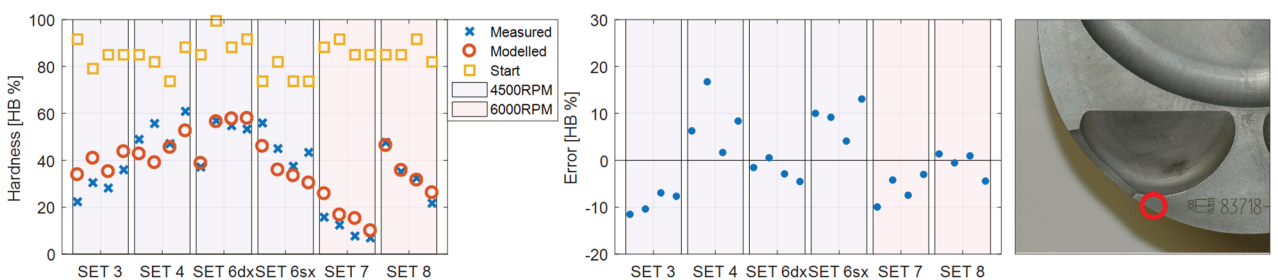


Figure 1.21 - Exhaust position 1: measured and estimated hardness values and the corresponding error (normalized units).

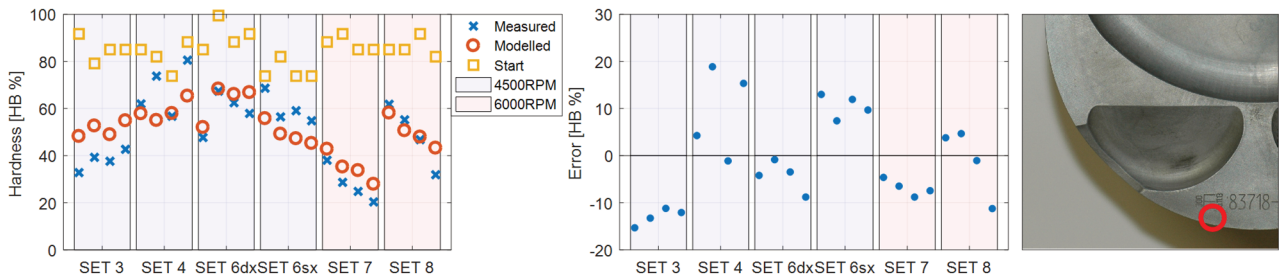


Figure 1.22 - Exhaust position 2: measured and estimated hardness values and the corresponding error (normalized units).

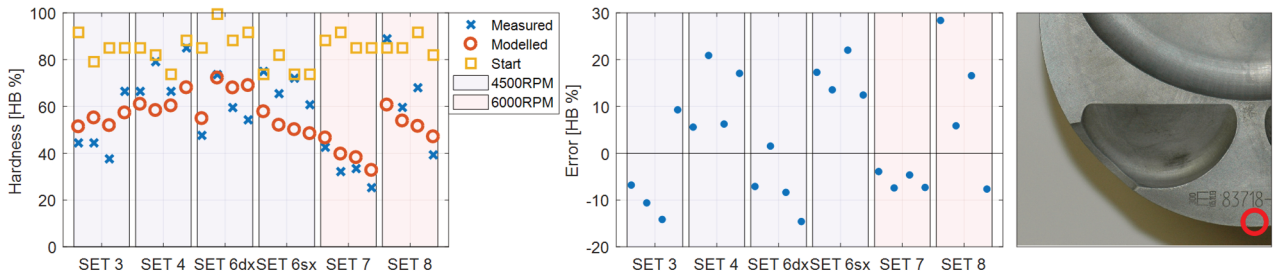


Figure 1.23 - Exhaust position 3: measured and estimated hardness values and the corresponding error (normalized units).

To interpret the data, it has to be kept in mind that the hardness values considered correspond to a single measurement for position 3 (both in the intake and in the exhaust), and to the average of 2 measurements for positions 1 and 2, because of the symmetry.

Some of the measurements, for example in position 3 in the exhaust, leave some doubt: in one case the residual hardness is higher than the initial value, while in other cases the hardness reduction is much more lower than expected.

This can be attributed to several causes, as explained in sub-section “1.3.2.1 Hardness Measurements”:

- measurement uncertainty due to the very small volume interested by the Vickers imprint;
- hardening during operation because the material is under-aged;
- low repeatability (or high sensibility) of the material around the lowest temperature which enables the material aging. Note that position 3 in the exhaust is characterized by the lowest temperature levels.

So, even if a relatively high dispersion of the experimental data is expected, the model calibration should be able to capture the mayor trend. The results are more reassuring if the mean values for every side (intake and exhaust) are considered, as shown in Figures 1.24 and 1.25.

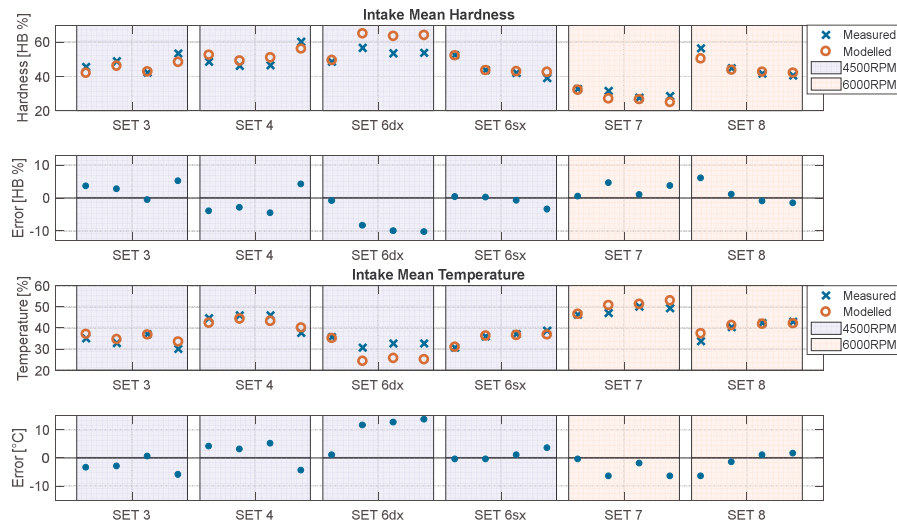


Figure 1.24 – Calibration results: mean intake hardness, temperature and corresponding error (normalized) values.

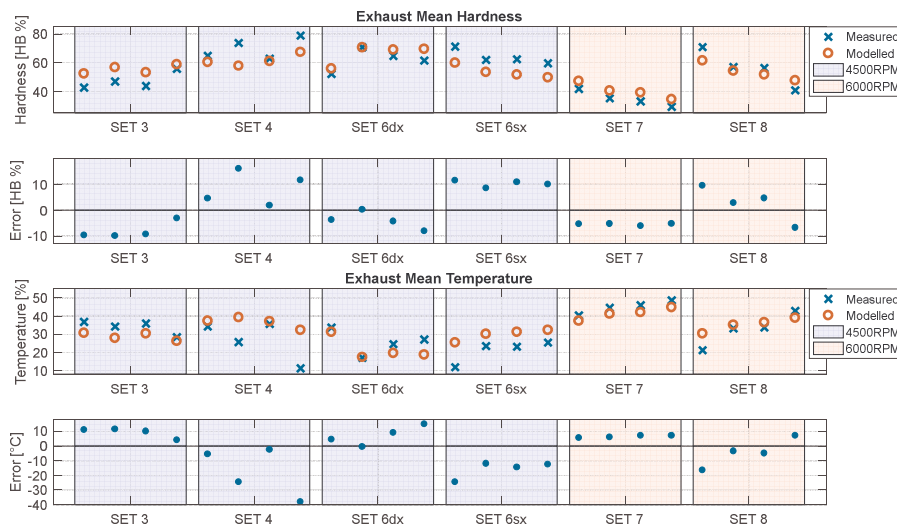


Figure 1.25 - Calibration results: mean exhaust hardness, temperature and corresponding error (normalized) values.

Table 1.4 – Comparison between the identified and the measured piston thickness values.

Piston Thickness Values		
measure point	Measured	Identified
int_1	13.1	13.0
int_2	10.9	14.0
int_3	16.6	16.6
exh_2	7.8	10.2
exh_3	13.5	13.2

Table 1.4 reports the values of the identified values for the piston thickness, used in the model to estimate the thermal resistance for every measurement location. As can be noticed, the values are extremely close, except for 2 cases, to the values measured from the drawings. This means that the model can be used, in principle, to estimate the temperature of every location within the piston, if a similar thickness measurement can be performed.

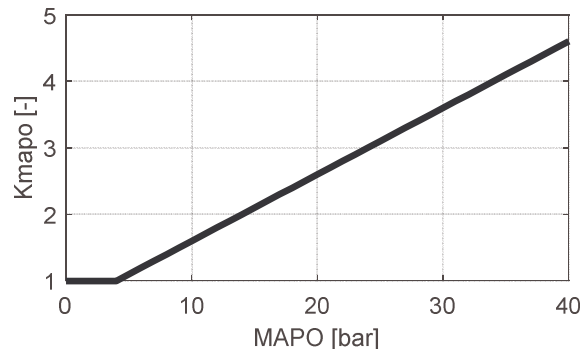


Figure 1.26 – Identified heat transfer multiplier ( $K_{MAPO}$ ) as a function of MAPO.

Figure 1.26 describes the identified heat transfer multiplier,  $K_{MAPO}$ , which quantifies the increase of the heat transferred to the piston (in the exhaust side, by hypothesis) as a function of the knock intensity index MAPO. What emerges from the calibration of such parameter, is that single knocking combustions heavily increase the heat transfer rate (as widely detailed in literature): 14 bar of MAPO double the heat transferred to the exhaust side, with 35 bar of MAPO the heat transferred is 4 times the value which corresponds to a non-knocking combustion.

These results are in good accordance with the analysis described in [1.21], where a linear dependence with similar slope between the integral heat transfer within the cycle and the MAPO index is observed. This apparently huge amount of extra heat transferred to the piston by knocking combustions, needs to be weighted by the knock intensity distribution function, to quickly estimate an average increase of the thermal power and then of the piston temperature. Then, since for “reasonable” knocking levels the frequency of high knock intensity cycles is relatively diluted, the mean effect on piston temperature is not dramatic, even if not negligible and so calibratable.

#### 1.6.5 Oil pressure variation effect

In the previous section, the calibration of the piston temperature model has been presented, in which set 9 has not been considered. This is because this test operated with a lower oil pressure (3 instead 4.5 bar of relative pressure), with a consequent lower piston cooling and piston temperatures higher than expected. Moreover, the engine operated with high fuel RON (100), which allows to reach higher pressure levels (and so piston temperature) for a given knock intensity level. Hence, the combined effect of lower oil pressure and high RON fuel induced the highest piston temperatures experienced in this activity.

For this test, the piston boundary condition on the oil side (i.e. the convective coefficient) has been reidentified, to calibrate the pressure oil effect on the cooling conditions. All the other parameters previously identified are unchanged. So, this test can be considered as a partial validation of the piston temperature model.

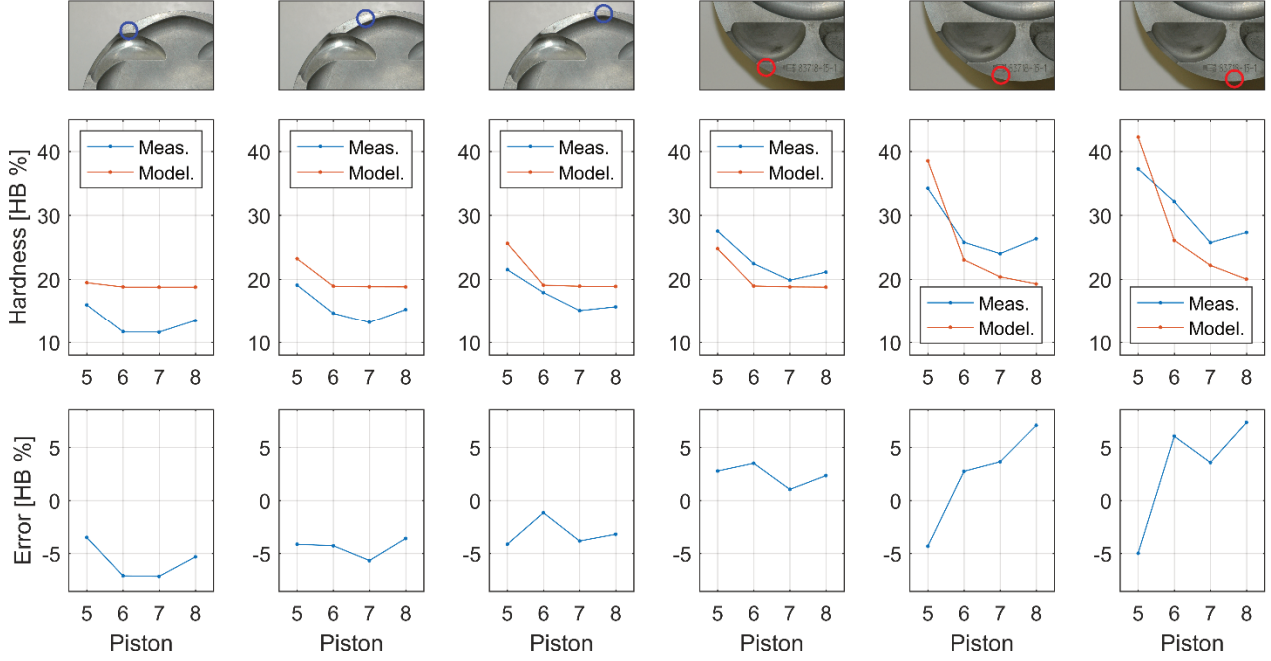


Figure 1.27 – Set 9 results: comparison between measured and estimated hardness (normalized) values and the corresponding error.

In Figure 1.27 the results of this dedicated recalibration are exposed, showing small errors between the measured and the predicted hardness values.

Some values reached the asymptotic lower value, so no sensitivity on the piston temperature is actually expected for these measurements.

The convective coefficient identified for this set is lower than the one identified on the previous calibration process, as expected (because of the lower oil pressure level). The convective coefficient reduction can be evaluated w.r.t. the reduction in the oil pressure. Bernoulli equation for incompressible flows can be considered, in which the oil velocity, responsible for the mass flow and the convective coefficient, depends on the square root of the pressure difference between the oil pump outlet and the crankcase (i.e. the oil pressure expressed as a relative pressure):

$$\frac{K_{oil_{set\ 9}}}{K_{oil_{set\ 3...8}}} = \frac{6.176\ e3}{7.32\ e3} = 0.84 \approx \frac{\sqrt{3}}{\sqrt{4.5}} = 0.81 \quad (1.9)$$

Where  $K_{oil_{set\ 9}}$  is the identified convective coefficient for set 9 and  $K_{oil_{set\ 3...8}}$  is the identified convective coefficient for sets 3 to 8. The prediction of the convective coefficient as a function of the oil pressure cannot be assumed a priori, since the interaction between the oil and the bottom piston surface is very complex and a change in the oil velocity can affect the heat exchange at many levels (mass flow, impingement surface, etc.). Anyway, the reduction of  $K_{oil}$  is very similar to the reduction of the expected flow speed according to Bernoulli, confirming the physical content of the model.

The extension of the piston model temperature to this exceptional operating condition can be useful to estimate in a small range what is the effect of the oil pressure on the piston cooling condition, and furthermore allows the damage model to be applied to this set as well.

### 1.6.6 Piston skin temperature

Before developing the piston temperature model, it has been hypothesized that the skin temperature has minor variations within the cycle. Now this statement can be verified by supposing a plausible specific thermal flux profile during the cycle and by resolving the proposed model with a fine piston domain discretization and an appropriate small time-step.



The model has been applied to a thickness of 15 mm, discretized by 250 elements, with different thermal flux profiles, characterized by different mean and peak values; in Table 1.5, the mean value and the oscillation amplitude of the piston skin temperature within the cycle are reported.

Table 1.5 – Skin temperature average and oscillation, depending on the mean and peak specific flux.

Skin Temperature Average				Skin Temperature Swing			
Mean specific flux [W/m <sup>2</sup> K]	Max specific flux [W/m <sup>2</sup> K]			Mean specific flux [W/m <sup>2</sup> K]	Max specific flux [W/m <sup>2</sup> K]		
		5E+5	6.5E+5			8E+5	5E+5
5.0E+06		218.1	248.0	-		8.1	8.9
1.0E+07		218.1	248.0	278.0		13.1	14.5
1.5E+07		218.1	248.0	278.0		15.5	17.6

As well known, the thermal flux estimation, both in terms of mean value and even more in terms of the profile shape, is hard and uncertain. That is why different profiles are tested, characterized by mean values compatible with the values identified by the previous model calibration (even if the mean value is not affecting very much the temperature swing), while peak values are taken from the literature. The highest value is found in [1.31], where flux measurements are taken during knocking combustions and peak values of the thermal flux profile reach 15 MW/m<sup>2</sup>, Nates proposes similar values in [1.20]; the resulting temperature oscillation values are not really negligible.

Then, the case characterized by the highest temperature swing (19.6 °C) is considered, and the hardness decay history is calculated both considering the estimated skin temperature profile and the correspondent constant mean value (both reported on the left side of Figure 1.28), for an exposure duration of 5 hours. As described on the right side of Figure 1.28, the difference in the final residual hardness is negligible (≈0.5 HB). However, this kind of analysis is based on the assumption that the material has not dynamic behaviour (the frequency of the temperature oscillation has no effect), which cannot be verified.

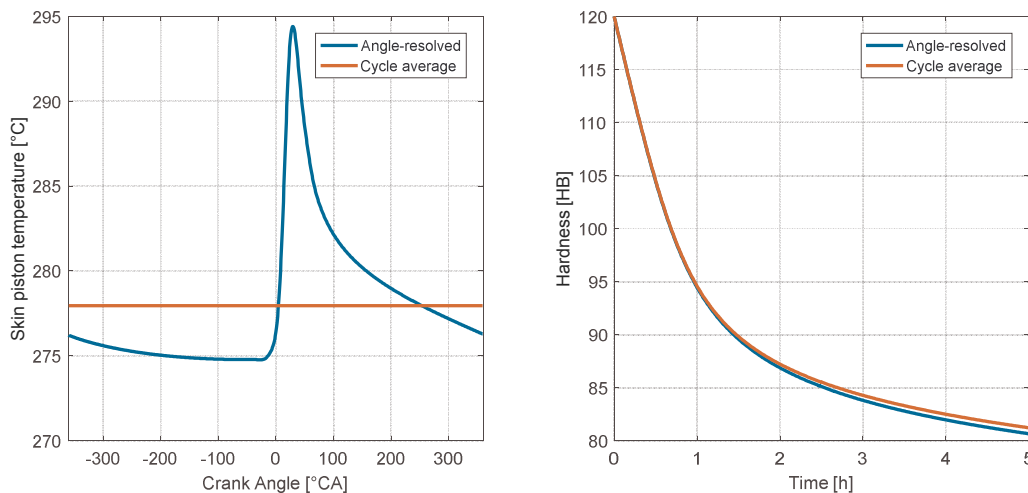


Figure 1.28 – Temperature profile and correspondent mean value within the cycle (left) for the highest temperature oscillation considered in Table 1.5 and the correspondent hardness decay history (right).



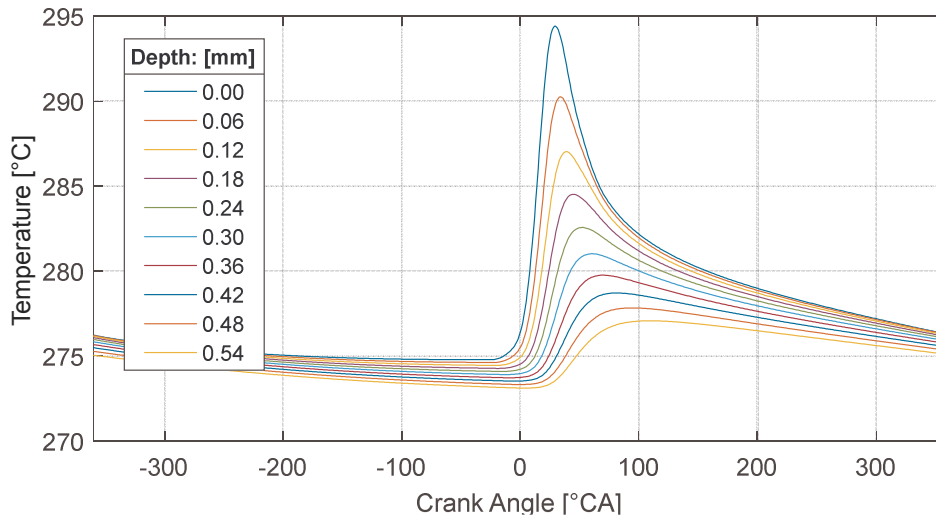


Figure 1.29 – Profile temperature within the cycle for different depths.

In Figure 1.29, the temperature profile within the cycle is reported for different depth values, showing as the highest temperature gradient decays in about 0.5 mm. Consequently, even if the temperature gradient were very high and the calculated hardness gradient not negligible, the measured hardness is actually an averaged valued of different layers of material, which would inevitably filter such gradient.

Hence, the temperature oscillation within the cycle can be neglected while calibrating the piston temperature model by using hardness measurements, since these are basically unaffected.

On the other hand, with high values of the thermal flux peak, which possibly locally can be even higher than the highest considered value, the temperature gradient is extremely high and the impact on the resulting mechanical stress can be effectively important, as hypothesized by Nates in [1.20];

To have a quantitative idea of the induced stresses, the right side of Figure 1.30 describes the most critical transversal stress profile (w.r.t. the piston axis) along the slab coordinate  $y$  (described on the left side of Figure 1.30, which maximum value is 15 MPa) for the temperature field described in Figure 1.29.

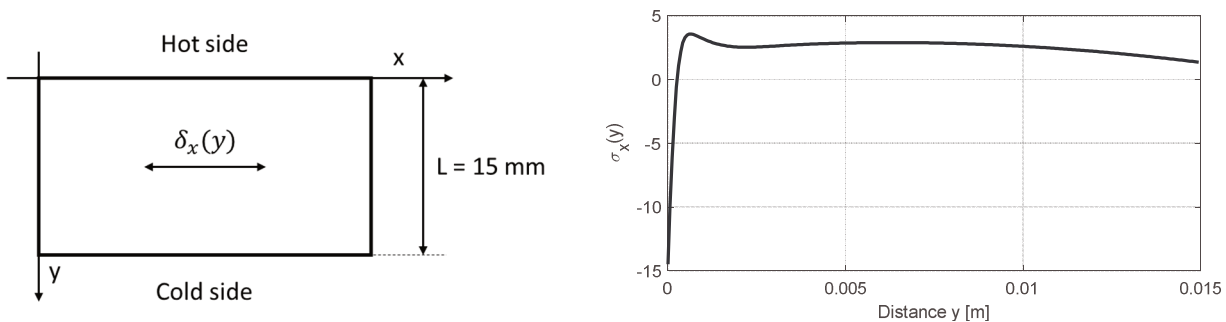


Figure 1.30 – Considered reference frame (left) and transversal stresses across the slab because of the supposed temperature gradient (right).

The stress calculation is made according to Timoshenko [1.32], as suggested by Nates:

$$\delta_x(y) = \frac{\alpha E}{1 - \nu} T(y) + \frac{1}{L} \int_0^L T(y) dy + \frac{12 y}{L^2} \int_0^L T(y) y dy \quad (1.10)$$

## 1.7 Knock damage model

The induced damage, on the assumptions made in the previous sections, is supposed to depend on piston temperature and, of course, on knock intensity.

Both for control purposes and to avoid any arbitrary statistical index, the damage should be calculated for every cycle, depending on the instantaneous temperature.

The proposed idea is to define a MAPO threshold to classify damaging events, which is supposed and confirmed by the experiments (see Figure 1.8) to be decreasing with temperature. Then, cycles below such threshold are harmless, while the others should damage depending on their intensity.

The idea of defining a threshold comes from the yield concept for a ductile material, since in knocking combustions the piston is supposed to be subjected to a mechanical stress, and eventually by the thermal stress which both should depend on the same knock intensity.

Material hardness, since it is directly related to the material properties, should be considered in the model to estimate the induced damage. Currently it is not possible to identify both instantaneous temperature and hardness weights in the material susceptibility to knock damage. Substantially, a hotter piston has lower material resistance both because of the instantaneous and the integral temperature effects on piston material properties. Specific tests, for example by using pre-aged pistons, are needed to quantify such contribution.

As described in Figure 1.31, the damage model can be thought as a simplified stress-strain diagram: in the elastic domain knock does not damage the material, while over the yield limit, which corresponds to a MAPO value (to be identified), knock leaves its indelible mark, supposed proportional to the distance between the measured index and the threshold.

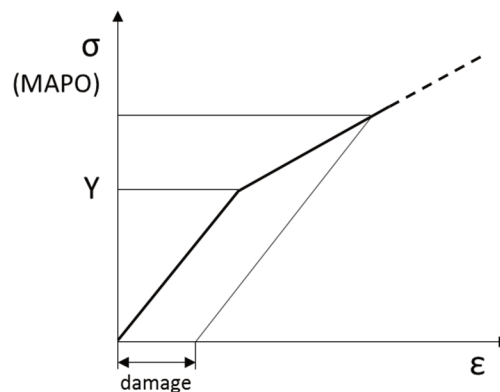


Figure 1.31 – Stress-strain-like diagram, representing the damage model concept.

At the current stage, the slope of the plastic behaviour is supposed to be unitary, so that the damage induced by the single combustion event corresponds to the positive difference between the MAPO value and the current threshold (depending on the piston temperature).

What emerges from the calibration attempts is that here there is (another) inevitable indeterminacy (in addition the one regarding the heat transfer): it is not possible to absolutely discern what are the damaging cycles (i.e. the corresponding MAPO values). This is because of the stochastic nature of knock and because it is characterized by a continuum in terms of intensity. We can consider two different knocking levels (see Figure 1.32), which can be synthetically evaluated by a statistically robust average MAPO percentile, but even better they can be fully and well described by the log-normal probability density function (which is widely used in literature to describe knock distributions), as shown in the first graph. Suppose distribution 1 generated a certain damage level, while distribution 2 did not. Now, there is the question of how many cycles, or better which fraction, are over a certain MAPO value, to try to find the MAPO threshold which discriminates between damaging and inoffensive cycles. The answer can be sought in the survival function, reported in the second plot, which describes the fraction of the distribution that overcomes the generic value of MAPO. For a better visualization, the logarithmic scale is adopted.

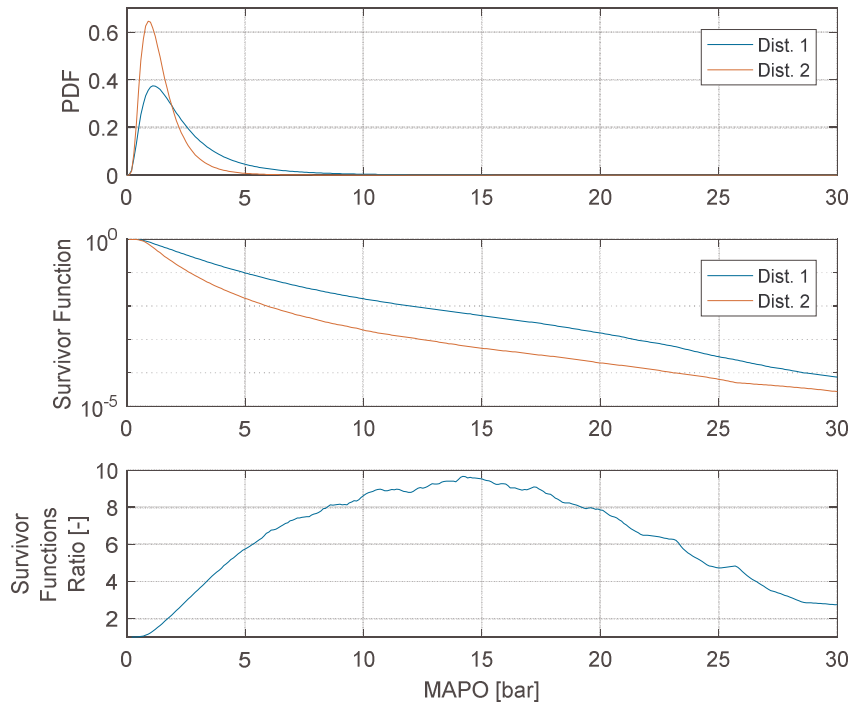


Figure 1.32 – Statistical comparison between 2 different knock intensity distributions: PDF functions, survivor functions and survivor functions ratio.

In the last graph, the ratio between the 2 survivor functions is reported: as can be noted, the question about the threshold cannot be answered, since this ratio does not reveal a clear abundance of a certain intensity range in the distribution 1 w.r.t. distribution 2 to which attribute the responsibility for the induced damage. Substantially, both distributions cover the same intensity range (which is theoretically not limited), and distribution 1 has permanently and almost constantly a higher probability to have values over a generic MAPO value throughout the domain. So, potentially damage can be attributed to cycles with MAPO higher than 2 bar as well as higher than 20 bar, with similar results.

It can be asserted (even if not properly demonstrated) that it is mathematically impossible to uniquely identify such threshold, unless by generating combustions with the desired and constant knock intensity.

The desired threshold synthesizes the composition of 2 transfer functions: one is the material resistance, which relates stress and damage, while the other defines the relation between the oscillations measured by the pressure sensor and the real stress on the piston surface.

This last would be determined if the desired threshold could be identified.

Anyway, this does not mean that the problem cannot be modelled, instead there are infinite solutions (even easier), which result in a loss of physical significance.

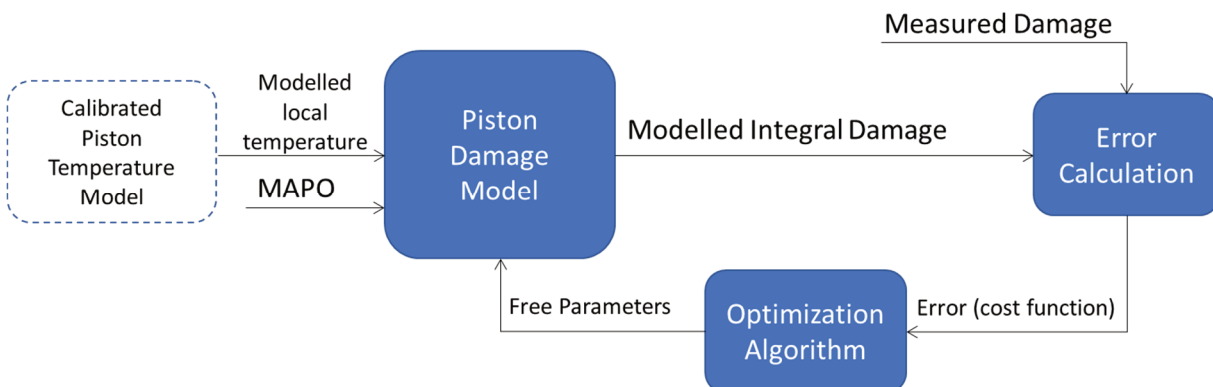


Figure 1.33 – Damage model calibration process.

Figure 1.33 shows the calibration process, which is very similar to the one adopted for the previous model. Model inputs are the measured MAPO and the temperature histories, cycle by cycle. Since the temperature model can estimate the temperature for different locations, depending on the equivalent thickness, it is reasonable to consider the temperature of the damaged location. Such area has not been involved by hardness measurements, since the measurement would interfere with the damage itself; moreover, the hardness test would require special setup due to the complex crown surface.

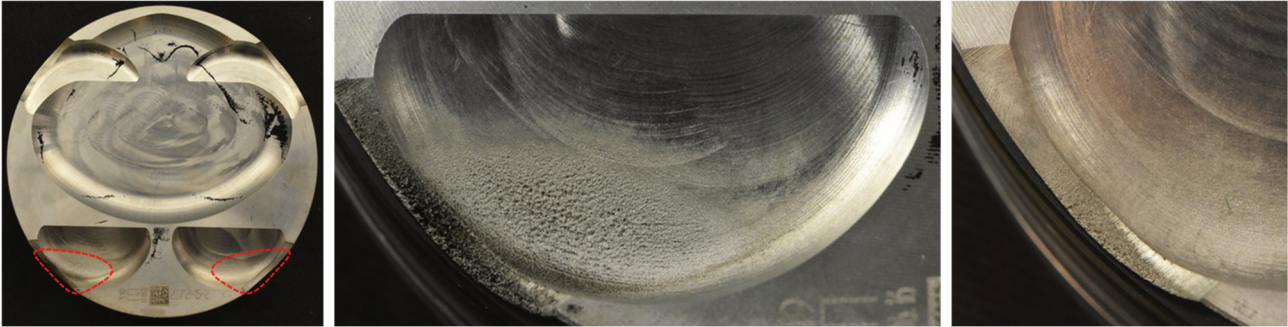


Figure 1.34 – The area typically interested by erosion induced by knocking combustions is highlighted on the left. Two examples of erosion in the highlighted area in the 2<sup>nd</sup> and 3<sup>rd</sup> pictures.

After calibrating the temperature model with the 6 values available, the temperature of the area highlighted in the left picture in Figure 1.34 has been calculated by estimating (by the geometry) the equivalent thickness.

The damage model consists in a temperature dependent MAPO threshold. If the function is supposed to be linear, 2 parameters are to be identified. As already explained, the problem is undetermined and potentially only the (negative) slope of the function can be determined. However, both parameters have been identified, starting from a supposed reasonable initial solution.

The cost function (CF) is defined to maximize Pearson's correlation,  $\rho$ , between the measured and the modelled damage D:

$$CF = 1 - \rho(D_{meas}, D_{mod}) \quad (1.11)$$

### 1.7.1 Damage model calibration results

Figure 1.35 reports the results of the damage model calibration: x-axis represents the modelled damage (integral value of MAPO values over the threshold), which can be still expressed in bar, while the y-axis describes the measured damage levels.

Pistons without any measured damage have not been considered in the calibration not to bias the cost function, since a dead band zone (with no correlation) is expected (and desired) where the modelled damage is positive while the measured is null.

Neither pistons from SET 4, which experienced some pre-ignition cycles (which are supposed to be much more damaging), have been considered during the model calibration. Evidently, the model is not able to completely capture the effect on pistons of this kind of combustion, since they are always outliers (the model underestimates the damage for these pistons), whatever the calibration approach.

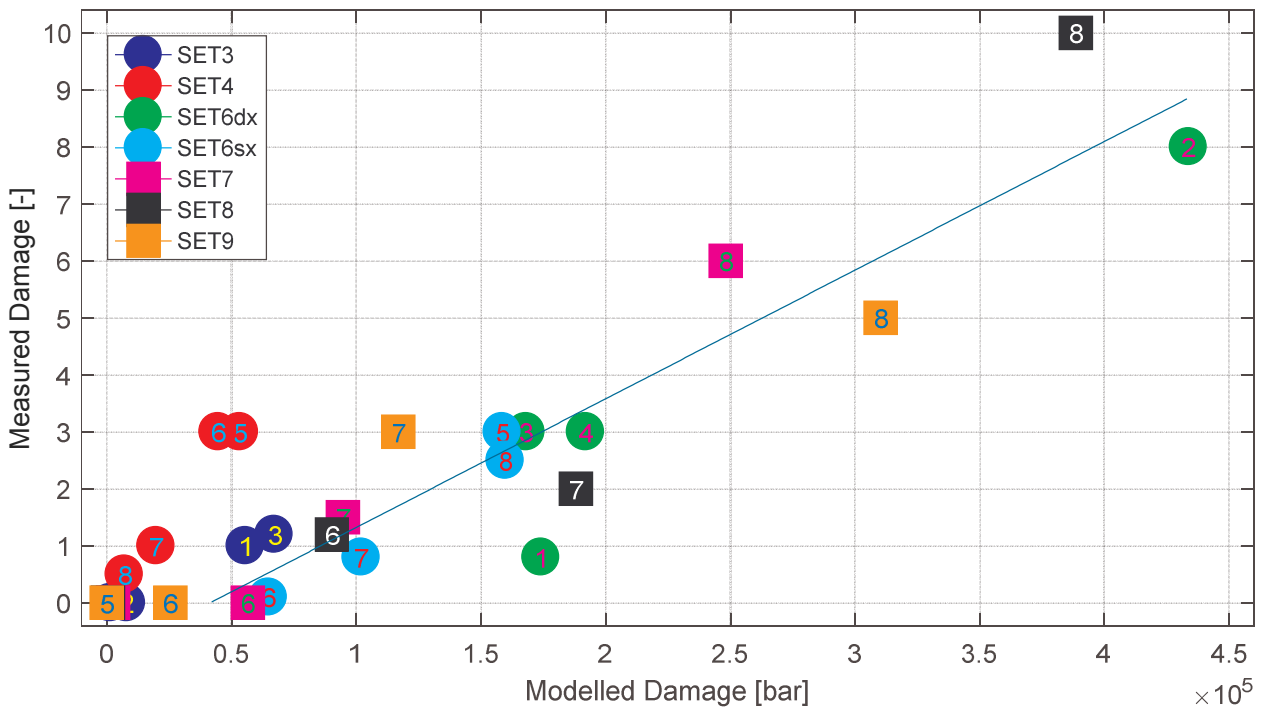


Figure 1.35 – Calibration results of the damage model. The x and the y axes are the modelled and the measure damage levels, respectively.

The resulting MAPO threshold as a function of the piston temperature, reported in Figure 1.36, has been identified in order to maximize the correlation between the modelled and the measured damage.

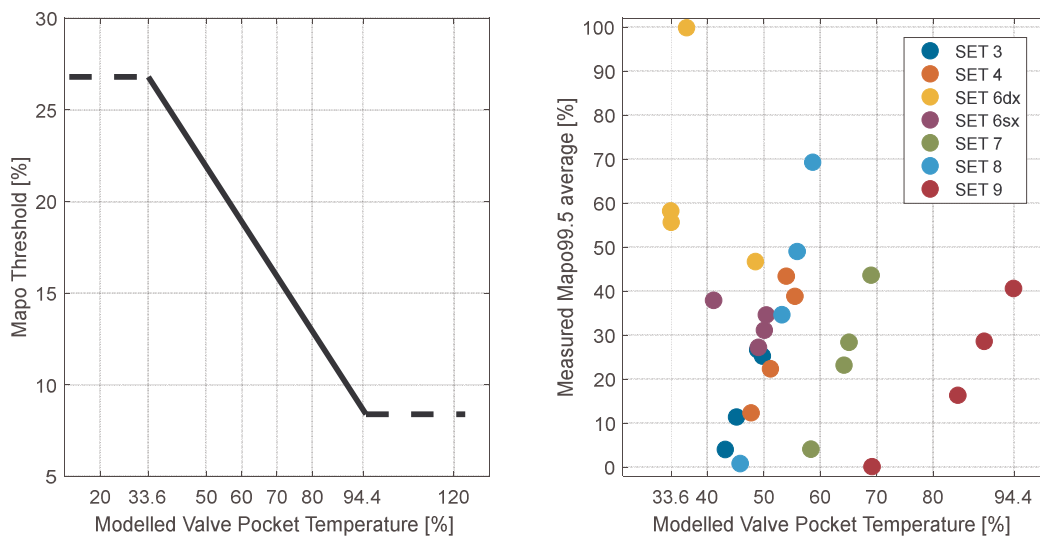


Figure 1.36 – Left: temperature-dependent MAPO threshold, identified by the damage model calibration. Right: mean modelled temperature in the exhaust valve pocket and mean MAPO 99.5 % for sets 3 to 9.

The interesting result is the decreasing value of the threshold as the piston temperature increases, confirming the observations made on SET 7 and SET 8 (Figure 1.8).

The threshold can be identified only in the temperature range where the pistons operated on average (between 33.3 and 94.4 %), which is described on the right side of Figure 1.36. Out of this interval the thresholds are currently clipped to the extreme values. In future developments, the material resistance shape will be adopted, allowing a relatively confident extrapolation out of the calibration range.

Figure 1.37 reports the correlation map as a function of the high and low temperature MAPO thresholds. It can be noticed that the surface has a ridge with a relatively constant correlation along a  $y = kx$  (where  $x$  and  $y$  are the high and low temperature MAPO thresholds), which describes the mentioned uncertainty of the problem. Also, it can be observed that the surface contains a log-normal behaviour, characteristic of the MAPO distribution, which is itself the cause of the indeterminacy.

This degree of freedom can be exploited when defining the control strategy. By varying both thresholds along the ridge, the dead-band along the modelled damage (visible in Figure 1.35) can be modified: by considering higher thresholds the dead band can be reduced or eliminated, so that the regression line can pass through the origin. But, for control purposes, it is convenient to adopt lower thresholds, so that if the targeted induced real damage is null, the controller is however able to estimate and control a non-saturated value of the estimated damage (the control implementation of the model will be detailed in the following chapter). In other words, the adoption of lower thresholds, allows to control the low frequency of high knock intensity cycles through the estimation of the higher frequency of low knock intensity cycles. By varying the selected solution, the conversion parameter between measured and modelled damage (i.e. the regression function considered in Figure 1.35) varies as well, so it needs to be defined coherently with the temperature-dependent threshold.

The optimal solution found (represented on the left side of Figure 1.36 and highlighted on the left side of Figure 1.37) provides a relatively wide dead-band, so this solution is considered.

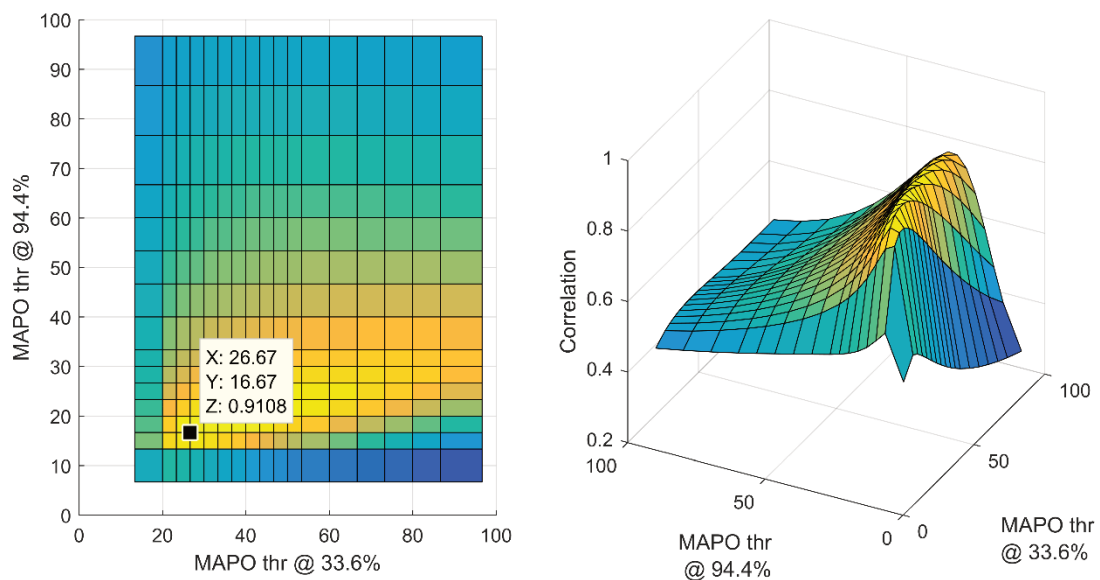


Figure 1.37 – Correlation between the measured and the modelled damage depending on the high and low temperature thresholds.

### 1.8 Control implementation

The proposed damage model is based on the hypothesis that the damage is accumulated cycle by cycle, so there is a linear dependence on the number of damaging cycles and so on the operation time. Up to now, the discussion dealt with the total induced damage, which is a quantity that cannot be properly controlled unless a life cycle of the engine (of the piston) is defined. Supposing an aggressive spark advance control strategy (i.e. a strategy which actively improves efficiency by controlling knocking conditions), it is clear that the targeted damage, the corresponding knock intensity and engine performance has to be spread throughout engine life. Indeed, a condensed damage generation and the corresponding performance increase within a short time would be a very inefficient way of using this model.

So, the control strategy target should be a (constant) damage speed, which finally generates the desired damage level upon completion of the design life cycle.

Supposing a predefined engine life,  $Life_{tgt}$  (expressed in seconds) and a target modelled damage,

$Damage_{tgt}$  (expressed in bar, which corresponds to a real induced damage, according to Figure 1.35), a damage speed target  $DS_{tgt}$  can be defined, as described in Equation (1.12):

$$DS_{tgt} = \frac{Damage_{tgt}}{Life_{tgt}} \left[ \frac{bar}{s} \right] \quad (1.12)$$

Similarly, the estimated (instantaneous) damage speed can be defined as:

$$DS_{est} = \frac{Damage_{est|P}}{P} \left[ \frac{bar}{s} \right] \quad (1.13)$$

Where P is the considered period (e.g. 10 seconds or the time corresponding to 100 cycles) and  $Damage_{est|P}$  is the cumulated damage within the period P estimated by the model.

At first instance, a simple closed loop can be thought, as depicted in Figure 1.38:

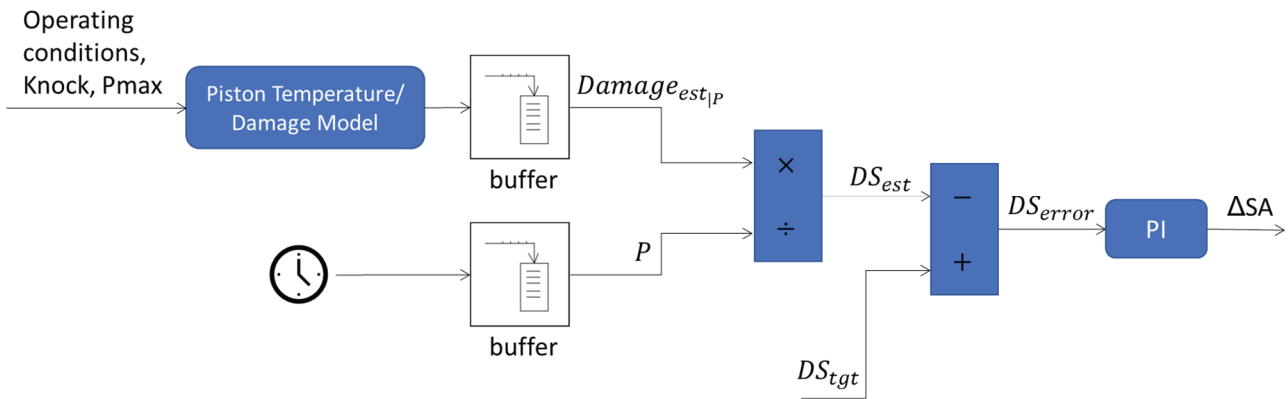


Figure 1.38 – Example of closed-loop control strategy based on the damage speed estimation.

Where a Proportional-Integral (PI) controller, in which the main contribution is due to the integral term, calculates a spark advance correction depending on the error between the estimated and the target damage speed.

To make the control more accurate and suitable for transient conditions, in parallel to the closed-loop strategy, a feed-forward spark advance calculation can be performed, but it requires the adoption of a knock model. The idea is described in Figure 1.39: depending on the operating conditions and knock intensity, the piston temperature model estimates the temperature of the piston location usually interested by damage (exhaust valve pockets, in this case) and based on this, the MAPO threshold between safe and damaging intensities (reported in figure 1.36) is assigned.

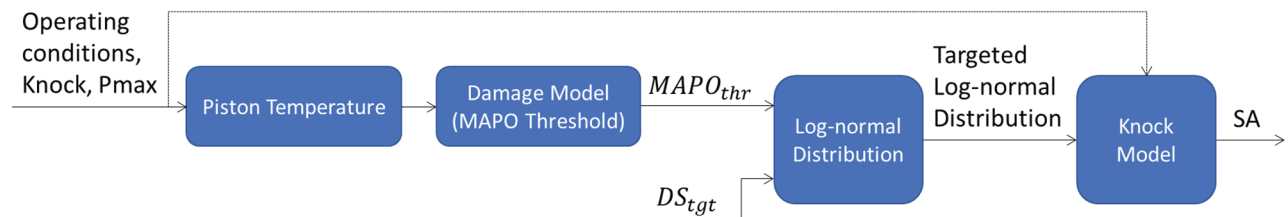


Figure 1.39 – Example of feed-forward spark advance calculation, for the given piston temperature (MAPO threshold) and damage speed target.

Then, given the MAPO threshold and the combustion frequency (i.e. engine speed), for a generic knock intensity (lognormal) distribution it is possible to calculate the knock damage speed. Consequently, it is



possible to identify the knock distribution (within the  $\infty^1$  possible distributions, depending on the spark advance, for the given operating condition) which generates the desired target speed and finally, by inverting the knock model, the targeted knock distribution is converted in the corresponding spark advance.

Several approaches are available in literature and can be adopted to model knock intensity. Supposing the most general approach, where the model is able to describe the log-normal distribution expected for the generic operating condition and the applied spark advance, the average damage per cycle can be calculated through Equation (1.14):  $PDF$  is the probability density function,  $\Delta MAPO$  is the interval used to discretize the MAPO domain and  $PF$  is the probability function.

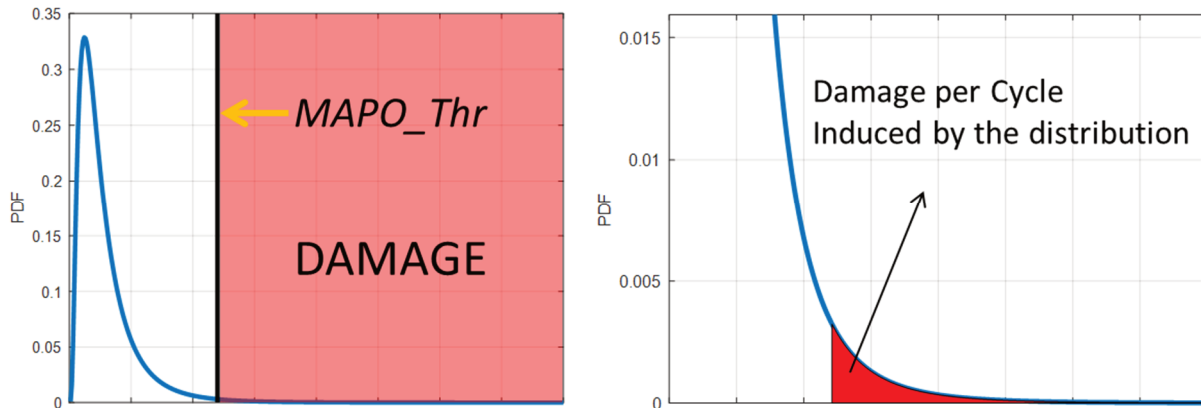


Figure 1.40 – Damage per cycle associated to the MAPO distribution for the given MAPO threshold.

$$Damage\ per\ cycle\ [bar] = \int_{THR}^{+\infty} (PDF\ \Delta MAPO) dMAPO = \int_{THR}^{+\infty} PF\ dMAPO \quad (1.14)$$

### 1.9 Validation

Validation tests have been carried out, by implementing a closed loop strategy like the one described in Figure 1.38 and targeting a predefined damage speed. In the test, set 10 sx, two different RON fuels (95 and 100) have been used alternatively during the operation, to highlight how the controller is able to control different knock intensities depending on the knock resistance of the fuel. Specifically, with a higher RON, a lower knock intensity is expected, due to higher pressure level and piston temperature.

In Figure 1.41, 100000 cycles operation is reported, from the 7.5 hours long total operation. Specifically, the trends of Pmax, MAPO and MAPO995 percentile, estimated piston temperature (in the exhaust valve pocket), the damage speed and the cumulated damage are described. The controller controls the mean damage speed to an almost constant value, described by the slope in the bottom plot, while limiting the instantaneous damage speed (calculated over a buffer of 500 cycles) described in the fourth plot. It can be noted that there are basically 2 levels of maximum pressure (high and low), corresponding (respectively) to the 2 different fuels (100 and 95 RON). Since the piston temperature, visible in the third plot, is affected by the controller reacting to the fuel type, the MAPO threshold varies and so the resulting MAPO percentile (2<sup>nd</sup> plot): it is slightly higher with lower maximum pressure (lower RON).



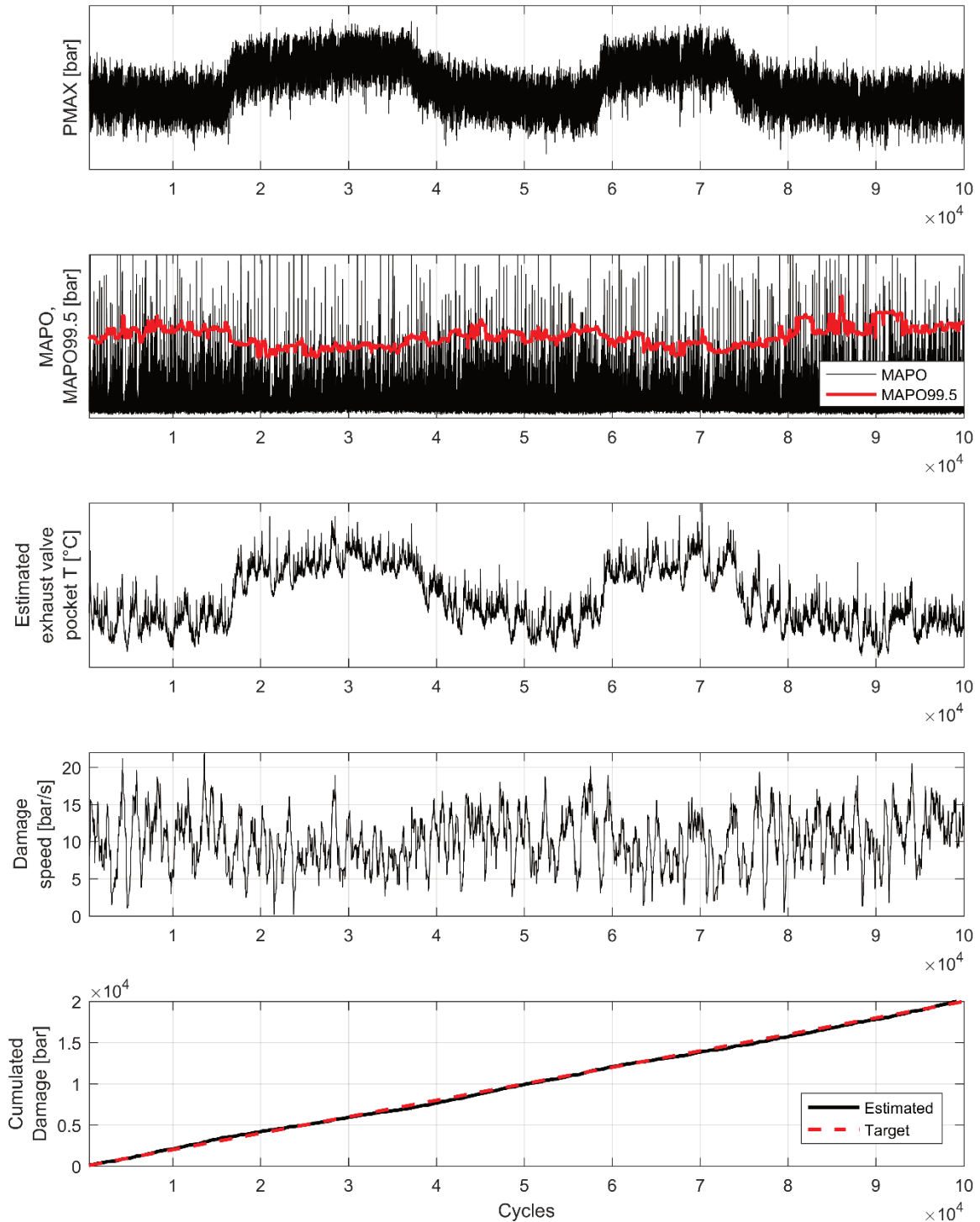


Figure 1.41 – Set 10 sx, maximum pressure, knocking level, piston temperature and damage estimation.

### 1.9.1 Piston temperature model

In Figure 1.42 and Figure 1.43, the comparison between the measured and the modelled hardness values and the corresponding temperature error are reported, both for the intake and the exhaust side. Hardness values are reported in the Brinell scale, as previously done, by converting the measured Vickers hardness. It is important to remember that Vickers hardness measurement are affected by a relatively high uncertainty. Anyway, the comparison shows a good match between modelled and measured values. The lowest hardness values, for this operation time (7.5 h), are out of range for the decay function reported on the left

of Figure 1.2. Moreover, for the lowest hardness values, close to the plateau of the material, the temperature estimation is extremely influenced by measurement errors. This is why, for some of the measurements, the temperature error is apparently very high or not reported.

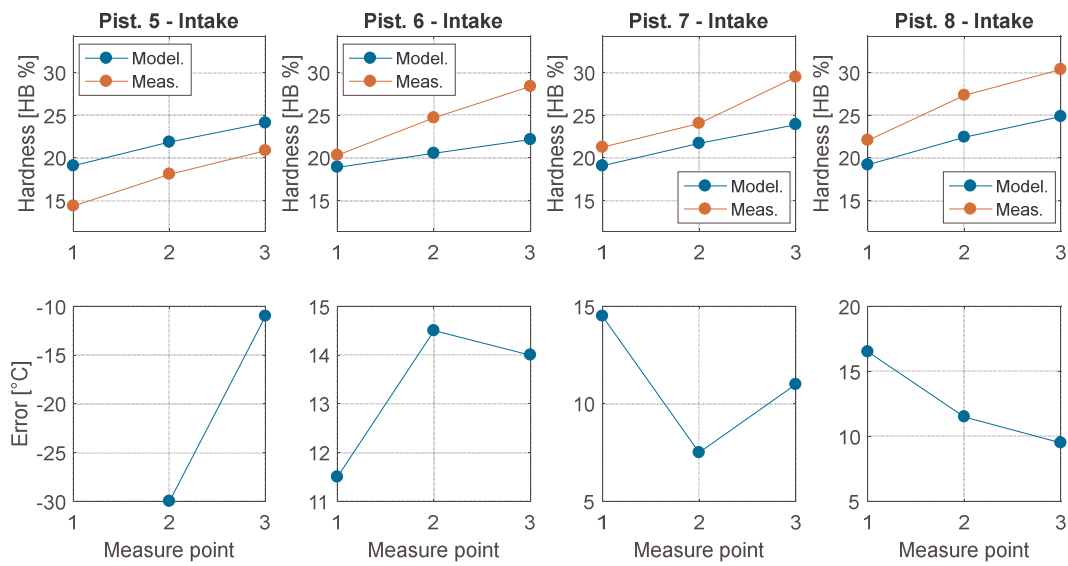


Figure 1.42 – Set 10 sx, measured and modelled hardness values and the corresponding temperature estimation error on the intake side.

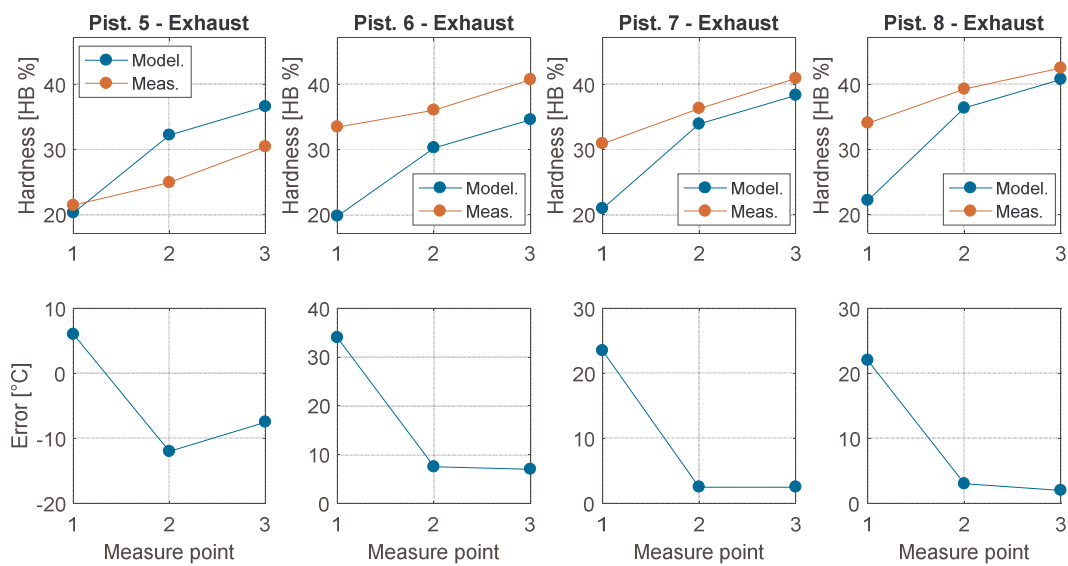


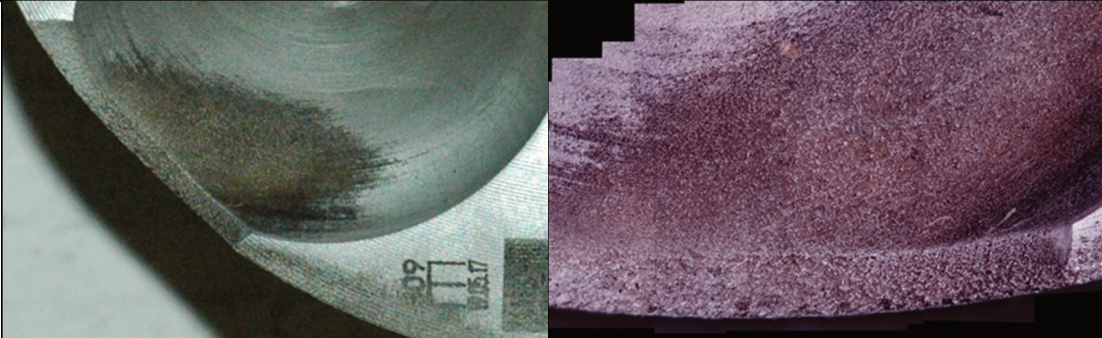


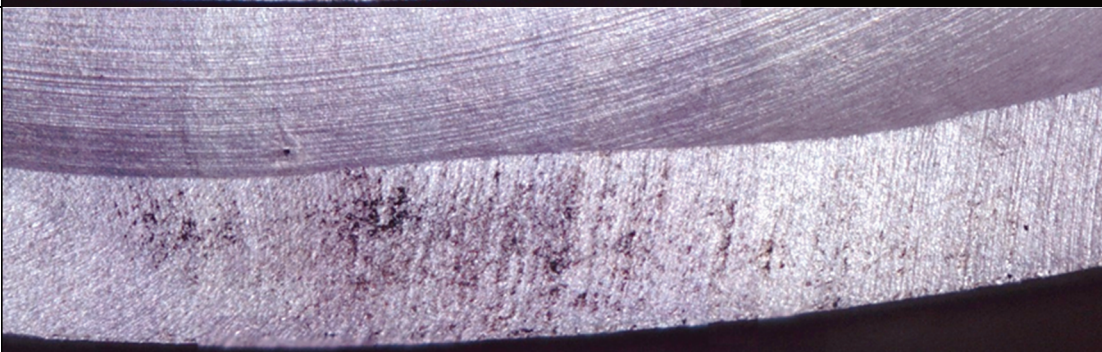
Figure 1.43 - Set 10 sx, measured and modelled hardness values and the corresponding temperature estimation error on the exhaust side.

### 1.9.2 Damage model

The damage model is then used to calculate the cumulative estimated damage, which should coincide with the targeted value. This correspondence is not perfectly achieved because the definition of the filters used to calculate the MAPO index during the real-time and the post-processing are different (and this difference is not avoidable at the moment). In particular, the two filters have different band-width and this difference has been compensated inside the controller by applying a multiplying factor to convert the real-time MAPO to the correspondent off-line value. Since the difference lies in the frequency domain and it is compensated by varying the intensity of the resulting index (and because the pressure sensors have slightly different frequency responses), such compensation is not perfect. Anyway, the targeted and the off-line calculated cumulative damage are very close, and they would coincide if the same filter is used.

The pictures in Table 1.7, describe the induced damage on the 4 tested pistons and the correspondent erosion index values are reported in the right column, showing a decreasing damage from piston 5 to 8.

Table 1.7 – Induced erosion pictures and erosion index in pistons from set 10 sx.

Piston		Erosion
5		4
6		2.5
7		2.4
8		1.5



In Figure 1.44, the off-line calculated cumulative damage and the erosion index (from the previous table) for set 10 sx are superimposed to the now known graph describing the correlation between the 2 indexes for all the pistons used for the model calibration.

As can be seen, the results of this validation test are very well aligned with the previous tested pistons and with the resulting regression function.

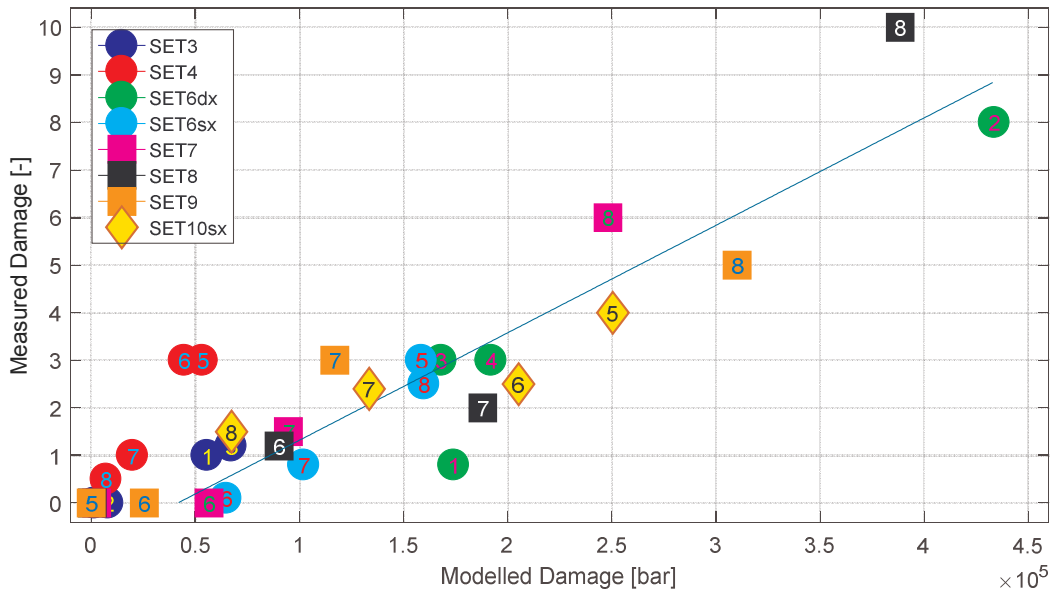


Figure 1.44 – Damage model validation: the yellow diamond-shaped markers represent the measured and estimated damage levels w.r.t. the pistons used for the model calibration.

### 1.9.3 Heat flow estimation

As discussed in “1.6.1 Calibration approach”, the estimation of the heat flux across the piston and the convective coefficient on the oil side, are affected by high uncertainty. It would be very useful to measure at least one of these quantities for higher accuracy and predictivity of the proposed models. With the same tools and methods presented up to now, one attempt has been made to estimate the temperature gradient and then the thermal flux across the piston, through Vickers hardness measurements. Eventually other attempts on other pistons can be done to statistically improve the results. In Figure 1.45, the intake and the exhaust sides (on the left and on the right, respectively) of the middle section of the same piston are reported, where a grid of measure points has been applied.

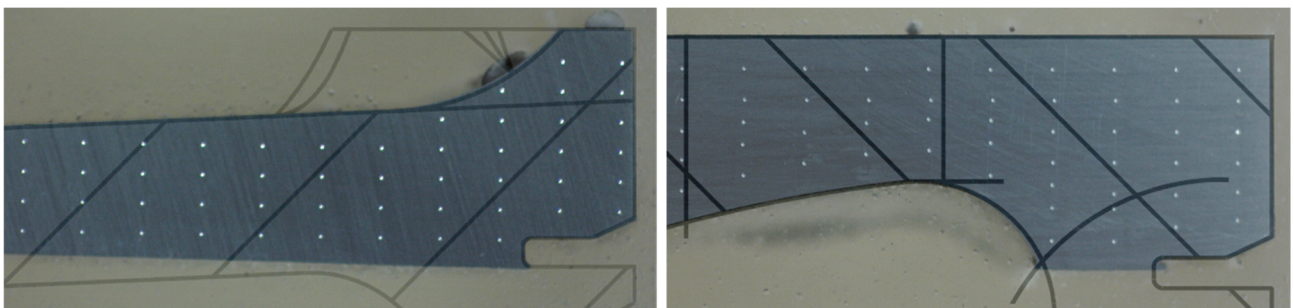


Figure 1.45 – Hardness measurement matrixes in the piston section; intake and exhaust sides on the left and right, respectively.

The technical drawing has been superimposed on the specimen pictures, to be used to dimensionally describe the measure grid. In particular, this is piston 1 of set 6 dx, which experienced an average maximum pressure of 41 % and a mean MAPO 99.5 of 46.5 %. This piston had been previously cut along the first ring groove plane, this is why the oil-impinged surface is not available on the intake side.

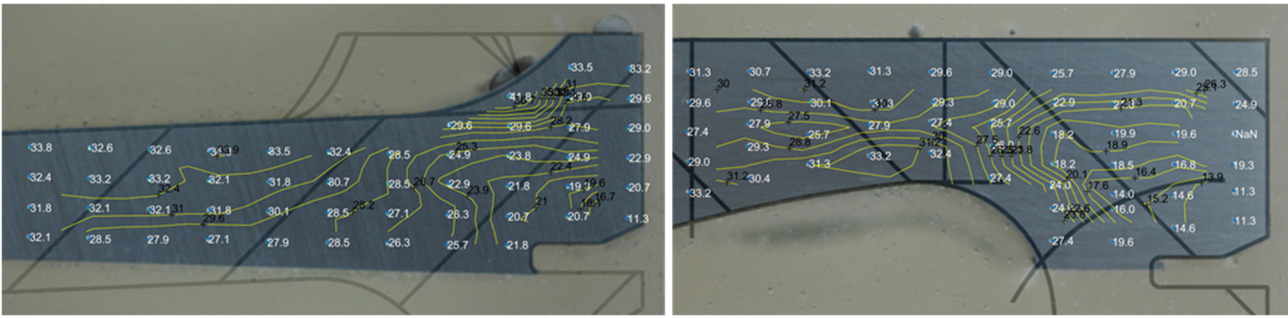


Figure 1.46 – Normalized temperature field estimated by hardness measurements in the piston section; intake and exhaust sides on the left and right, respectively.

Figure 1.46 describes the (normalized) temperature values estimated by the Vickers hardness measurements, to quantify the temperature gradient.

On the intake side (left picture in Figure 1.46), the expected gradient towards the oil-impinged surface and towards the first ring can be noted, even if this second direction of the heat flux is neglected in the piston temperature model proposed before. One measurement (41.8 %) suggests an unjustified very high local temperature gradient.

On the exhaust side (right picture in Figure 1.46), a non-physical result is obtained, where the oil-impinged surface is hotter than the upper layers. This unexpected and well-defined behaviour is hard to explain, unless by assuming a low repeatability and non-uniformity of the material decay, probably depending on the forging process (the oil-impinged surface is not machined after the forging).

So, both on the intake and on the exhaust side, the temperature estimation are not sufficiently robust nor accurate to define a temperature field to calculate the correspondent heat flux field. More data is required to achieve the desired result from this kind of analysis.

Anyway, the high number of measurements on both specimens should partly hide the real value of the average thermal flux passing through the piston. To highlight this information, the temperature field can be fitted with a linear function, like

$$T = T_0 + x T_x + y T_y \quad (1.15)$$

Where  $x$  and  $y$  are the spatial coordinates and  $T_x$  and  $T_y$  are the corresponding partial differentials of the temperature, expressed in  $K/m$ .

Then, the total thermal flux can be calculated as

$$F = \lambda(T_x + T_y) = \lambda \nabla T \quad (1.16)$$

Where  $\lambda$  is the thermal conductivity of the piston material and  $\nabla T$  is the temperature gradient.

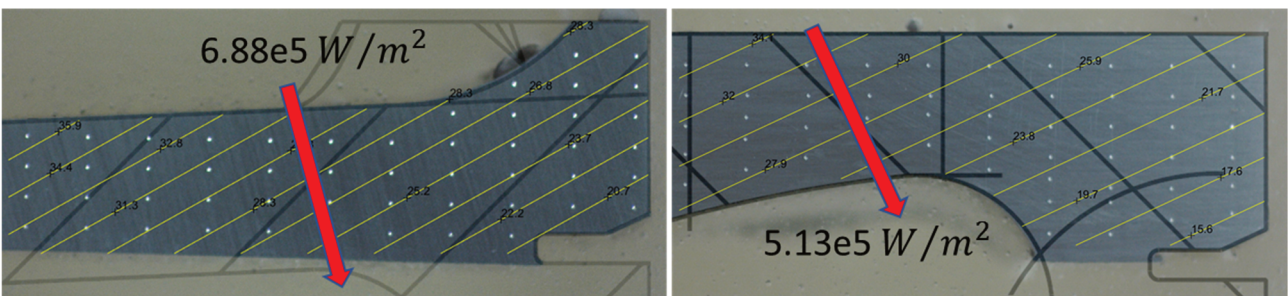


Figure 1.47 – Linear temperature field and corresponding estimated thermal flux; intake and exhaust sides on the left and right, respectively.

The results of this simplified approach are reported in Figure 1.47: the average fluxes are  $6.88e5$  and  $5.13e5 \text{ W/m}^2$  on the intake and the exhaust side, respectively.

Now, these values can be compared with the values expected by the specific flux model, described in “1.6.3 Specific thermal flux correlation” and reported in Figure 1.48.

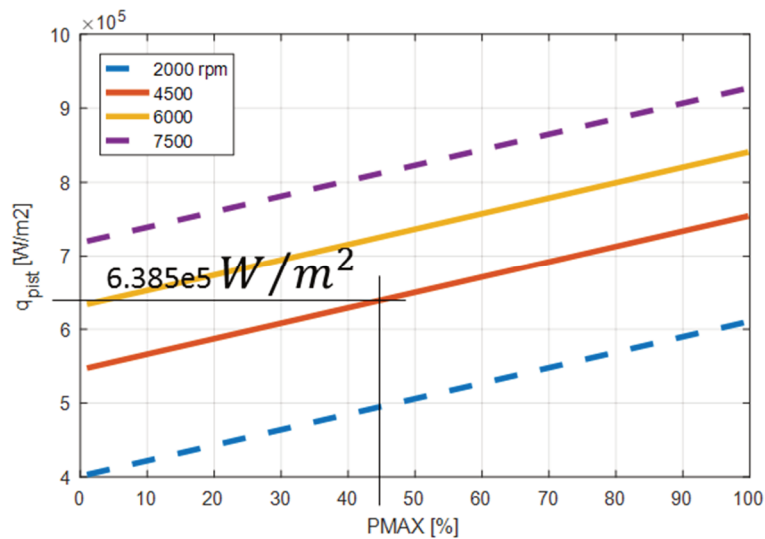


Figure 1.48 – Specific thermal flux correlation as a function of the (normalized) maximum pressure; the value corresponding to piston 1 of set 6 dx is highlighted.

The nominal modelled value, net of knock contribution and so valid for the intake side, is  $6.385e5 \text{ W/m}^2$ , very close to the value estimated from the linear temperature gradient in Figure 1.47 for the intake side. The exhaust side is supposed to experience a higher value of the thermal flux, because of the knock effect (which is supposed to act on the exhaust side only), while the measured flux says the opposite. This is caused by the simplified approach (linear fitting) and by the measurement uncertainty. For example, by ignoring the unexpected higher temperatures on the oil side, the gradient and so the flux would be higher. Anyway, this partial validation confirms that the thermal correlation used is very close to the “real” value.

This analysis also confirms that the cooling mechanism through the rings is not negligible, and it needs to be considered in the next developments of the piston temperature model.

## 1.10 Conclusions

The described research activity is focused on the understanding of the damage mechanisms involved by knocking combustions, with the aim of consciously controlling knock levels, reliability and efficiency. The observed damage, induced by controlled knocking conditions, is related to the measured knock intensity and to the piston temperature, which influences piston material mechanical properties. The physical content allows the model to be adapted to different engines or variants of the same engine, with minor recalibration effort.

Then, the model can be used to directly measure the damage speed during the engine operation and to control knock intensity, dosing the desired final damage, which can be even null, throughout the defined life time of the engine.

The variables involved in the model, can suggest how the targeted knock level and consequently the resulting engine efficiency, can be qualitatively influenced by the piston cooling conditions, piston geometry and high temperature material properties.

The obtained results can deeply change the way engines are usually calibrated: for example, since piston temperature increases with engine speed, for a given load, the model indicates that the knock level considered to calibrate the engine should be decreasing with engine speed, while in general an opposite criterium is applied.

All the efforts made to understand and model knock occurrence should be complemented by a better understanding of the interaction between the knocking combustion and the combustion chamber components, and I think that this activity gave important contribution in this direction.

### 1.11 References

- [1.1] G. Cantore, M. Giacomini, R. Rosi, A. Strozzi, P. Pelloni, C. Forte, M. Achilluzzi, G.M. Bianchi, L. Ceschini, A. Morri, "Validation of a Combined CFD/FEM Methodology for the Evaluation of Thermal Load Acting on Aluminum Alloy Pistons through Hardness Measurements in Internal Combustion Engines", *Metallurgical Science and Technology*, 2011.
- [1.2] M. Kubicki, H.C. Watson, J. Williams, P.C. Stryker, "Spatial and Temporal Temperature Distributions in a Spark Ignition Engine Piston at WOT". SAE Technical Paper Series, 2007.
- [1.3] Mahle GMBH, "Piston and engine testing", 2012.
- [1.4] F.S. Silva, "Fatigue on engine pistons - A compendium of case studies", *Eng. Fail. Anal.* Volume 13 (Issue 3) (April 2006), <http://dx.doi.org/10.1016/j.engfailanal.2004.12.023>.
- [1.5] F. Szymtka, M. Salem, F. Rézai-Aria, A. Oudin, "Thermal fatigue analysis of automotive Diesel piston: Experimental procedure and numerical protocol", *Int. J. Fatigue* 73 (2015), <http://dx.doi.org/10.1016/j.ijfatigue.2014.11.011>.
- [1.6] G. Floweday, S. Petrov, R.B. Tait, J. Press, "Thermo-mechanical fatigue damage and failure of modern high performance diesel pistons", *Eng. Fail. Anal.* 18 (2011), <http://dx.doi.org/10.1016/j.engfailanal.2011.02.002>.
- [1.7] M. Shariyat, S.J. Fathi, S.A. Jazayeri, "Experimentally validated combustion and piston fatigue life evaluation procedures for the bi-fuel engines, using an integral-type fatigue criterion", *Lat. Am. J. Solids Struct.* 13 (2016), <http://dx.doi.org/10.1590/1679-78251828>.
- [1.8] O.P. Singh, Y. Umbarkar, T. Sreenivasulu, E. Vetrivendan, M. Kannan, Y.R. Babu, "Piston seizure investigation: Experiments, modeling and future challenges", *Eng. Fail. Anal.* 28 (2013), <http://dx.doi.org/10.1016/j.engfailanal.2012.11.005>.
- [1.9] T.J. Kamps, J.C. Walker, R.J. Wood, P.M. Lee, A.G. Plint, "Reproducing automotive engine scuffing using a lubricated reciprocating contact", *Wear* (2015), <http://dx.doi.org/10.1016/j.wear.2014.12.045>.
- [1.10] S. Wan, D. Li, G. Zhang, A.K. Tieu, B. Zhang, "Comparison of the scuffing behaviour and wear resistance of candidate engineering coatings for automotive piston rings", *Tribol. Int.* (2017), <http://dx.doi.org/10.1016/j.triboint.2016.10.026>.
- [1.11] B. Zabala, A. Igartua, X. Fernandez, C. Priestner, H. Ofner, O. Knaus, M. Abramczuk, P. Tribotte, F. Girod, E. Roman, R. Nevshupa, "Friction and wear of a piston ring/cylinder liner at the top dead centre: experimental study and modelling", *Tribol. Int.* (2017), <http://dx.doi.org/10.1016/j.triboint.2016.10.005>.
- [1.12] J. Fitton, R. Nates, "Knock erosion in spark-ignition engines", SAE Tech. Pap. 11 (1996), <http://dx.doi.org/10.4271/962102>.
- [1.13] R.J. Nates, A.D.B. Yates, "Knock damage mechanisms in spark-ignition engines", SAE Int. (1994), <http://dx.doi.org/10.4271/942064>.
- [1.14] R.J. Nates, "Knock Damage in Spark-Ignition Engines", University of Cape Town, 1995.
- [1.15] J.C. Fitton, R.J. Nates, "Investigation into the relationship between knock intensity and piston seizure", *N&O J.* (1992) 2–7.



- [1.16] B. Waldhauer, U. Schilling, S. Schnaibel, J. Szopa, "Piston Damages - Recognising and Rectifying", MSI Motor Service International, 2004.
- [1.17] R.R. Maly, R. Klein, N. Peters, G. Konig, "Theoretical and Experimental Investigation of Knock Induced Surface Destruction". SAE Technical Paper 900025, 1990.
- [1.18] N. Cavina, N. Rojo, A. Businaro, L. Ceschini, E. Balducci, A. Cerofolini, "Analysis of pre-ignition combustions triggered by heavy knocking events in a turbocharged GDI engine", Energy Procedia 101 (2016) 893–900, <http://dx.doi.org/10.1016/j.egypro.2016.11.113>.
- [1.19] Z. Wang, H. Liu, T. Song, Y. Qi, X. He, S. Shuai, J. Wang, "Relationship between superknock and pre-ignition", Int. J. Engine Res. 16 (2015) 166–180, <http://dx.doi.org/10.1177/1468087414530388>.
- [1.20] R.J. Nates, "Thermal Stresses Induced by Knocking Combustion in Spark-Ignition Engines". SAE Technical paper 2000-01-1238, 2000, <http://dx.doi.org/10.4271/2000-01-1238>.
- [1.21] X. Zhen, Y. Wang, S. Xu, Y. Zhu, C. Tao, T. Xu, M. Song, "The engine knock analysis - an overview", Appl. Energy 92 (2012) 628–636, <http://dx.doi.org/10.1016/j.apenergy.2011.11.079>.
- [1.22] N. Cavina, E. Corti, G. Minelli, D. Moro, L. Solieri, "Knock indexes normalization methodologies", SAE Int. J. Engines (2006), <http://dx.doi.org/10.4271/2006-01-2998>.
- [1.23] L. Ceschini, A. Morri, E. Balducci, N. Cavina, N. Rojo, L. Calogero, L. Poggio, "Experimental observations of engine piston damage induced by knocking combustion", Mater. Des. 114 (2017) 312–325, <http://dx.doi.org/10.1016/j.matdes.2016.11.015>.
- [1.24] E. Balducci, L. Ceschini, N. Rojo, N. Cavina, R. Cevolani, M. Barichello, "Knock induced erosion on Al pistons: Examination of damage morphology and its causes", Engineering Failure Analysis, Volume 92, October 2018, Pages 12-31, <https://doi.org/10.1016/j.engfailanal.2018.05.002>
- [1.25] L. Ceschini, A. Morri, A. Morri, M. Di Sabatino, "Effect of thermal exposure on the residual hardness and tensile properties of the EN AW-2618A piston alloy", Mater. Sci. Eng. A. 639 (2015) 288–297. doi:10.1016/j.msea.2015.04.080.
- [1.26] E. Balducci, L. Ceschini, A. Morri, A. Morri, M. Di Sabatino, L. Arnberg, Y. Li, "High Temperature Behavior of the EN AW-2618A Piston Alloy Containing 0.12wt% Zr: Influence of Heat Treatment", in: Mater. Today Proc., Elsevier Ltd, 2015: pp. 5037–5044.
- [1.27] E. Balducci, L. Ceschini, S. Messieri, S. Wenner, R. Holmestad, "Thermal stability of the lightweight 2099 Al-Cu-Li alloy: Tensile tests and microstructural investigations after overaging", Mater. Des. 119 (2017) 54–64. doi:10.1016/j.matdes.2017.01.058.
- [1.28] F. Cesari, "Calcolo matriciale delle strutture 2", Pitagora Editrice Bologna, 1997.
- [1.29] F. Cesari, "Meccanica delle strutture. Metodo degli elementi finiti. 120 problemi risolti", Pitagora Editrice Bologna, 2011.
- [1.30] N. Cavina, N. Rojo, L. Ceschini, E. Balducci, L. Poggio, L. Calogero, R. Cevolani, "Investigation of Knock Damage Mechanisms on a GDI TC Engine", SAE Technical Paper 2017-24-0060, 2017, doi:10.4271/2017-24-0060.
- [1.31] J. Mutzke, B. Scott, R. Stone, J. Williams, "The Effect of Combustion Knock on the Instantaneous Heat Flux in Spark Ignition Engines", SAE Technical Paper 2016-01-0700, 2016, doi:10.4271/2016-01-0700.
- [1.32] S.P. Timoshenko, "Theory of Elasticity", McGraw-Hill, 3rd Ed., New York, 1970.



## 2 ION-based combustion control

The contents of this chapter, up to section 2.5, have been just submitted for publication to the SAE Journal of Engines, while the remaining contents, from section 2.6, have already been described in "Investigation on Pre-Ignition Combustion Events and Development of Diagnostic Solutions Based on Ion Current Signals" (SAE Int. J. Engines 10(4):1518-1523, 2017, ISSN 1946-3944, doi: 10.4271/2017-01-0784).

### 2.1 Introduction

Combustion feedback is essential in the latest-generation SI engines, to achieve both maximum performance, efficiency and reliability. Knock intensity estimation function has recently become a must for Engine Control Units (ECUs), since external disturbances can modify the engine knock tendency during on-board operation. The effects on the knock intensity of some of the engine boundary conditions can be mapped or modelled, and compensated by the open-loop spark advance controller, but the remaining uncertainties (fuel octane number, engine ageing...) cannot be fully included in the base spark advance calibration, but they are, at least partly, entrusted to the on-board knock measurement and control system. Several sensors can be installed on the production engine to estimate knock intensity, such as accelerometers, ion sensing, microphones, and of course in-cylinder pressure, which can be considered as a benchmark for other systems, characterized by higher cost and lower durability [2.1].

Knock intensity control can be insufficient to realize maximum efficiency operation, since in knock-free operation, where the knock control is supposed not to react and the spark advance control is purely in open-loop, external environmental disturbances like air humidity [2.2], engine ageing and cylinder-to-cylinder differences, which cannot be taken into account by the open-loop SA controller, can result in sub-optimal operation.

In knock-limited conditions, a protective controller (i.e. providing only negative corrections to the spark advance) is not pushing towards the maximum brake torque spark advance when operating with high octane fuel.

Conversely, an aggressive strategy (i.e. calculating and applying also positive corrections) would require, apart from great confidence on knock measurement that is however needed, some guarantee (feedback) that the controller is not over-advancing the spark angle, for the same uncertainties explained above relating spark advance to combustion phasing.

It is then clear that a feedback about the efficiency of each combustion event, in addition to its knock intensity, can be extremely useful and make the spark advance control potentially ideal. Moreover, the combustion control calibration effort could be reduced, since many of the corrections related to the accountable disturbances could be simplified or ignored, leaving them to the on-board closed-loop control. The well-known bell-shaped torque-CA50MFB (Crankshaft Angle at which 50% of Fuel Mass is burnt) characteristic, makes the CA50MFB, and equivalently the pressure peak position, reliable indicators of the distance from the maximum efficiency condition for the given operation [2.3]. Pressure signal is of course perfectly suited for this purpose, but such signal is very rarely used in production applications because of the high cost and low durability of the sensor [2.1].

Apart from in-cylinder pressure, there are two other signals that can be used to evaluate combustion phasing: ionization current and engine block vibrations. Ionization current sensing is a well-known technology that allows measuring a signal strictly related to free ions concentration, in-cylinder temperature and therefore the combustion process [2.4]. Substantially, it is a good surrogate of the pressure signal, even if with a lower SNR (i.e. Signal-to-Noise Ratio).

Accelerometers are used to measure engine block or cylinder head vibrations, which can be partly produced and transmitted to these sensors by the combustion process. This makes it possible to estimate knock intensity, since this kind of combustion is well characterised in the frequency domain; moreover, it

has been demonstrated how this signal can be processed to estimate pressure-peak position [2.5]. Anyway, the robustness of this last approach has to be further investigated and will not be considered in this work.

In this chapter, ionization current signal is processed to be used as input to a closed-loop combustion control strategy, as it contains all the required features listed above, and it can therefore provide the required information throughout the whole engine operating field.

The objective is to demonstrate the capability of the ionization current signal to be used as the main input to a closed-loop combustion controller, both in knock-free and knock-limited conditions.

Pressure signal is considered as a benchmark, to evaluate the ion-based control performance, and the control logic is the same for both controllers, to make them comparable.

First, the closed-loop combustion controller is developed and calibrated in a Model-in-the-Loop (MiL) environment, considering both pressure and ionization current signals. Then, the controller is implemented in a Rapid Control Prototyping (RCP) system and validated with the real engine. Experimental tests are then performed at the engine test bench, without further optimizing the controller calibrations, since the objective is mainly demonstrating the capabilities of the ionization current to replace the pressure signal to fully control the combustion process.

## 2.2 Ionization current signal

During the combustion, molecules get ionized by heat, making the charge conductive. By applying an electric field, it is possible to measure such conductivity and hence the ion concentration. The great advantage is that gasoline engines already have electrodes inside the combustion chamber, so no modification to the chamber is required. In production engines, the sensing system is generally integrated with the coil and it measures the current while applying a voltage difference between the two electrodes, immediately after the spark discharge event [2.2].

### 2.2.1 Ion sensing circuit

A schematic of the ion current sensing circuit is reported in Figure 2.1. On the left side, the arrows represent the current flow during the spark event, immediately after the IGBT opening. The inductive voltage generated in the secondary coil is used to generate the spark between the electrodes, but simultaneously it is used to charge the capacitor shown on the right.

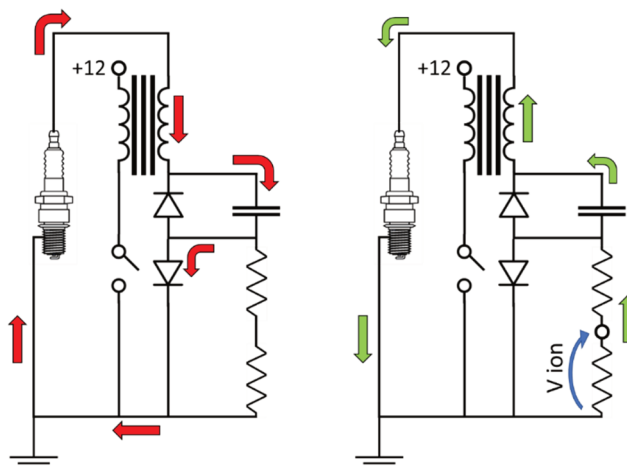


Figure 2.1 - Ion current sensing circuit

Once the spark ends (right side of the figure), the capacitor drives the ionization current through the secondary coil and the gap between the electrodes, with an intensity that is proportional to the gas conductivity and to the capacitor potential. The current intensity can be evaluated through the sensing resistance shown in the bottom right side of the schematic [2.6, 2.7].

### 2.2.2 Ionization

Ionization is caused by the heat released during the combustion process, through two different mechanisms. One takes place in the flame front, where the oxygen reacts with the carbon and the hydrogen, rapidly passing through several intermediate ionized stages [2.8], and finally producing water and CO<sub>2</sub>. Since the flame front is supposed to be thin and moving across the combustion chamber, ion generation is localized and can be sensed through the spark plug electrodes only during the early stage of the combustion. This mechanism is usually called “chemi-ionization” [2.8, 2.9], “chemical ionization” [2.4], “flame ionization” [2.10] or “flame front” [2.2] and it corresponds to the first peak on the ion signal, after the ignition, as it can be seen in Figure 2.2.

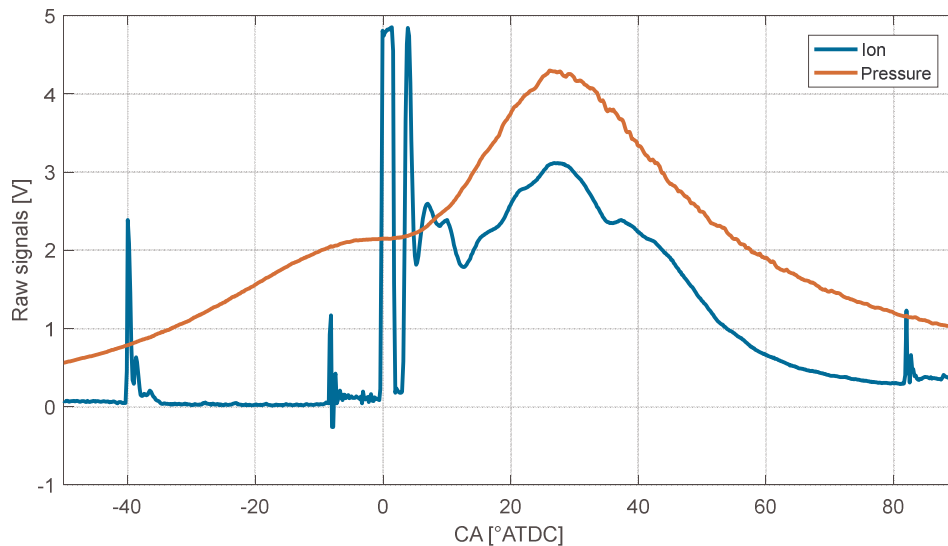


Figure 2.2 - in-cylinder pressure and ion current signals comparison

The second mechanism of ions formation is related to massive thermal dissociation, concerning the whole charge, which is promoted by high temperature and it corresponds to the second peak of the signal shown in Figure 2.2. Temperature, pressure and volume are closely related (e. g. the ideal gas law can be applied), so that a strong correlation is expected between Pressure Peak Position (PPP) and ion current thermal peak position [2.2, 2.3]. The angle corresponding to in-cylinder peak temperature, to which it should correspond the maximum ion concentration, is expected between the TDC and the peak pressure angle; but the sensing dynamics, the local temperature measurement, and probably other aspects very complex to consider, result experimentally in a “thermal” or “post-flame” ionization peak extremely close to the peak pressure angle.

Figure 2.2 shows how reliably the thermal peak can be used to estimate the pressure peak angle, and this is generally true for all engine operating conditions. This is the feature of the ion signal that will be considered in this work as an indicator of the combustion phasing, to be used as input to the SA closed-loop controller.

### 2.2.3 Knock

Ion signal can be used to detect knock too, as widely described in literature [2.4, 2.6, 2.11, 2.12]. The high frequency pressure oscillations induced by knocking combustion are reflected on in-cylinder temperature and therefore on ion concentration, causing a corresponding oscillation of the ion current signal, as can be seen in Figure 2.3. As for the pressure signal, oscillations are to be found during the expansion stroke, generally from the peak pressure position onwards, and their spectrum is related to the chamber resonance frequency range. The analogy between the two signals allows adopting similar algorithms, which are mainly based on high-pass filtering and windowing stages.

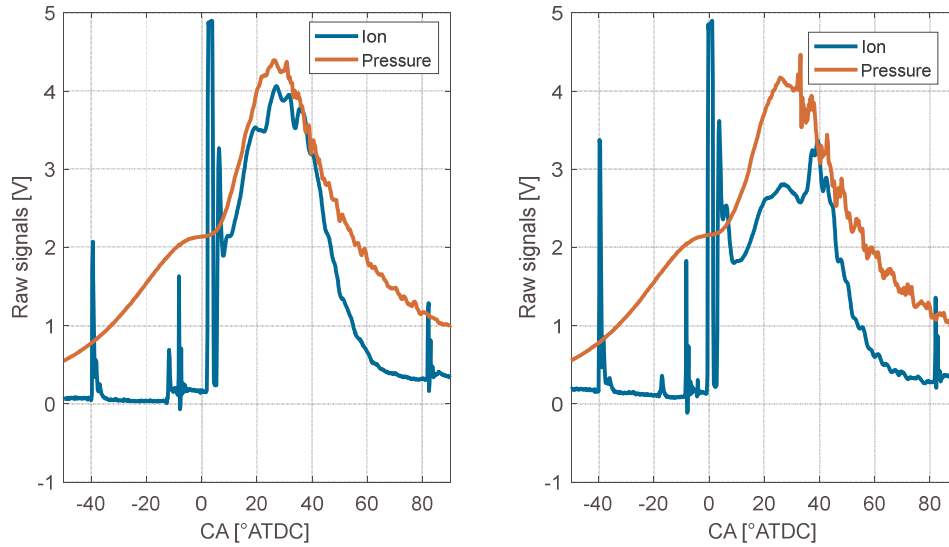


Figure 2.3 - Pressure and ion signals comparison during knocking combustions

#### 2.2.4 Other Ion Signal Features

Ion current signal can be effectively used to detect misfire, since in absence of combustion the signal is null [2.13, 2.14]. The same signal can also be used to detect preignition, since an early heat release results in a flame-ionization before the spark [2.15]. Further, some attempts have been made to estimate in-cylinder air-to-fuel ratio from the current signal [2.16], since the thermal ionization peak amplitude shows a non-linear correlation with this parameter.

There are other characteristics of the signal, in the earlier angles displayed in Figures 2.2 and 2.3, which can vary depending on the ignition and sensing circuit. They are shortly described here for sake of clarity. In general, the ion current signal is available during the whole engine cycle, unless being biased by the ignition process. The first spike, during the compression stroke, is given by the start of the coil energizing phase, and the second spike corresponds to the spark discharge angle (the angular distance between such spikes is the dwell angle, see Figure 2.2). The interval between the spark discharge and the first rising edge is the spark duration, during which the current flows through the diode shown in Figure 2.1 in parallel to the voltage divider. As the spark ends, the remaining energy in the coil is responsible for the oscillating response that can be seen before the chemical phase.

### 2.3 Experimental setup

The experimental tests have been conducted on a V-8 3.8 litres GDI turbocharged high-performance engine (Table 2.1), equipped with ion sensing technology as standard production equipment. Several ion-based strategies are implemented on the production engine (misfire diagnosis, knock and preignition detection), but not the combustion phasing closed-loop control.

In the test bench set-up, pressure and ion signals of every cylinder have been acquired and sampled at 200 kHz.

Table 2.1 – Engine specifications

Stroke	82 mm
Bore	86.5 mm
Compression Ratio	9.4:1
Displacement	3855 cc, 8 cylinders

In the first stage, both pressure and ion signals have been recorded during steady-state spark sweeps, to generate the database required by MiL activity (described below). 4500 rpm and high load is the operating condition chosen for this phase of the project.

In the production layout, the ECU is receiving via CAN the ion-based indexes and the corresponding SA corrections calculated by the dedicated module. For the real-time implementation, the ion module has been replaced by a rapid control prototype, so that the protective knock-based corrections calculated by the ion module are ignored and replaced by the strategy implemented in the RCP. At the same time, the RCP is connected via CAN to the test bench combustion analyser, which provides standard pressure-based indexes (CA50MFB and knock intensity, the latter measured via MAPO – Maximum Amplitude Pressure Oscillation [2.17]) and customized ion-based indexes (ATHp and IntIon) to feed the control strategy.

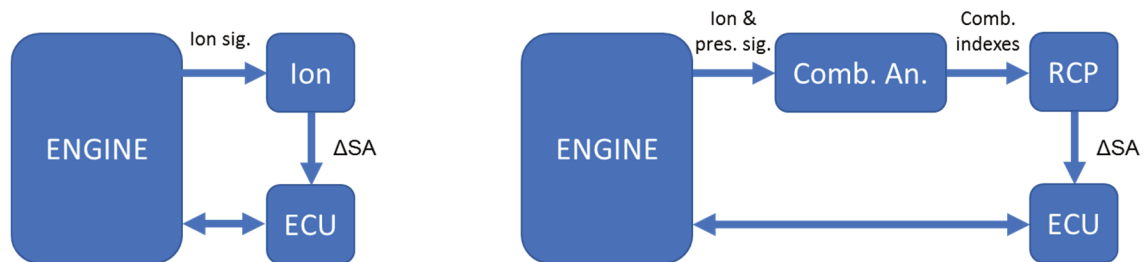


Figure 2.4 - Left: on-board, standard equipment layout; right: test-bench layout

## 2.4 Spark Advance Controller Development

The controller task is to manage each cylinder spark advance to achieve a pre-defined combustion phase, while guaranteeing that a pre-fixed knocking intensity level is not largely nor frequently overcome. The possible outcome, in terms of engine performance and costs optimization, is remarkable: combustion efficiency could in fact be optimized under all engine operating conditions, cylinder by cylinder, without requiring significant calibration efforts, and in a fully auto-adaptive way. Such results have a very strong impact on the overall engine development process, and on the performance the engine can guarantee during its entire life:

- Combustion efficiency optimization is achieved by controlling the combustion phasing, considering the well-known bell-shaped Brake Specific Fuel Consumption (BSFC) vs CA50MFB curves [2.3]. Closed-loop control can therefore be implemented by setting as target the optimal CA50MFB value, previously identified as a function of speed and load. Then, information about combustion phasing (i.e., CA50MFB) is extracted from the in-cylinder pressure signal, by evaluating the so-called normalized heat release curve [2.3].
- During combustion phasing optimization activity, the controller varies the SA angle to reach the target value, and its authority should be limited to avoid excessive knocking levels. In-cylinder pressure signal should then be real-time processed to provide both combustion phase and knocking intensity information. The pressure-based index used in this work is called MAPO [2.17]. It represents the maximum of the absolute value of the high-pass filtered in-cylinder pressure signal (a 5 kHz high-pass filter has been used). Knocking is a stochastic event [2.18], and very high percentile MAPO values, around 98-99%, are normally used to determine the knocking intensity of a sequence of combustion events, each characterized by its MAPO value, once they have been collected in a First In First Out buffer.
- With the proposed control system, the optimization mentioned above could be performed cylinder by cylinder: even the ideal open-loop controller, "perfectly" calibrated, would inevitably achieve an overall higher fuel consumption.

- One of the most interesting outcomes of the proposed solution is the great reduction of calibration costs and time. The SA open-loop controller could be fully eliminated, together with the associated calibration time and costs.
- Finally, the closed-loop controller is inherently auto-adaptive, both to engine-to-engine variations and to combustion variations during engine life (fuel quality, ambient conditions, ageing effects).

#### 2.4.1 In-Cylinder Pressure Controller Layout

The controller structure was developed by considering different sub-functions: targets definition, closed-loop controllers, hierarchy definition, SA actuation. As shown in Figure 2.5, the controller compares the target CA50MFB and the maximum admissible MAPO 99th percentile with the measured ones, and two parallel error calculations are performed. The CA50MFB controller filters the measured values through a moving average (to avoid reacting to intrinsic combustion variability) and it is bidirectional, in the sense that it can request both negative and positive corrections to reach the target value. The knock control strategy, instead, can only require negative SA corrections, if the knocking level is higher than the threshold. In that case, the CA50MFB error is frozen, and the knock controller error prevails. In this way, the SA actuation variations requested by the combustion phase controller are executed only if the knocking level is below the actual threshold, while the knock controller applies SA reductions if such threshold is overcome. The errors of the two strategies, w.r.t. their targets, are summed and the resulting error is considered to feed the PI controller. Weights are available to allow the controller to react differently to the two errors. In addition, a "fast" protective action, highlighted in blue, performs a permanent correction to the integral value of the PI every time a heavy knock cycle is detected.

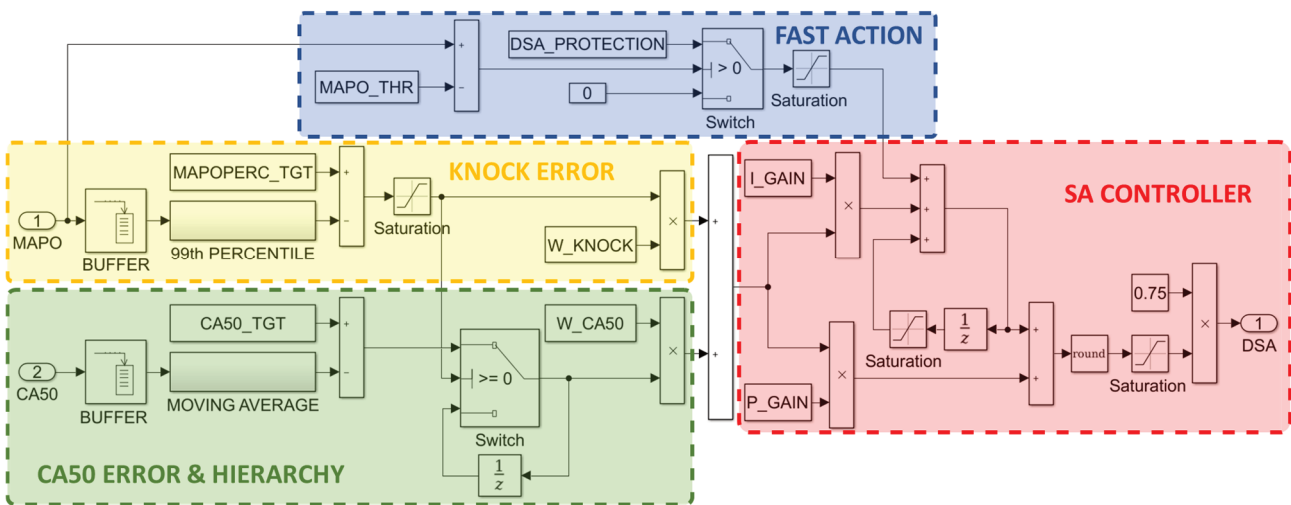


Figure 2.5 - Pressure-based Closed-loop Controller Layout

##### 2.4.1.1 Pressure-based Model In the Loop (MIL) Results

The controller was then tested, further developed and optimized in a self-built Model In the Loop environment. The engine model, and the associated combustion variability, was reproduced by randomly selecting in-cylinder pressure cycles from pre-recorded engine running conditions (described in chapter 3), cylinder-by-cylinder, and for the specific SA value that the controller would output, as was done in previous works [2.19]. In particular, for the investigated operating point, 500 cycles have been acquired for 15 consecutive values of SA, corresponding both to excessive knock intensity and sub-optimal knock-free operation.

The engine model (database) is then made by two 3-D matrices, one for the CA50MFB and one for the MAPO values. The applied SA (calculated by the controller), the random number generated every iteration, needed to randomly select a cycle, and the cylinder number, define the cell of the matrices to be selected. Considering cylinder n. 1, Figure 2.6 shows a steady-state test where the combustion phasing controller is

activated starting from an open-loop condition, while the engine is running at 4500 rpm and 23 bar of IMEP (Indicated Mean Effective Pressure). In the higher part of the top plot, the dashed line represents the CA50MFB target value and instantaneous and averaged CA50MFB values are also shown. The moving average value, represented by the thick solid line, is the input to the controller. The lower part of the upper plot shows the SA correction applied by the controller w.r.t. the open-loop value. The lower plot shows instantaneous MAPO values and the its 99th percentile. The dashed line is the MAPO 99th percentile threshold.

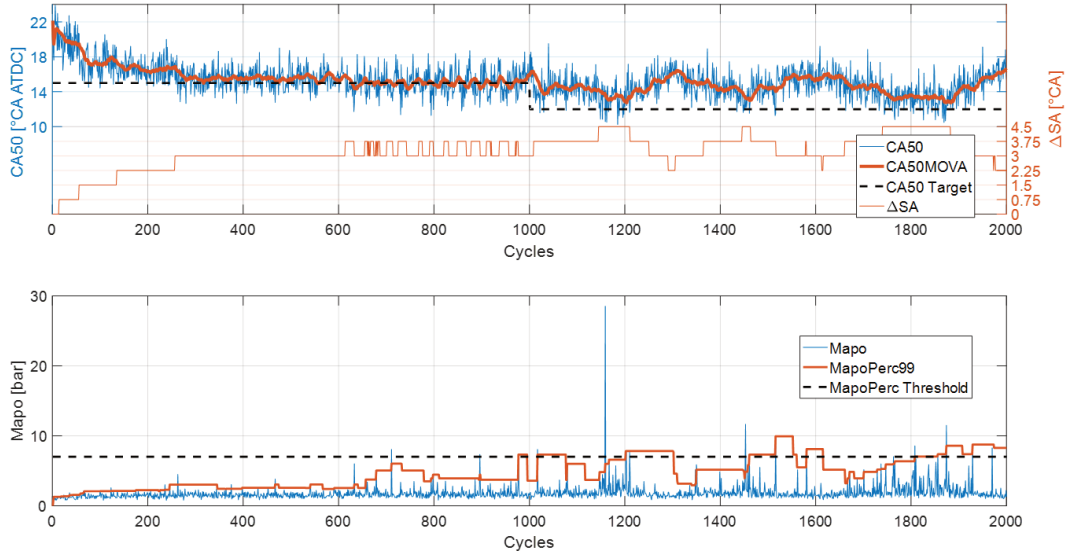


Figure 2.6 - Pressure-based Virtual Controller Performance (Knock-limited Operation)

Finally, the x-axis represents elapsed engine cycles in both plots. In the first part of the test, the controller target is set to 15 degrees ATDC, corresponding to a light knock condition: the target is reached with a 3.5 degrees SA correction (limiting the SA oscillation to one step once it has been reached), and the MAPO 99th percentile is still under the threshold, even if it has significantly increased. The CA50MFB target is then reduced to 12 degrees ATDC at cycle n. 1000. The controller reacts by further advancing SA, thus further increasing knock intensity. Once the knock threshold has been overcome (cycle n. 1200), the SA is reduced by the protective action of the knock controller, and from then on, both controllers cooperate to keep the CA50MFB as close as possible to the target, while limiting the 99th MAPO percentile below the threshold.

## 2.4.2 Ion Current Controller Development

The basis on which this work is founded is that ion current system may not only replace accelerometer-based knock controllers, but it could allow a closed-loop SA control able to maximize engine efficiency also under knock-free operating conditions. In fact, both CA50MFB- and MAPO-related information can be extracted from the ion current signal.

### 2.4.2.1 Ion indexes calculation

In this initial phase, ion-based indexes have a relatively simple definition, also to be compatible with real-time calculation limitations.

The knock index, called  $IntIon$ , is calculated as follows: the signal is high-pass filtered, then the mean value of its absolute value is evaluated within a predefined angular window.

$$IntIon = \frac{\sum_{win\_start}^{win\_end} |ION_{high-pass}|}{samples} \quad (2.1)$$



In particular, the cut-off frequency of the filter has been set to 15 kHz, and the signal has been windowed between 25 and 55 °CA ATDC.

The angle corresponding to the thermal peak of the ion signal has been calculated by identifying the up-down zero-crossing of the first derivative of the low-pass filtered ion signal (cut-off frequency set at 2 kHz), windowed in the range 15-70 °CA ATDC.

Figure 2.7 shows on the left side the correlation between CA50MFB and ATHP (Angular THERmal Peak position), which is significantly high (87%), and almost linear. The right side of Figure 2.7 shows the correlation between MAPO and Intlon ion-based knocking index, for the considered engine operating condition (4500 rpm and 23 bar of IMEP). In this case, the correlation level is lower (62%), but still sufficient to correctly close the control loop.

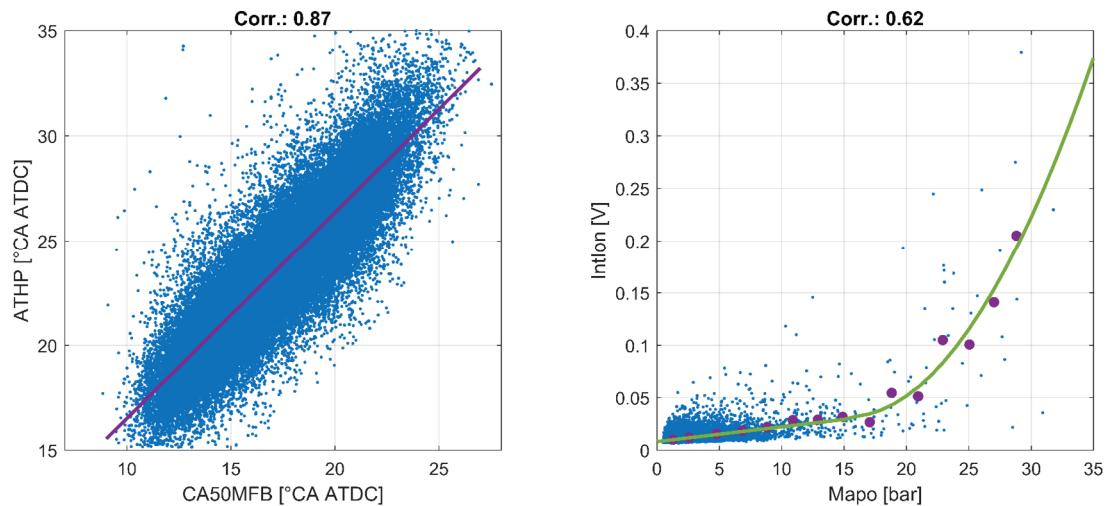


Figure 2.7 - Correlation Diagrams between In-cylinder Pressure and Ion Current: Combustion Phase (left) and Knock Intensity (right)

For a better assessment of the ion signal potential, the controller was purposely kept identical to the pressure-based one, and its inputs are previously converted from ion-based to pressure-based ones. In other words, a "conversion" stage is added to the controller shown in Figure 2.5, to convert ATHP into CA50MFB, and Intlon into MAPO. Such conversion has been performed by inverting the fitting functions reported in Figure 2.7, to calculate the corresponding values of CA50MFB and MAPO as a function of ATHP and Intlon, respectively.

#### 2.4.2.2 Ion-based Model In the Loop (MIL) Results

A database similar to the one used for developing the pressure-based controller has been generated from the same experimental dataset for ATHP and Intlon indexes development, and the same type of tests have been performed.

Figure 2.8 shows an example of how the ion-current based virtual controller behaves during a test like the one shown in Figure 2.6. Also in this case, the phase target is decreased from 22 to 19 ATHP degrees (i.e., from 15 to 12 CA50MFB degrees) at cycle n. 1000, and the further SA increase applied to achieve such target induces excessive knocking levels. The intervention of the knock controller enables a condition where the SA is forced to oscillate to keep the engine as close as possible to the target combustion phase, avoiding excessive knock.

As it can be observed, the ion-based controller performance is very similar to the pressure-based one. To quantify and compare their behaviour, standard deviation and average error have been considered as possible metrics. Generally, under knock-free conditions, the two controllers achieve the same particularly high accuracy in terms of CA50MFB and ATHP (mean error equal to 0.02-0.03 CA degrees), and the combustion stability once the loop is closed is almost unaffected (standard deviation of about 1 degree CA in both cases). Under knock-limited operation, the pressure-based system allows reaching the threshold level very accurately, while the ion-based one is slightly less robust, due to greater false positives occurrence.



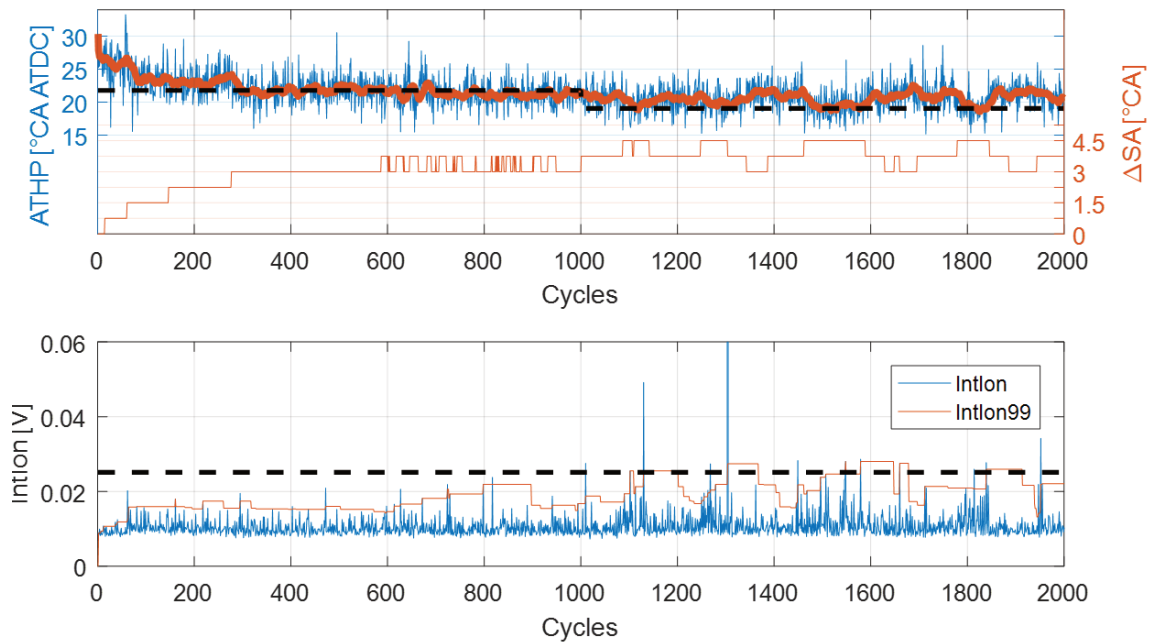


Figure 2.8 - Ion-based Virtual Controller Performance (Knock-limited Operation)

## 2.5 Experimental Validation

The final step of this phase of the project consisted in testing the developed controllers in real time, on the real engine. A self-developed, National Instruments based, Rapid Control Prototyping (RCP) system was used to verify the controller performance in the test cell. As described in Fig. 4, the RCP system receives, in real time from the combustion analysis system, pressure or ion current based indexes (combustion phase and knock intensity), and it applies a SA correction to the one calculated by the ECU in open loop. The following analysis is extended to all the engine cylinders, to demonstrate the ability of the controller to reach the same CA50MFB target (or the same knocking limit) by acting individually, and differently, on the SA angles of the various cylinders. For clarity, the results shown in the paper are limited to one of the two banks of the V-8 engine described above.

### 5.1 In-cylinder Pressure Controller Experimental Results

As an example of the in-cylinder pressure-based controller performance under knock-free operation, Figure 2.9 shows an experimental test during which a SA step was externally imposed, to analyse the controller ability to reject external disturbances.

In the first part of the test, up to engine cycle n. 1300, the controller is operating under steady-state conditions, with a CA50MFB target of 20 CA degrees ATDC. The top plot shows both the target and the achieved CA50MFB for the four cylinders (evaluated as a moving average - MOVA - of the instantaneous CA50MFB, and corresponding to the controller input), while the lower plot reports the individual, and different, DSA corrections applied to the cylinders (between -3.0 and -1.5 CA degrees). As it can be seen, the 4 considered cylinders require slightly different mean SA values to reach the target combustion phase. At cycle n. 1300, an external, 1.5 CA degrees wide, SA step disturbance is imposed to all the cylinders, as shown in Figure 2.9. The controller reacts by increasing the negative SA correction on all engine cylinders, and once the transient is over (in about 100-150 engine cycles), the CA50MFB target is reached again for all the cylinders. As it can be seen, the controller performance is very similar to the one observed in the virtual environment, confirming the high accuracy in terms of CA50MFB. Also in this case, the combustion stability is essentially unaffected w.r.t. open loop, constant SA operation.

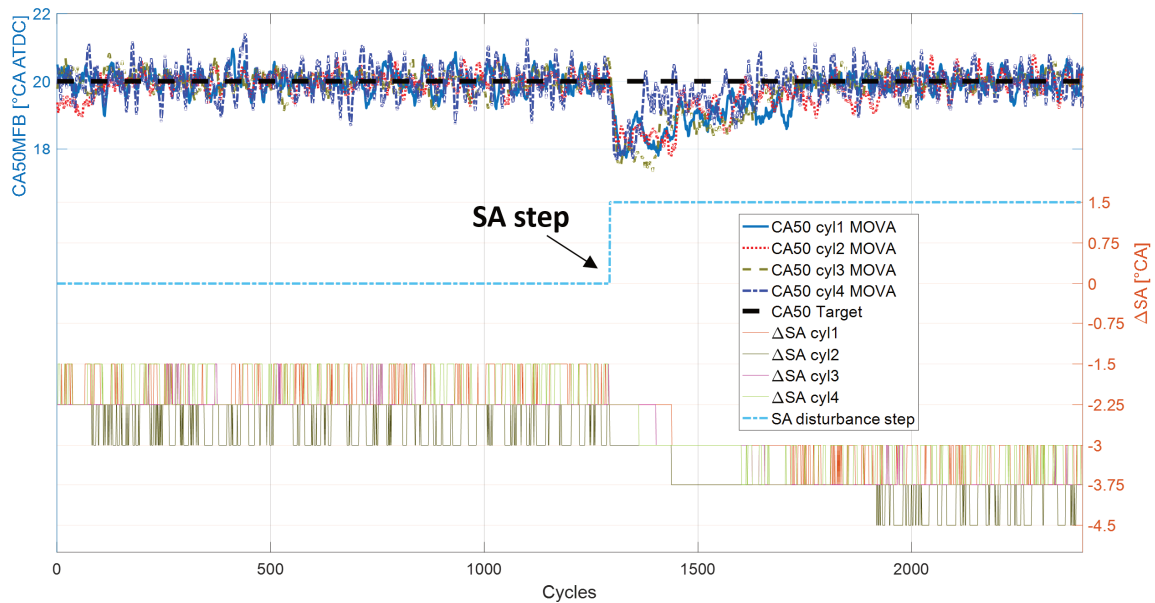


Figure 2.9 - Pressure-based Controller Performance (Knock-free Operation)

The performance of the in-cylinder pressure closed loop SA controller under knock-limited operation may be analysed by looking at Figure 2.10. For sake of clarity only cylinder 1 is investigated. Also in this case, the figure shows both the ability of the controller to guarantee that the threshold knocking level is not overcome under steady-state conditions, and its robustness in terms of disturbance rejection. The test is performed by setting a CA50MFB target equal to 12 CA degrees ATDC, which corresponds, for the given engine operating conditions, to excessive knocking intensity. Then a positive SA disturbance step is externally applied, to abruptly increase the knocking level, and to verify the controller ability to reduce the SA to continue respecting the threshold knocking level. The top plot shows the instantaneous MAPO values (thin line), the corresponding MAPO 99th percentile (thick line), and the MAPO 99th percentile threshold (thick dashed line).

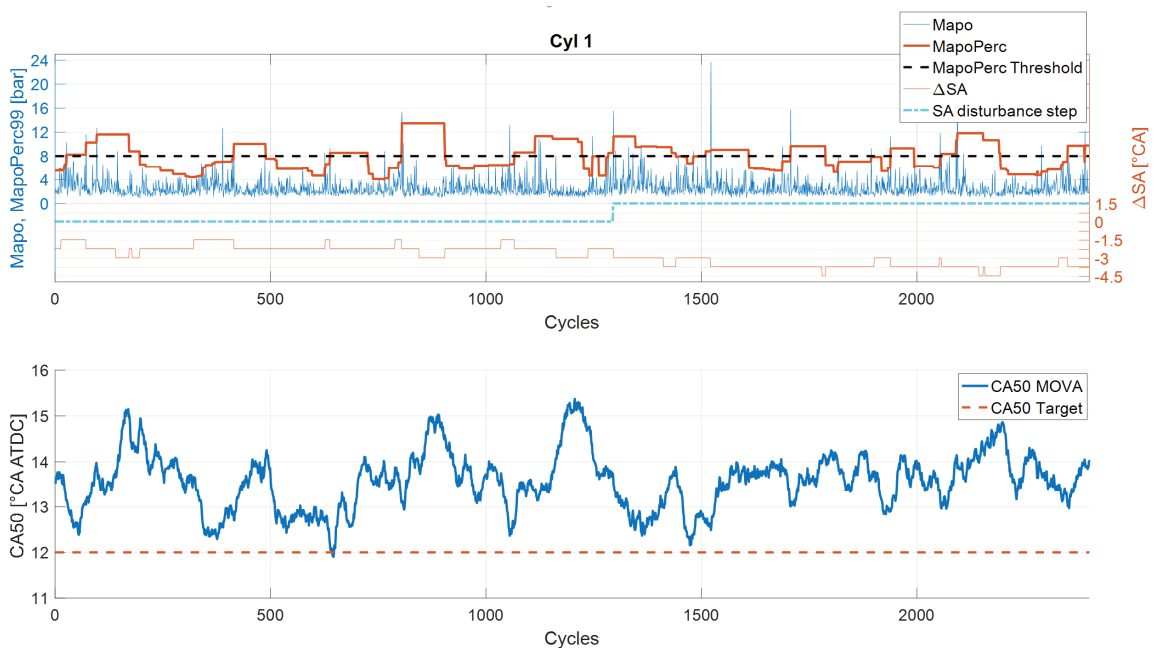


Figure 2.10 - Pressure-based Controller Performance (Knock-limited Operation)

The lower part of the top plot presents both the externally applied SA advance step (thick dashed line), and the SA correction imposed by the closed-loop controller. Finally, the bottom plot shows the CA50MFB

moving average value, or MOVA, for cylinder n.1, which is an input to the controller, and the CA50MFB target (equal to 12 CA degrees).

In the first part of the test, up to cycle n. 1300, it can clearly be observed how the controller continuously tries to reach the target CA50MFB by reducing the SA correction, but then the SA is forced back to smaller values (i.e., the SA correction assumes again greater negative values) since the MAPO percentile overcomes the threshold. Also, when the SA disturbance is applied, the controller reacts by requesting greater negative SA corrections, to limit the knocking intensity by compensating for the disturbance. At the end of the test the controller correction is in fact equal to around -3 CA degrees, 1.5 CA degrees smaller than at the beginning of the test.

### 2.5.2 Ion Current Controller Experimental Results

Finally, several experimental tests were conducted to evaluate the controller performance based on ion current rather than in-cylinder pressure measurements. Figure 2.11 reports an exemplary behaviour of the controller operating under knock-limited operation, focusing the attention on cylinder n. 2. The CA50MFB target has been set at 12 CA degrees ATDC, a combustion phase that corresponds to excessive knock intensity. The top plot shows, in the upper part, the controller internal variables, such as the ion current based knock index (IntIon), the 99th percentile value of the same index (IntIonPerc), and the threshold corresponding to maximum knocking intensity (IntIonThr). The lower part of the upper plot shows SA variations, both internally calculated by the controller (DSA), and externally imposed (SA disturbance step). The lower plot shows the controller performance, both in terms of CA50MFB moving average (CA50MOVA), and MAPO (MAPO, MAPOPerc), with respect to the corresponding target (CA50 Target) and threshold (MapoPerc target).

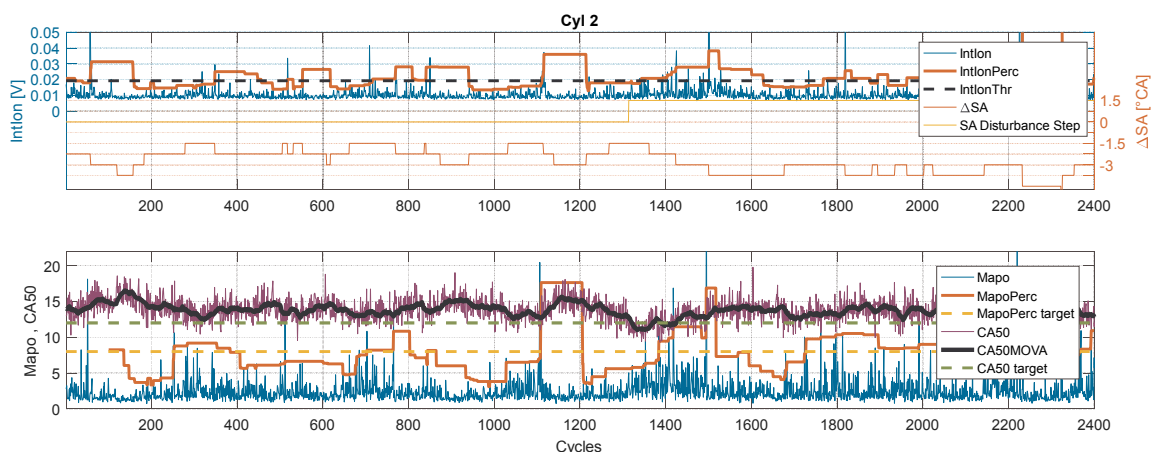


Figure 2.11 - Ion-based Controller Performance (Knock-limited Operation)

It can be clearly noticed how also in this case the maximum knock intensity is not frequently overcome, and at the same time the CA50MFB target is constantly tracked by reducing the SA correction. When the disturbance step is imposed (around cycle n. 1300), the knocking intensity increases, and the controller reacts by further reducing the SA, thus restoring a borderline knock condition, as desired.

### 2.5.3 Comparison between Pressure- and Ion-based Control

To numerically compare the two controls, mean values and standard deviations of the controlled variables have been considered, to evaluate accuracy and precision, respectively.

In Table 2.2, the comparison between the pressure-based and the ion current-based control performance is reported. In the upper part of the table, knock-free condition is considered, with two different target values of CA50MFB. The open loop condition is realized with a constant spark advance angle that realizes the CA50MFB closest to the target, identified for the specific engine and operating condition before the test. This condition is needed to set an “ideal” reference value for the standard deviation of CA50MFB.

The closed loop control, both implemented with pressure and with ionization current signals, maintains the target with good accuracy and with a small increase on CA50MFB variability (i.e. standard deviation).

Table 2.2 - comparison between pressure-based and ion current based control.

			CA50MFB Mean	CA50MFB Std
Knock-free	Control			
	Open Loop	-	20.42	1.41
	Pressure	MFB50 target: 20	20.00	1.48
	ION	(knock target 8)	19.42	1.48
	Open Loop	-	15.56	1.22
	Pressure	MFB50 target: 15	15.02	1.39
	ION	(knock target: 8)	15.03	1.39

			MapoPerc Mean	MapoPerc Std	MapoPercEQ Mean
Knock-limited	Pressure	Knock target: 4	5.21	1.64	-
	ION	(MFB50 target: 12)	3.93	1.52	5.72
	Pressure	Knock target: 8	8.75	3.04	-
	ION	(MFB50 target: 12)	6.83	2.60	9.48

The error between the target of 20°C CA MFB50 and the mean value realized with the ionization current-based control (19.41°C CA) is to be attributable to the identified MFB50 regression model (see Figure 2.7, left plot), which is assumed to be linear, while a higher polynomial degree would produce smaller regression errors.

In knock-limited operation, the performance of the controller is evaluated in terms of mean value (and secondly standard deviation) of the MAPO 99th percentile, which is the targeted variable. Because of the stochastic nature of the knock phenomenon, it is impossible to control a quasi-static value of the knock intensity (i.e. MAPO 99th percentile). Moreover, the controller architecture needs the threshold to be crossed in both directions, and since the positive distance (with respect to the threshold) is generally higher than the negative one, the mean knock intensity is slightly higher than the targeted value. That is the reason why the pressure-based mean-controlled knock intensity is higher than the target (5.2 bar instead of 4 bar, 8.75 bar instead of 8 bar).

The same applies to the ionization current-based controller if the variable MapoPercEQ is considered. As explained before, the two control architectures are the same, but in the ion-based version an ion-to-pressure indexes conversion has been introduced upstream of the controller. Therefore, the ion-based control is running on the equivalent pressure indexes. When controlling knock intensity with ionization current signal, the equivalent pressure knock index values (MapoPercEQ) and the measured pressure knock index values (MapoPerc) should match on average, unless a regression error is committed, or the regression model is not sufficiently robust. The lower standard deviation obtained for the knock intensity is related to the lower mean value of the index itself.

## 2.6 Pre-Ignition detection

Pre-ignition combustion is extremely dangerous for the engine, as it induces high pressure levels and usually heavy knocking events. The excessive pressure can damage the connecting rod, while the increased heat transfer to the chamber walls may lead to seizure [2.20]. The possibility of diagnosing pre-ignition can be fundamental in achieving higher efficiency or specific power, while safeguarding the engine. Once one or more pre-ignition cycles are detected, the Engine Control Unit has many ways to react (for example it can reduce the load, it can cut injection to one or more cylinders, it can vary the intake and exhaust valves overlap). Since there is no unequivocal definition of pre-ignition, a clarification is necessary: in this document, pre-ignition is a combustion process that started before (and so not initiated by) the spark, independently of the combustion initiation cause. Such early combustion can be triggered by a hot-spot in the combustion chamber [2.3], by the compression ignition by oil contamination, or by glowing carbon deposits. The first mode is often called “surface ignition”, while the two other modes are the most likely causes of the LSPI (Low Speed Pre-Ignition) [2.21, 2.22].

In this chapter, ionization current signal has been used to diagnose pre-ignition cycles, which were observed during some tests. Two different pre-ignition modes have been identified: test 1 involves clearly surface ignition most likely initiated by the spark plug ceramic insulator, which degenerates in a run-away condition; test 2, instead, describes isolated pre-ignition cycles, for which the initiation cause is difficult to assess.

### 2.6.1 Test 1

Test 1 was conducted at 4500 rpm at full load. Heavy knocking condition was induced in cylinders 1, 2 and 3 by controlling the Spark Advance (SA). After 50-80 cycles (depending on the cylinder) some pre-ignition cycles occurred, alternating with normally ignited cycles. Then all cycles pre-ignited, in a self-sustaining mechanism that rapidly forced the start of combustion to migrate towards the early compression phase. Figure 2.12 shows the time history of the crank angle value corresponding to 10% of mass fraction burned (CA10%MFB), which rapidly diminishes (symptom of more and more advanced, or early, start of combustion) when the combustion mode enters the pre-ignition region.

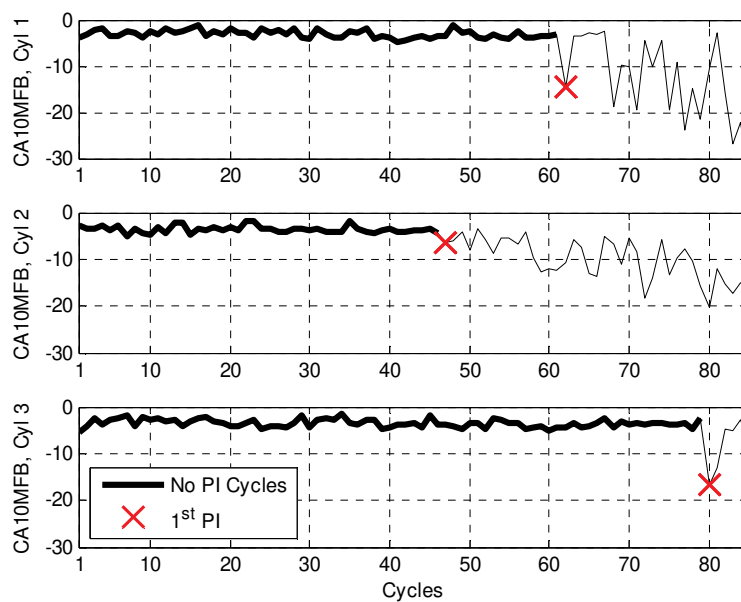


Figure 2.12 - Sequences of CA10%MFB in Test 1 for cylinders 1, 2 and 3 and first pre-ignition occurrence.

In a previous work [2.20], the pre-ignition sequence and the effects on the combustion chamber components have been thoroughly described. In Figure 2.13, ion current and pressure signals for some pre-ignition cycles are represented. Pressure traces, on the right, show cycles with different combustion phase and correspondingly increasing peak pressure, but above all, it is clear that these combustions started before the spark (SA). On the left, ion current signals of the same cycles are represented. Compared to the signal of Figure 2.2, all these cycles are characterized by a rising edge during dwell time, which indicates the presence of combustion.

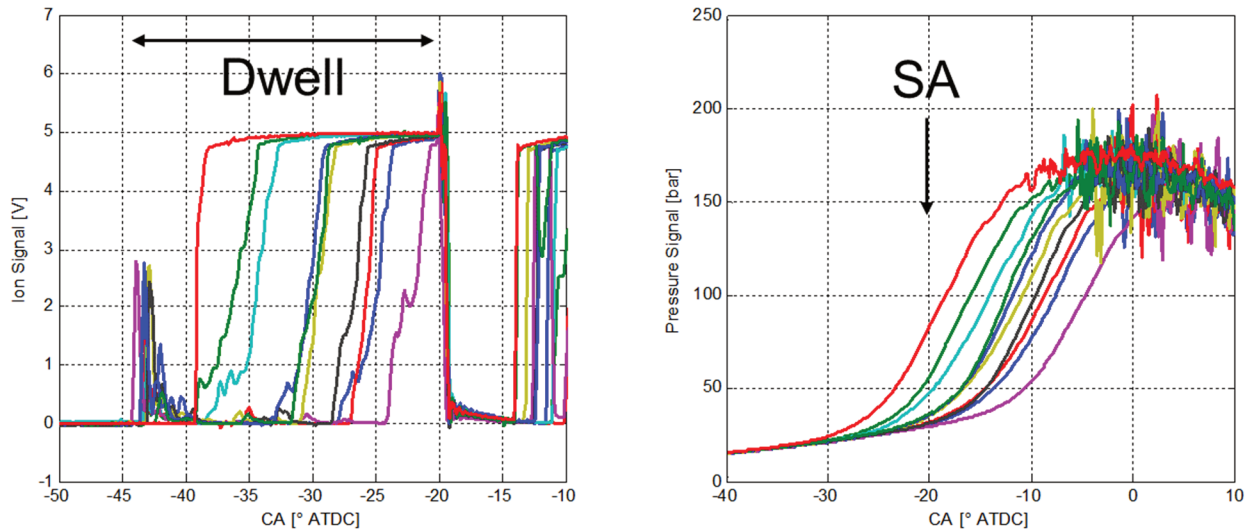


Figure 2.13 - Some pre-ignition cycles in Test 1: Ion signals (left) and corresponding pressure signals (right).

### 2.6.2 Dwell integral index

To identify pre-ignition cycles, a simple index can be defined. For example, the integral (or the mean value) of the signal during dwell time can be calculated for every cycle of every cylinder. Then, index values above a certain threshold will categorize the relative cycle as pre-ignited. In doing this, the only information needed is Spark Advance angle and (an estimate of) the dwell start time (or angular position). This kind of operation can be simply implemented into the ECU, which exactly knows such information. Figure 2.14 shows an example of a cycle that would have a non-zero pre-ignition index. The spike in the signal at around -30 CA, whose position may vary within the dwell interval, is not to be considered a symptom of pre-ignition but noise, as there is no correlation between its occurrence and corresponding combustion angles.

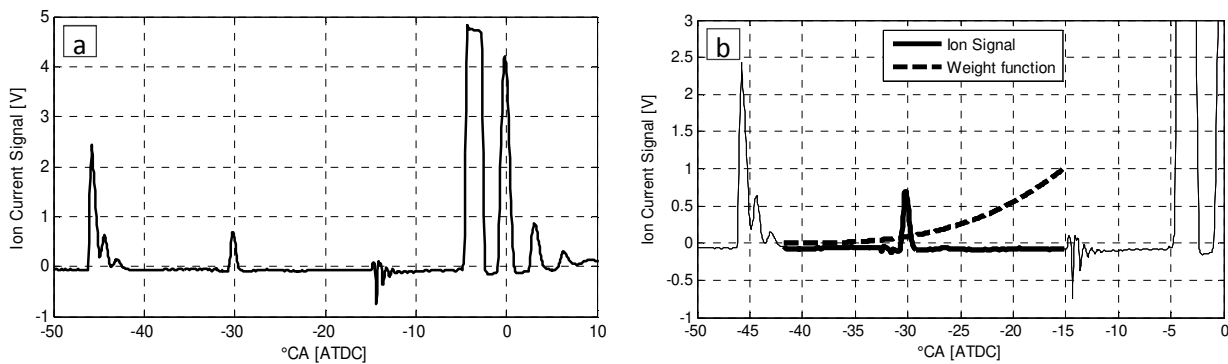


Figure 2.14. Disturbed ion signal during dwell time (a); Considered portion of the signal for Dwell Integral calculation and weight function (b).

To be immune (or more robust) to the spike presence and to extend sensitivity for pre-ignition cycles whose raising edge in the ion current signal is very close to the spark, the Dwell Integral (pre-ignition index) has been defined introducing a weight function  $W_i$  that gives more relevance to the samples close to the ignition, defined by Equation (2.2):

$$W_i = \left(\frac{i}{N}\right)^3 \text{ for } i = 1, \dots, N \quad (2.2)$$



where  $i$  is the generic sample of the considered window and  $N$  is the number of samples of the considered window. The Dwell Integral is defined by Equation (2.3):

$$DI = \frac{\sum_{i=1}^N W_i S_i}{N} \quad (2.3)$$

where  $S_i$  is the ion signal value at the sample  $i$ .

Of course, a more robust algorithm can be defined, for example, by replacing the weight function  $W_i$  with a spike detection algorithm that simply detects the falling edge (not present in pre-ignition events) after the raising edge.

As the Spark Advance was kept constant during the tests, a Probability Density Function (PDF) of the CA10%MFB (Crankshaft Angle corresponding to the 10% of mass of fuel burned) can be calculated for the cycles until the first pre-ignition occurs, for every cylinder. Strictly speaking, it is not possible to identify with great confidence the first pre-ignition cycle by the CA10%MFB value or by its sudden variation (for example, cylinder 2 has a gradual transition). In [2.23] a more rigorous statistical approach to identify pre-ignition events is proposed. However, it may be possible to isolate consecutive cycles that are reasonably not pre-ignited. In Figure 2.12, the thick line corresponds to the considered cycles and the red cross indicates the first suspected pre-ignition.

The three distributions of the three cylinders (assumed to be normal distributions), or the mean distribution (as they are very similar) estimated by considering only non-pre-ignited cycles, can characterize “standard” combustion at this operating point for the given Spark Advance angle. Table 2.3 presents the numerical values that characterize non-pre-ignited CA10%MFB distributions for the specific operating condition. Values of CA10%MFB that fall far from the mean value, can be considered anomalous combustions: a (considerably) lower value is symptom of pre-ignition, while a (considerably) higher value is evidence of a very slow combustion or a misfire. This consideration can be extended to other combustion angles (e.g. CA50%MFB). However, for this work purpose, lower mass fraction burned angles should present greater sensitivity, and only the left side of the distribution is of interest.

Table 2.3. CA10%MFB probability density function parameters ( $\mu$ ,  $\sigma$ ) and pre-ignition threshold ( $\mu - 6 \sigma$ ), for cylinders 1, 2, and 3.

Cyl	$\mu$ [°CA ATDC]	$\sigma$ [°CA ATDC]	$\mu - 6 \sigma$ [°CA ATDC]
1	-3.11	0.84	-8.13
2	-3.57	0.77	-8.19
3	-3.55	0.84	-8.61

The issue is how far from the mean value the CA10%MFB have to be or, in other words, what is the corresponding value of the PDF, to consider a cycle pre-ignited. It is inevitable to assume the existence of an uncertainty bandwidth, a “grey” zone, where normally ignited, but at the same time particularly fast combustions, are mixed-up with pre-ignition cycles with a relatively late pre-ignition.

Figure 2.15 shows the three PDFs (relatively to cylinders 1, 2 and 3) of CA10%MFB, calculated for normal cycles. The same graph also presents Dwell Integral versus CA10%MFB (right y-axis scale) for both normal and pre-ignited cycles. A high value of the Dwell Integral index indicates combustion initiation before the Spark Advance, so a threshold could be simply set (0.05 for example) to discriminate pre-ignition cycles.

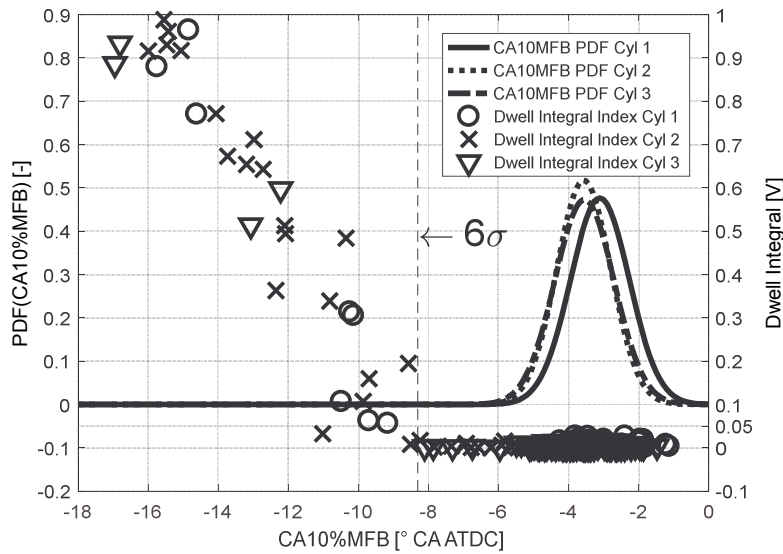


Figure 2.15 - CA10%MFB probability density functions and CA10%MFB vs. Dwell Integral for Test 1

This test represents a suitable pre-ignition phase “sweep” to understand how ion current can detect pre-ignition, and it gives a clear idea on the sensitivity of the ion current information during dwell time (i.e. Dwell Integral) to pre-ignition angular phase (or position). Moreover, as Ion Current Dwell Integral can categorize cycles as unmistakably pre-ignited, a threshold on CA10%MFB can be identified to diagnose clear pre-ignitions. In this case, cycles with CA10%MFB values below  $-9^\circ$  CA are undoubtedly pre-ignited. In order to generalize this concept, such threshold can be defined in terms of  $\mu - n \sigma$ ; in this case a proper value for  $n$  is 6.

Slightly higher values of CA10%MFB than the just defined threshold (i.e. in the interval  $-8, -6^\circ$  CA ATDC), have a very low probability density but a relatively high frequency. Evidently some of these cycles are weakly pre-ignited, meaning that the hot-spot and the spark cooperate in igniting the charge. These cycles, unless they later develop into (heavy) knocking events, are typically not dangerous for the components integrity.

### 2.6.3 Test 2

In another test (Test 2), operating at 6000 RPM, full load and under knocking conditions, some pre-ignitions occurred sporadically in cylinder n° 4. Also in this case, pre-ignition is triggered by a hotspot, but this time as a result of partial oxidation of the electrodes of the spark plug hosting the pressure sensor. In Figure 2.16, ion current signals during dwell time, and corresponding in-cylinder pressure traces, are reported for some of these cycles.

Compared to those of Test 1, these pre-ignition cycles are less severe, in terms of (anticipated) combustion phase and resulting maximum in-cylinder pressure levels. In this case, the response and the content of the ion current signal can be evaluated for pre-ignitions whose combustion start is very close to the spark event.

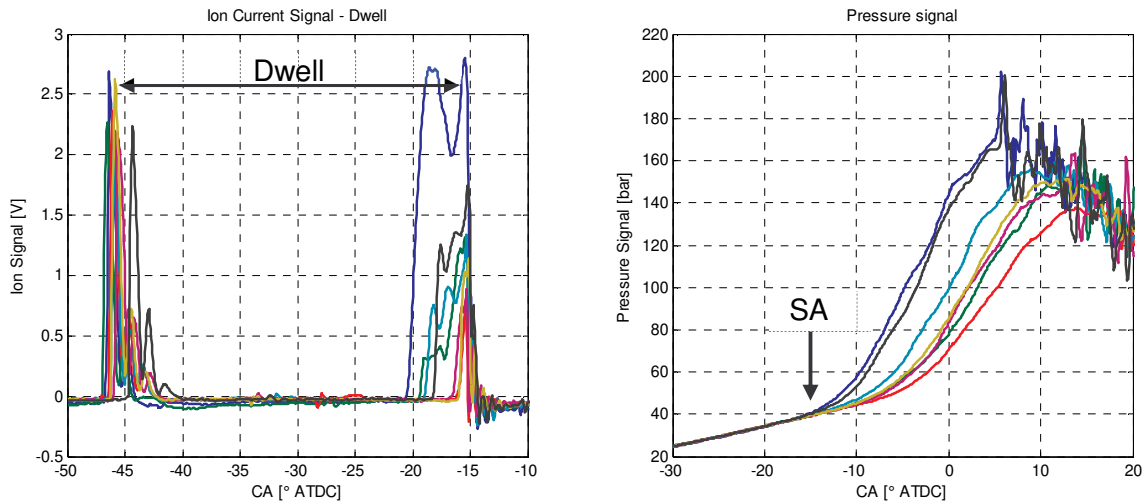


Figure 2.16 - Some pre-ignition cycles in Test 2: Ion signal (left) and corresponding in-cylinder pressure signal (right).

Three probability density functions have been calculated during non-pre-ignition operation, one for each Spark Advance value adopted during the test. Those PDFs are shown in Figure 2.17, and the corresponding parameters are reported in Table 2.4. Once again, Dwell Integral Index quantifies pre-ignition signature on the ion current signal. The same threshold  $\mu - 6\sigma$  adopted above for Test 1 can be applied to discriminate pre-ignition cycles. In this case, 3 threshold levels (one for each Spark Advance value) have been calculated, two of which are practically coincident.

Table 2.4 - CA10%MFB probability density function parameters ( $\mu$ ,  $\sigma$ ) and pre-ignition threshold ( $\mu - 6\sigma$ ), for different SA values.

SA [°CA BTDC]	$\mu$ [°CA ATDC]	$\sigma$ [°CA ATDC]	$\mu - 6\sigma$ [°CA ATDC]
14.25	3.37	0.98	-2.49
15	2.7	0.87	-2.5
15.75	2.01	0.86	-3.15

As shown in Figure 2.17, and as a confirmation of what was demonstrated in the previous paragraph, distinction between cycles with pre-ignition and normally ignited is not clear-cut. Considering again the threshold value 0.05 for Dwell Integral index, some pre-ignition cycles (defined by Dwell Integral  $> 0.05$ ) have a relatively high CA10%MFB value, while one or more cycles are evidently pre-ignited but Dwell Integral index is practically null (as under normal combustion operation).

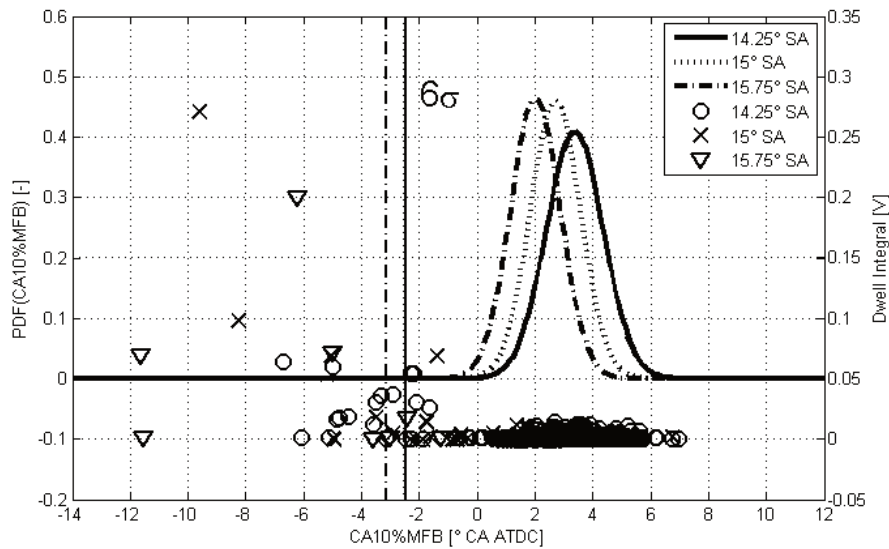


Figure 2.17 - CA10%MFB probability density functions and CA10%MFB vs. Dwell Integral for Test 2.

This probably depends on the location of the combustion initiation. For Test 2, pre-ignition cause is not perfectly clear (or it was possibly caused by concurrent factors). If some pre-ignitions were not triggered by a hot spot in the spark plug but they started from a peripheral region of the combustion chamber, the ion current sensing element (spark plug electrodes) would be exposed to the flame front with a certain delay. If the ignition point is far enough away from the spark plug, the flame front can reach the spark plug electrodes after the spark time, resulting in a flat dwell time ion current signal.

#### 2.6.4 Pre-Ignition Phase

For those pre-ignition cycles detectable by the ion current signal (corresponding to a Dwell Integral value higher than a reasonable threshold), ion current signal can provide information about the angular position corresponding to the pre-ignition flame front, as it could already be seen in Figure 2.13 and Figure 2.16. This idea can be implemented by a simple algorithm, reported in Figure 2.18, which allows identifying the angular position (limited to the dwell angular window) for which the ion current signal exceeds a defined threshold (0.5 V in this case). We will call this angle PI Phase.

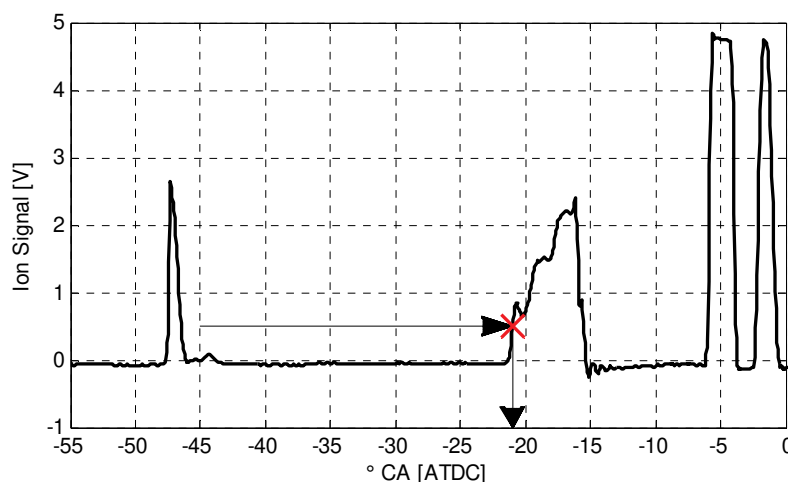


Figure 2.18 - Pre-Ignition (PI) Phase identification algorithm.

Of course, Dwell Integral and PI Phase are related to each other: an earlier PI Phase corresponds to a higher value of the integral. But while Dwell Integral value depends on Spark Advance angle, which defines the window end for the calculation, PI Phase is an absolute indication of the pre-ignition flame initiation position. In this way, it is possible to compare data from different tests, such as Test 1 and Test 2.

In Figure 2.19, PI Phase versus CA10%MFB are represented, for both data sets. Results are very superimposable, as it should be supposing a similar angular duration 0-10%MFB for both tests. All points represented, for both tests, are identified by a Dwell Integral value greater than 0.05, the threshold proposed above. In Figure 2.19, it can be noted that PI Phase values are necessarily lower than the applied spark advance, that is 20° CA BTDC (or -20° CA ATDC) for Test 1 and around 15° CA BTDC (-15° CA ATDC) for Test 2.

Pre-ignition cycles whose combustion started far from the spark plug (and therefore ion current signal would eventually give evidence of such anomaly with an angular delay), will locate above the line definable in Figure 2.19 by interpolating the available data. In Test 2, there is very little margin (about 5° CA) between the earlier PI Phase measured and the applied Spark Advance. This is why some clear pre-ignition cycles (evidently ignited far from the spark plug) from Test 2 have not been “seen” by the ion current signal and have been cut-off from this graph.

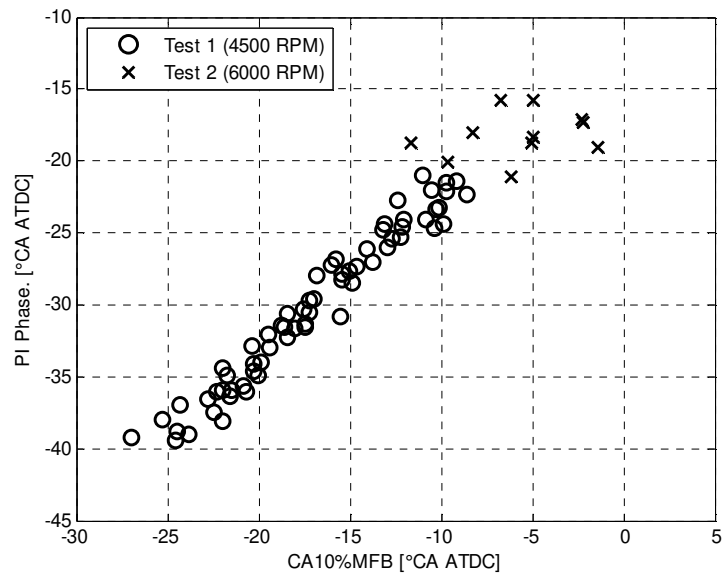


Figure 2.19 - Pre-Ignition Phase versus CA10%MFB, for both Test 1 and Test 2.

## 2.7 Conclusions

The aim of this study is to confirm the robustness and the reliability of the ion signal to describe combustion features, both concerning combustion phasing and knock intensity, and to demonstrate how such information can be used to perform a fully closed-loop, real-time Spark Advance controller, both in knock-free and knock-limited operation, which is the element of novelty of this paper.

Pressure- and ion current-based combustion closed-loop control is compared, by implementing both solutions in real-time. Both controllers are characterized by an aggressive strategy, which pursues the optimal combustion angular phase, and by a protective action governed by measured knocking levels. The study demonstrates the feasibility of combustion phase ion-based real-time closed-loop control, achieving very similar performance to the pressure-based control. The concept has been applied to a single operating condition, but it is extendible to the whole engine operating domain, thus allowing significant calibration costs and time reduction, and permanent fuel consumption optimization.

Moreover, ion current signal can be extremely helpful to real-time diagnose pre-ignition combustions. An ion signal pre-ignition index (i.e. Dwell Integral index) results having nearly the same sensitivity (or uncertainty) as the evaluation, by a skilled operator or by a well-calibrated signal processing algorithm, of an equivalent pressure-based index (CA10%MFB) in identifying pre-ignitions. Further, this work can give some guidance about interpreting combustion angles to discriminate pre-ignitions.

Furthermore, the strong link between the angular position of the rising edge of the ion signal and the

combustion angular phase confirms the robustness of the ion signal information content. Local nature of this signal can occasionally lead to misdetection, if flame initiation occurs far from the spark plug electrodes.

With some attention to avoid signal noise interferences, the diagnostic algorithm can be rapidly implemented in the ECU, to promote a closed-loop combustion control reaction in case of severe pre-ignition events, possibly before the subsequent combustion takes place.

## 2.8 References

- [2.1] X. Storm, H. Salminen, R. Virrankoski and S. Niemi, "Analysis of cylinder pressure measurement accuracy for internal combustion engine control", SAE Technical Paper 2017-01-1067, 2017.
- [2.2] L. Eriksson, "Methods for Ionization Current Interpretation to be Used in Ignition Control", Master Degree Project in Vehicle Systems at the Technical University of Linköping, Sweden, 1995.
- [2.3] J.B. Heywood, "Internal combustion engine fundamentals", New York, McGraw Hill, 1988.
- [2.4] N. Cavina, D. Moro, L. Poggio and D. Zecchetti, "Individual cylinder combustion control based on real-time processing of Ion current signals", SAE 2007 Transactions - Journal of Engines, Section 3 - Vol.116, 2007.
- [2.5] A. Businaro, N. Cavina, E. Corti et al, "Accelerometer Based Methodology for Combustion Parameters Estimation", Energy Procedia 81 (2015) 950–959, 2015.
- [2.6] G. Malaczynski, G. Roth, D. Johnson, "Ion-Sense-Based Real-Time Combustion Sensing for Closed Loop Engine Control", SAE Int. J. Engines 6(1):2013, doi:10.4271/2013-01-0354, 2013.
- [2.7] Y. Cao and L. Li "A Novel Closed Loop Control based on Ionization Current in Combustion Cycle at Cold Start in a GDI Engine", SAE Technical Paper 2012-01-1339, 2012.
- [2.8] M. Glavmo, P. Spadafora and R. Bosch "Closed Loop Start of Combustion Control Utilizing Ionization Sensing in a Diesel Engine", SAE Technical Paper 1999-01-0549, 1999.
- [2.9] N. Henein, W. Bryzik, A. Abdel-Rehim and A. Gupta "Characteristics of Ion Current Signals in Compression Ignition and Spark Ignition Engines", SAE Int. J. Engines 3(1):260-281, 2010, doi: 10.4271/2010-01-0567.
- [2.10] I. Andersson "A Comparison of Combustion Temperature Models for Ionization Current Modelling in an SI Engine", SAE Technical Paper 2004-01-1465, 2004.
- [2.11] V. Giglio, G. Police, N. Rispoli et al., "Experimental Investigation on the Use of Ion Current on SI Engines for Knock Detection", SAE Technical Paper 2009-01-2745, 2009.
- [2.12] D. Kumar, A. Ramesh, M. Babu and P. Manivannan, "An Ionization Current based Cylinder Gas Pressure Estimation for Knock Detection and Control in a Single Cylinder SI Engine", SAE Technical Paper 2009-32-0118, 2009.
- [2.13] D. Panousakis, A. Gazis, J. Paterson, W. Chen et al., "Ion Current Signal Interpretation via Artificial Neural Networks for Gasoline HCCI Control", SAE Technical Paper 2006-01-1088, 2006.
- [2.14] Cavina N, Poggio L and Sartoni G (2011) Misfire and Partial Burn Detection based on Ion Current Measurement. SAE Int. J. Engines 4(2):2451-2460, doi:10.4271/2011-24-0142.
- [2.15] N. Cavina, N. Rojo, L. Poggio, L. Calogero et al., "Investigation on Pre-Ignition Combustion Events and Development of Diagnostic Solutions Based on Ion Current Signals", SAE Int. J. Engines 10(4):2017, doi:10.4271/2017-01-0784.



- [2.16] D. Upadhyay and G. Rizzoni, "AFR Control on a Single Cylinder Engine Using the Ionization Current", SAE Technical Paper 980203, 1998.
- [2.17] E. Corti, C. Forte, "Statistical analysis of indicating parameters for knock detection purposes", SAE Technical Paper 2009-01-0237, 2009.
- [2.18] J. Spelina, J. Peyton Jones, J. Frey, "Recent advances in knock analysis, simulation, and Control", SAE International Journal of Engines 7(2):947-955, 2014.
- [2.19] N. Cavina, G. Po, L. Poggio, "Ion current based spark advance management for maximum torque production and knock control", 8th Biennial ASME Conference on Engineering Systems Design and Analysis. Torino, Italy, 4-7 July, 2006.
- [2.20] N. Cavina, N. Rojo, A. Businaro, L. Ceschini, E. Balducci, A. Cerofolini, "Analysis of pre-ignition combustions triggered by heavy knocking events in a turbocharged GDI engine", Energy Procedia 101:893-900, 2016, DOI: 10.1016/j.egypro.2016.11.113.
- [2.21] A. Zahdeh, P. Rothenberger, W. Nguyen, M. Anbarasu et al., "Fundamental Approach to Investigate Pre-Ignition in Boosted SI Engines," SAE Int. J. Engines 4(1): 246-273, 2011, doi:10.4271/2011-01-0340.
- [2.22] P. Haenel, P. Seyfried, H. Kleeberg and D. Tomazic, "Systematic Approach to Analyze and Characterize Pre-ignition Events in Turbocharged Direct-injected Gasoline Engines," SAE Technical Paper 2011-01-0343, 2011, doi:10.4271/2011-01-0343.
- [2.23] J. Zaccardi, L. Duval and A. Pagot, "Development of Specific Tools for Analysis and Quantification of Pre-ignition in a Boosted SI Engine," SAE Int. J. Engines 2(1):1587-1600, 2009, doi:10.4271/2009-01-1795.

## 3 Water Injection

This chapter presents simulation and experimental results of an activity carried out to evaluate the effects of intake water injection on the main combustion parameters of a turbo-charged, direct injection spark ignition engine, which has been already described in "Investigation of Water Injection Effects on Combustion Characteristics of a GDI TC Engine", published in the SAE International Journal of Engines (SAE Int. J of Engines 10(4):2209-2218, 2017, ISSN 1946-3944, doi: 10.4271/2017-24-0052).

Initially, main results of a one-dimensional simulation are presented: the analysis is carried out to highlight the key parameters (injection position, water-to-fuel ratio and water temperature) and their effects on combustion (in-cylinder and exhaust temperature reduction and knock tendency suppression). The main results of such study have then been used to design and conduct preliminary experimental tests on a prototype direct-injection, turbo-charged spark ignition engine, modified to incorporate a new multi-point water injection system in the intake runners. The experiments allowed to validate the model results, demonstrating the effectiveness of the proposed technology, and to further investigate on the mechanisms that allow controlling thermal load and knocking tendency by varying the water-to-fuel ratio.

### 3.1 Introduction

High load conditions for SI engines, especially in downsized and boosted engines, are heavily limited in terms of achievable efficiency levels by two main issues: excessive exhaust temperatures and heavy knocking operation. Exhaust temperatures cannot exceed maximum tolerable inlet temperature of the turbine, determined by speed and used materials (such limit is about 1000-1050°C for conventional turbochargers), and the common solution is to operate with rich mixture (exploiting heat subtraction due to fuel evaporation) waiving to after-treatment possibilities and heavily increasing fuel consumption.

The other main limit is imposed by knocking combustion, which occurs at high load conditions, due to high in-cylinder temperature and pressure levels. This forces to adopt a sub-optimum Spark Advance (SA) angle, thus reducing maximum temperature and knock intensity, while correspondingly increasing exhaust temperatures, with respect to maximum efficiency conditions.

Such strategies are no longer compatible with new homologation regulations and corresponding real driving cycles and consumption and emission upper bonds, so much that a pre-treatment of the fresh mixture seems to be a promising solution.

Water injection is a well-known technology, and many examples of its implementation can be found [3.1, 3.2, 3.3]. The principle consists in reducing charge and combustion temperature by means of the high latent heat of vaporization of injected liquid water. This yields benefits both in terms of exhaust temperature and knock intensity reduction.

In the next years, water injection will probably become a standard equipment for many production engines [3.4, 3.5].

This work investigates port water injection possibilities, since this layout results in no modification or complication of the cylinder head and can be easily installed on a pre-existing engine. The simplicity of this layout may compensate extra benefits and operation flexibility obtainable with direct water injection. The investigation here presented was carried out by 1-D modelling analysis in a first stage, then experimental tests were conducted in order to verify and validate the model.

### 3.2 Water injection and knock model

To evaluate water injection effects on combustion, a 1-D model of the engine has been developed in Gt-Power [3.6] environment. In this first stage, a single-cylinder model has been set, to reduce computational efforts.

### 3.2.1 Model layout

The developed engine model is based on a 1-D representation, and only one cylinder, in this first stage, is considered. Moreover, components upstream the intake and downstream the exhaust manifolds have been neglected. Model calibration has been carried out through experimental data, without water injection, in several operating conditions.

Combustion simulation is governed by a predictive model, which should be sensitive to in-cylinder variations of the charge physical properties due to heat subtraction operated by water evaporation.

To consider water film formation and evaporation dynamics in the intake ports, *PipePort* and *FlowSplitPort* templates have been used, which are designed to model PFI injection [3.6].

Of the total amount of port-injected water, a fraction will evaporate within the intake manifold, with some kind of interaction (fluid film) with the duct walls, while the remaining fraction should enter the combustion chamber still in liquid form. Figure 3.1 shows a schematic of the developed 1-D model.

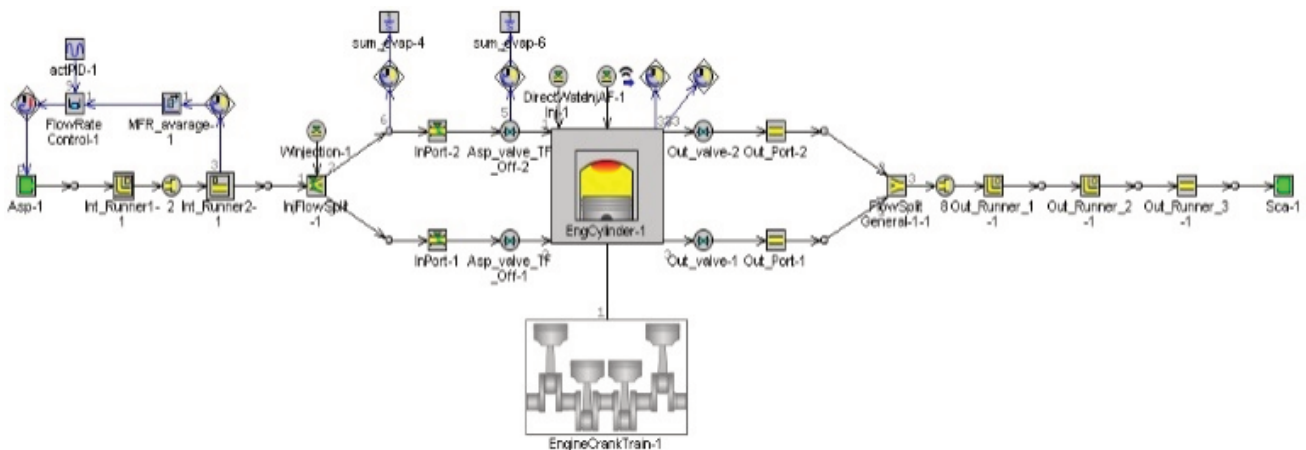


Figure 3.1 - Gt-Power model layout. Intake, cylinder and exhaust sub-models are shown from left to right

To control the amount of liquid water entering the cylinder, a fictitious direct injector was added in the model. For this injector, injected water instantaneously evaporates (for hypothesis), and in this way evaporation rate for the liquid mass fraction that reaches the combustion chamber can be controlled (i.e., imposed) by the direct injection rate. Instead, all the port-injected water in the model is forced to evaporate within the intake ports.

### 3.2.2 Water injection modelling parameters

The total amount of injected water is described by  $r$ , which is the ratio between injected water quantity and stoichiometric fuel mass. This convenient normalization is proposed in [3.1].

The split between port-injected and (fictitious) directly-injected water mass is described, and user-imposed, by  $F_i$  and  $F_d$ , which represent the port-injected and directly-injected water mass fractions, respectively. By definition, the sum of these two parameters is 1.

The Start of Injection (Sol) for the port injector, due to the model structure and hypothesis, has practically no effects. This is one of the main limits of this model, which cannot represent tridimensional interactions between evaporating water spray and pressure waves in the intake manifolds.

In-cylinder injection start is imposed at IVO (Intake Valve Opening), since it should model port-injected liquid water entering the combustion chamber during the intake stroke. This hypothesis is not necessarily verified: depending on the port-injection timing, injected water may not enter into the cylinder during the first part of the intake stroke.

Injection (and therefore evaporation) duration is imposed too, and described by the parameter ToE: Time of Evaporation, which will be considered below in terms of equivalent crank angle interval (for now, evaporation rate, or equivalently direct injector mass flow, is supposed to be constant).

The split between in-cylinder and in-runner water evaporation (i.e.  $F_d$  and  $F_i$ ) has to be identified and

calibrated, as well as the parameter ToE, depending on injection phasing and engine operating conditions. Indeed, this modelling approach is relatively simple but it is not predictive.

A first sensitivity analysis to these parameters variations has been conducted using the above described model. In this way, parameters that effectively represent degrees of freedom of the model can be identified to fit experimental data. Other parameters, which do not significantly affect the model outputs, due to the grey/black-box nature of this part of the model, or because of expected very weak physical correlations, will be kept constant.

Location of the water evaporation (where it takes place) has a severe impact on the useful effect of water injection or, equivalently, on water consumption. As shown in Figure 3.2, by varying the parameter  $F_i$  from 0 to 1 (corresponding to  $F_d$  variations from 1 to 0), the same water mass ( $r = 0.5$ , in this case) progressively produces minor impact on in-cylinder temperature. The engine operating point related to Figure 3.2 is defined by engine speed equal to 3000 rpm and intake manifold pressure equal to 1.5 bar, with a constant SA of  $13^\circ$  CA Before Top Dead Center (BTDC), but the results are qualitatively valid also for different operating conditions.

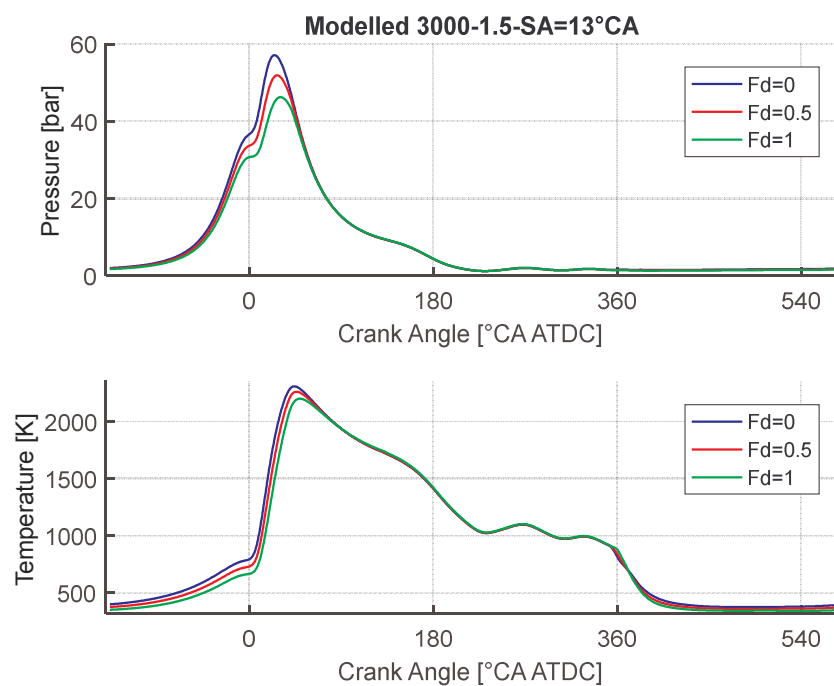


Figure 3.2 - Effect of  $F_d$  variation for fixed water quantity. Top graph represents such effects on the in-cylinder pressure profile, while in the bottom graph the corresponding effect on the in-cylinder temperature is shown. Temperature reduction achievable with direct injection is the highest.

This means that direct injection is undoubtedly the best solution.

These evidences confirm results reported in [3.1] and suggest, supposing a port injection solution, an injector installation as close as possible to the intake valves, while a single-point configuration is not recommended.

Figure 3.3 clearly shows that also the angular position of the in-cylinder evaporation (i.e. by varying in-cylinder injection duration, since the SOI is bonded to IVO event) affects temperature reduction, for fixed  $r$  and  $F_i/F_d$  values.

Figure 3.3 is related to the same operating conditions of Figure 3.2, and the effect of ToE parameter is shown: the later (or longer) the evaporation in the compression stroke, the higher the temperature reduction. Also in this case, such considerations can be generalized, as verified by applying the very same model to different engine operating conditions.

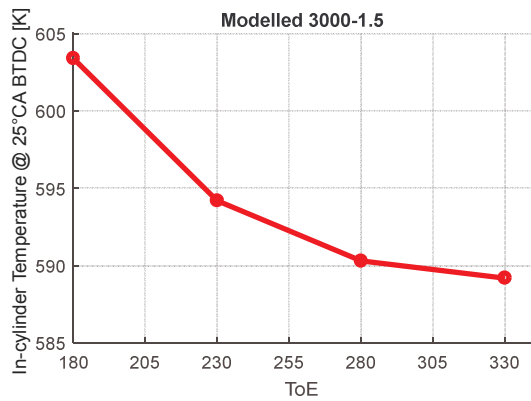


Figure 3.3 - Simulated in-cylinder temperature during the compression stroke (25°CA BTDC) depending on ToE parameter. As in-cylinder evaporation duration (ToE) is longer, the charge temperature is lower.

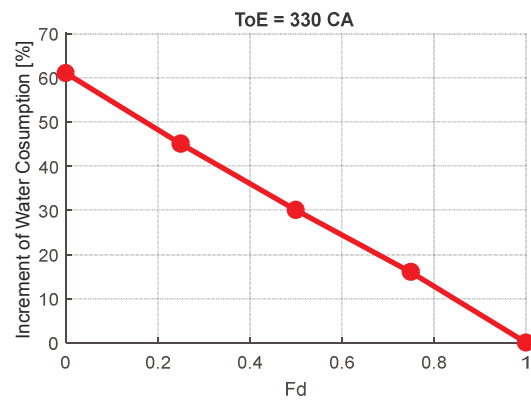


Figure 3.4 - Percentage increase of water consumption, for fixed maximum in-cylinder temperature, depending on the evaporation split between intake ducts (Fi) and combustion chamber (Fd).

Injected liquid water temperature does not significantly affect model response, as heat subtraction is given basically by its latent heat of evaporation. This means that, supposing an on-board application, water tank position under the bonnet is not particularly constrained.

As mentioned before, the model is not sensitive to SOI variations for the port injector, contrary to how the real process is expected to behave.

Similarly, water consumption dependence on these parameters can be analysed, for given useful temperature reduction effect. In Figure 3.4, the increment of water consumption is evaluated as a function of  $F_d$  (i.e. the fraction of water that evaporates within the cylinder), compared to a direct injection ( $F_d = 1$ ). This analysis is done with fixed ToE, in this case equal to 330°CA, while  $r$  is determined to achieve the target effect, which is the same in-cylinder maximum temperature. The engine operating point is the same as the one shown in previous figures, and in the subsequent Figure 3.5.

By transferring the evaporation process from the cylinder to the intake ducts, the increase of water consumption is very significant (up to 60%) to achieve the same effect on the in-cylinder conditions. In Figure 3.5 the same kind of analysis is carried out with respect to ToE parameter. Reported values describe the increase of water consumption, compared to a full direct injection with ToE equal to 180°CA, as a function of parameter ToE. Also in this case, the longer the evaporation duration, the lower the water consumption to achieve the same target effect.

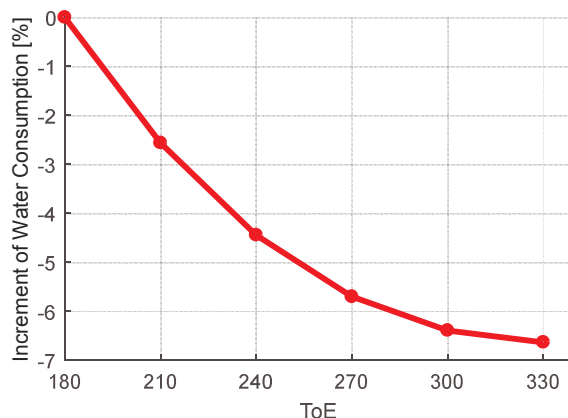


Figure 3.5 - Percentage increase of water consumption, for fixed maximum in-cylinder temperature, depending on the imposed duration of the in-cylinder evaporation. As the in-cylinder evaporation is longer (ToE), a lower value of  $r$  is required.

Therefore, considering an external water injection layout, it is clear the importance of the injector location and installation, in order to achieve maximum benefits while minimizing water consumption.

Going back to the analysis reported in Figure 3.4, it is now clear that a long duration of the in-cylinder evaporation process is desirable, so that the trend reported in the same figure is the most pessimistic,

while if considering a shorter duration (i.e. lower ToE value) the increase of water consumption corresponding to a reduction of Fd is lower.

### 3.2.3 Knock model

The selected approach to model knocking combustion requires the cycle-to-cycle variability (CCV) to be modelled, which can be obtained through stochastic variations of the main influencing parameters. In this way, the model generates a statistical distribution for each selected parameter, and every modelled combustion process is different from the previous. Knock model is then deterministically applied to every stochastic combustion, achieving a statistical distribution of the knock index.

To model CCV, equations proposed in [3.7] have been implemented. In the following, the empirical relationship adopted between CCV and variation of laminar flame speed and kernel growth speed is described. Model equations define the standard deviation of these two quantities as follows:

$$S_F[\%] = \left( e^{\frac{0.9285 - \chi_{ZS}}{0.17}} B_m^{-\chi_{ZS}} NF(\chi_{ZS}) \right) \quad (3.1)$$

$$NF(\chi_{ZS}) = \left( \frac{BD1090}{1000} \right)^{\chi_{ZS}-1} BD0010^{0.5 \chi_{ZS}} \left( \frac{T_{u,max}}{T_{ref}} \right)^{2(\chi_{ZS}+1)} \quad (3.2)$$

$$\chi_{ZS} = \chi_{ZS,mod} + 0.008 \chi_n \left( \frac{n}{1000} \right)^{-2} \quad (3.3)$$

$$EP = \varphi_{ZS} + 2.6 \varphi_n \left( \frac{n}{1000} \right)^{-2} \quad (3.4)$$

Where:

- $S_F[\%]$  is the percentage standard deviation of laminar flame speed
- $B_m$  is the maximum value of laminar flame speed
- $T_{u,max}$  is the maximum exhaust gas temperature
- $n$  is the engine speed
- BD1090 and BD0010 are the burn duration from 10 to 90 % and from 0 to 10 % of fuel mass fraction
- $\chi_{ZS,mod}$  is the *Laminar Flame Speed Variation Multiplier*
- $\chi_n$  is a no dimensional quantity, normally set to 1
- $EP$  is standard deviation of kernel growth speed
- $\varphi_{ZS}$  is the *Flame Kernel Growth Variation Multiplier*
- $\varphi_n$  is a non-dimensional quantity, normally set to 1

Calibration of the CCV model has been carried out by varying *Laminar Flame Speed Variation Multiplier* and *Flame Kernel Growth Variation Multiplier*, to minimize the parameter  $f_{o,ccv}$ , defined by the following equation:



$$f_{o,CCV} = 2 \left( \frac{STD_{imep,GT} - STD_{imep,ex}}{STD_{imep,ex}} \right)^2 + \left( \frac{STD_{pmax,GT} - STD_{pmax,ex}}{STD_{pmax,ex}} \right)^2 + \left( \frac{STD_{CA50,GT} - STD_{CA50,ex}}{STD_{CA50,ex}} \right)^2 \quad (3.5)$$

In equation (3.5),  $STD_{x,GT}$  is the standard deviation of the quantity “x” calculated by GT Power and  $STD_{x,ex}$  is the standard deviation of the same “x” quantity experimentally measured in the test cell.

Then, the *Kinetics Fit* method [3.8] has been applied, in order to model knock intensity. This model calculates a knock index, whose value or intensity depends on the unburned fuel mass when auto-ignition conditions are reached in the combustion chamber. The adopted knock index has been defined as follows:

$$KI = 1000 M u_b \left( \frac{V_{TDC}}{V} \right) e^{\left( \frac{-6000}{T_u} \right)} \max(0.1 - (1 - \phi)^2 I_{ave}) \quad (3.6)$$

Where:

- $M$  is the *Knock Index Multiplier*
- $u_b$  is the unburned fraction of the mixture when auto-ignition occurs
- $V_{TDC}$  is the in-cylinder volume at TDC
- $V$  is the in-cylinder volume when auto-ignition occurs
- $T_u$  is the temperature of the unburned mass fraction
- $\phi$  is the equivalence ratio of the unburned zone
- $I_{ave}$  is the integral of the induction time

Induction time integral is defined by the following expression:

$$I(t) = \int_{SOC}^t \frac{1}{\tau} dt \quad (3.7)$$

Where  $SOC$  is the Start Of Combustion and  $\tau$  is the Induction Time (autoignition delay) defined as follows:

$$\frac{1}{\tau} = \frac{1}{\tau_1 + \tau_2} + \frac{1}{\tau_3} \quad (3.8)$$

$$\tau_i = M_1 a_i \left( \frac{RON}{100} \right)^{b_i} [Fuel]^{c_i} [O_2]^{d_i} [Dilution]^{e_i} \exp \left( \frac{f_i}{M_2 T} \right)$$

for  $i = 1, 2, 3$

$$(3.9)$$

Where:

- $\tau_1, \tau_2$  and  $\tau_3$  are Induction Times for low, intermediate and high temperature regions
- $RON$  is the fuel Research Octane Number
- $[Fuel]$  is the fuel concentration (mol/m<sup>3</sup>)
- $[O_2]$  is the oxygen concentration (mol/m<sup>3</sup>)
- $[Dilution]$  is the sum of concentration of N<sub>2</sub>, CO<sub>2</sub> and H<sub>2</sub>O (mol/m<sup>3</sup>)
- $M_1$  is the *Knock Induction Time Multiplier*
- $M_2$  is the *Activation Energy Multiplier*
- $a_i, b_i, c_i, d_i, e_i$  and  $f_i$  are coefficients depending on the selected model (*Kinetics Fit*)

These expressions represent an empirical model developed by Gamma Technologies [3.6] that is used to predict knocking conditions: knock occurs when the integral defined by Equation (3.7) becomes equal to 1. Authors are also developing a custom definition of the modelled knock intensity (UKI, User Knock Index), for now as a function of the Gt-Power Knock Index (KI) and other operating parameters. Being an on-going activity, UKI definition is not reported in this work.

KI and UKI have been calibrated by comparing the simulated knock index (UKI, for example) with experimental knock index values, by minimizing the parameter  $f_{o,knock}$ , defined by Equation (3.10). As for CCV, knock model calibration is carried out by identifying optimal values of the *Knock Index Multiplier*, the *Knock Induction Time Multiplier* and the *Activation Energy Multiplier*, in addition to other parameters defined by the authors. As a reference knock index, MAPO (Maximum Amplitude of Pressure Oscillation) has been chosen since it represents one of the most widely used, and accepted, knock indicators [3.9-3.11].

$$f_{o,knock} = \left( \frac{30_{UKI} - 30_{MAPO}}{30_{MAPO}} \right)^2 + \left( \frac{50_{UKI} - 50_{MAPO}}{50_{MAPO}} \right)^2 + \left( \frac{98_{UKI} - 98_{MAPO}}{98_{MAPO}} \right)^2 \quad (3.10)$$

where  $X_{UKI}$  is the X percentile of the User Knock Index and the  $X_{MAPO}$  is the X percentile of the experimental MAPO index.

Since knock is a stochastic phenomenon, the only viable approach is to consider the statistical distribution of the experimental and modelled knock indexes. Authors considered CDF (Cumulative Distribution Function) of the two quantities, and the aim of the calibration process is to obtain the most similar distributions, summarized in the objective function by three singular percentile values.

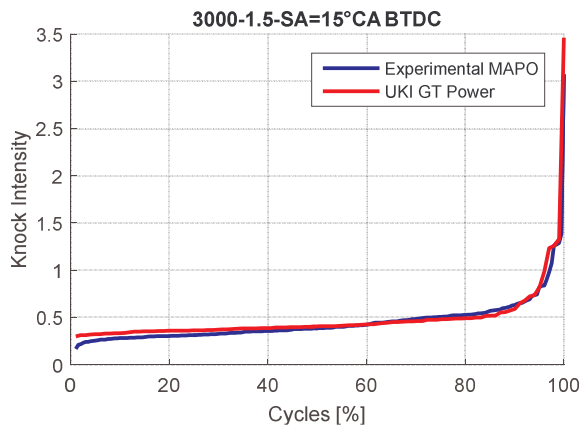


Figure 3.6 - Comparison between experimental MAPO and predicted User Knock Index, for the SA value used during model calibration.

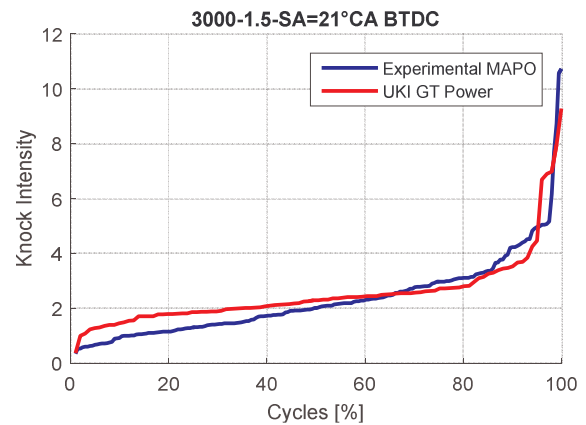


Figure 3.7 - Comparison between experimental MAPO and predicted User Knock Index, for the SA value used during model validation.

Calibration results are reported in figures 3.6 and 3.7, showing a good agreement between modelled and experimental knock intensities. Tuning parameters have been calibrated using a light-medium knock operating condition (Figure 3.6), while the validation of the model has been verified under conditions corresponding to higher spark advance angles, and therefore with higher knock intensity (Figure 3.7). As mentioned, the reference experimental knock index is MAPO, defined by the following Equation (3.11):

$$MAPO = \max\left(\text{abs}(p_{filt})\right) \quad (3.11)$$

where  $p_{filt}$  is the in-cylinder pressure signal high-pass filtered at 5 kHz.

Partly depending on the combustion model predictivity, this model should bring forward water injection potential on knock reduction.

### 3.2.4 Modelling results

Some simulations regarding SA and  $r$  sweeps have been run to analyse their combined effects on the combustion process, while keeping constant the following parameters:

- $F_i = 0.6$
- $ToE = 330^\circ CA$
- $wT = 80^\circ C$

For consistency, the operating point considered next is again 3000 rpm, 1.5 bar of intake manifold pressure, and stoichiometric mixture.

#### 3.1.4.1 Combustion phasing

One of the aspects that should be considered to evaluate engine response to water injection, is the effect on combustion. As the mass of water increases, combustion should shift towards the exhaust stroke for the same spark advance, because of lower in-cylinder temperatures. Predicted values for CA50%MFB (angle corresponding to 50% of mass burnt) as a function of the applied Spark Advance (SA) are reported in Figure 3.8.

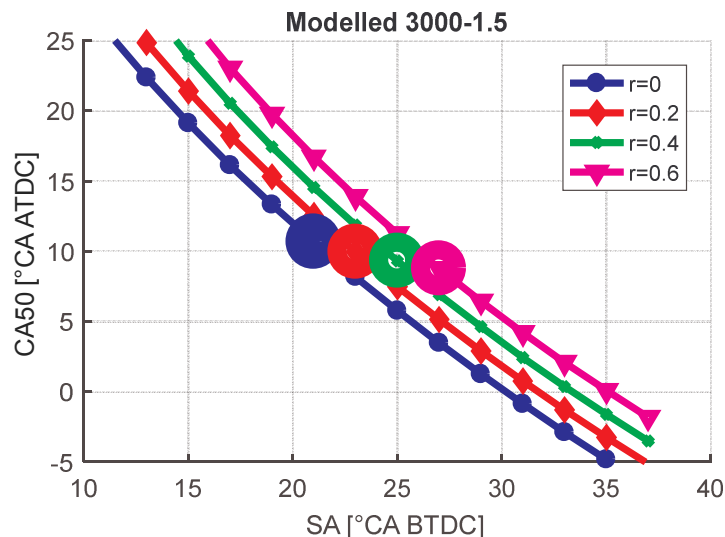


Figure 3.8 - CA50%MFB as a function of applied SA, for different water mass fractions.

According to the model, as water mass increases, combustion slows down. This means that an additional effort is necessary for the spark advance calibration, or that an on-board closed-loop combustion control could be very convenient. Also, CA50%MFB corresponding to maximum efficiency condition is lower as water ratio increases (represented by large circular markers in Figure 3.8).

#### 3.1.4.2 Exhaust temperature

As described in the previous paragraph, water injection affects combustion phasing. Because of the exhaust temperature dependence on combustion phasing, water injection effect on such quantity should not be compared at fixed spark advance. Supposing the operating point is not knock limited, exhaust temperature difference/reduction should be compared under maximum efficiency conditions (which can be obtained with about the same CA50%MFB), for every water mass quantity, and consequently with different spark advance angles.

In Figure 3.9 modelled exhaust temperature reduction is reported as a function of CA50%MFB, for different

values of  $r$ . The point considered as reference is the blue big dot in Figure 3.9, corresponding to the maximum efficiency spark advance for the case without injected water ( $r = 0$ ). For example, with 60% of injected water with respect to the stoichiometric fuel mass ( $r = 0.6$ ), a reduction of about 50°C is achievable when comparing maximum efficiency conditions.

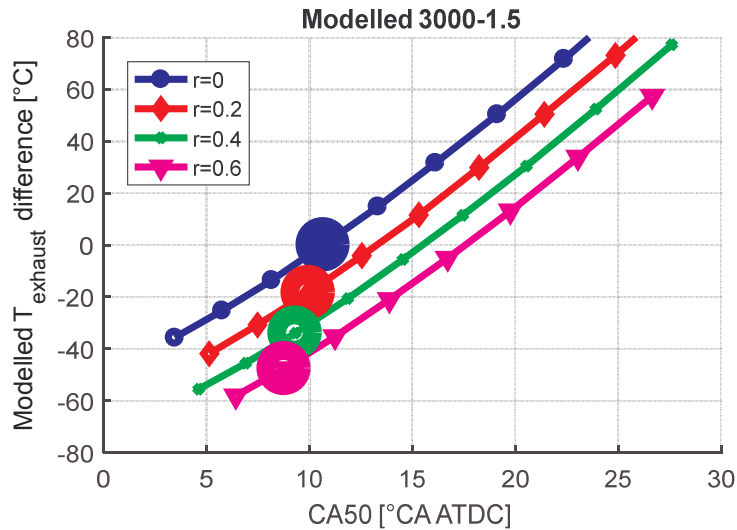


Figure 3.9 - Modelled exhaust temperature reduction as a function of CA50%MFB and water ratio.

### 3.1.4.3 Knock

Figure 3.10 reports UKI values calculated by the model, for different values of  $r$  and SA. The predicted knock reduction is substantial, even though, again, different curves should not be compared at fixed spark advance.

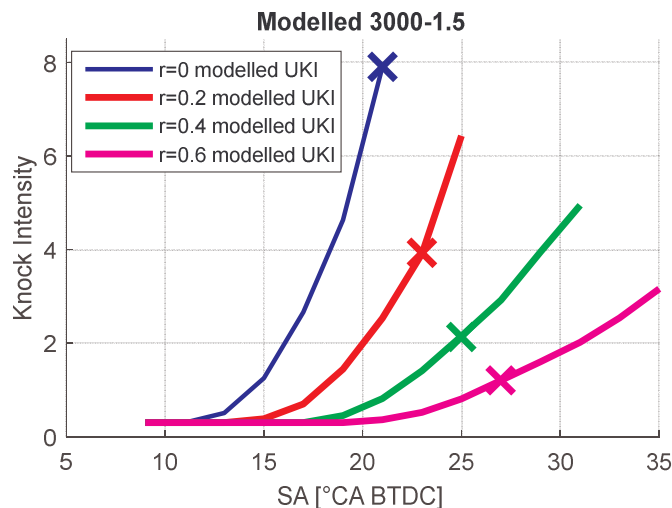


Figure 3.10 - Modelled knock intensity as a function of Spark Advance and water ratio. Water injection heavily reduces knock intensity.

## 3.3 Experimental tests

Experimental tests have been conducted on a prototype Gasoline Direct Injection (GDI) turbocharged Spark Ignition (SI) engine, whose intake system has been modified in order to install port water injectors and rail.

### 3.3.1 Experimental setup

In Figure 3.11 the modified intake manifold water rail and injectors are visible. Water injectors location is as close as possible to the intake valves, according to the model indication about water evaporation dynamics. Water injectors and pump are controlled by a RCP (Rapid Control Prototyping) system developed by this research group in collaboration with Alma Automotive, by which it is possible to control injection timing and rail pressure, with great flexibility.

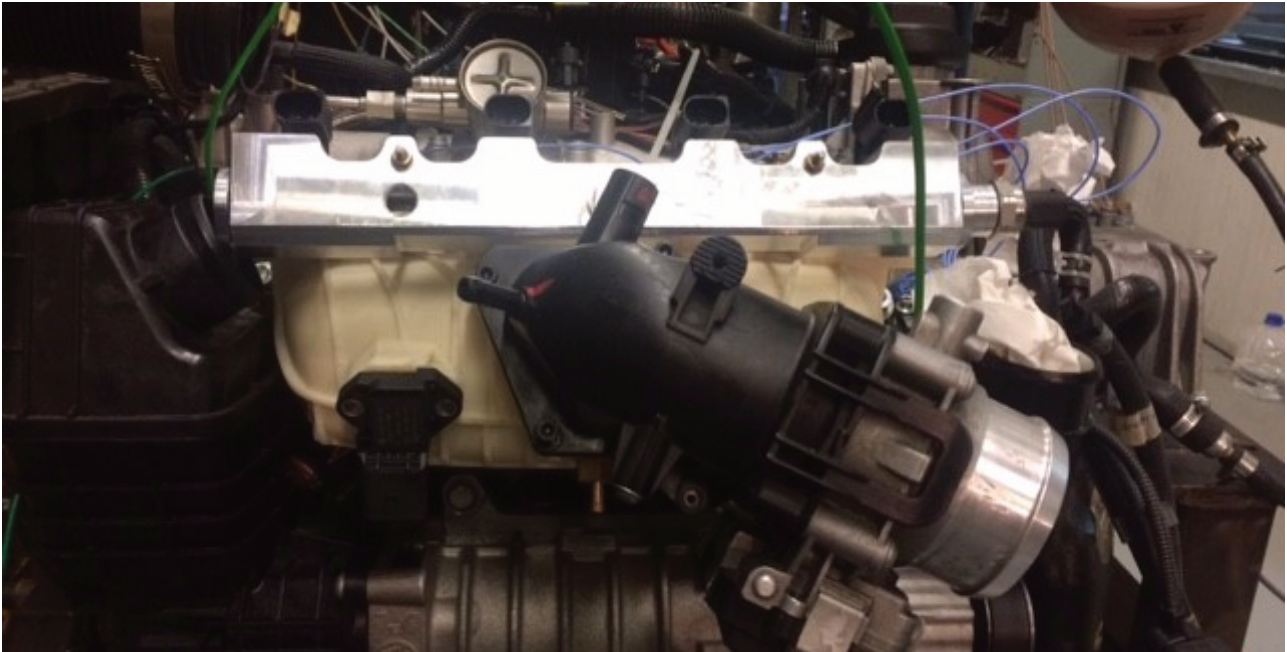


Figure 3.11 - Detail of the experimental setup: modified intake manifold and water rail are visible.

Experimental data here presented have been obtained with constant injection pressure and timing, 10 bar and 360°CA ATDC (beginning of the intake stroke), respectively. Such values have not yet been optimized, and a detailed sensitivity analysis is now taking place, during the second part of the project. Injection phasing is expected to be a very significant parameter and will be carefully investigated.

Engine operating point is the same considered as an example: 3000 rpm, 1.5 bar of intake manifold pressure, and stoichiometric mixture. All cylinder pressure data have been acquired and analyzed, then the “mean” cylinder has been considered in all the figures below.

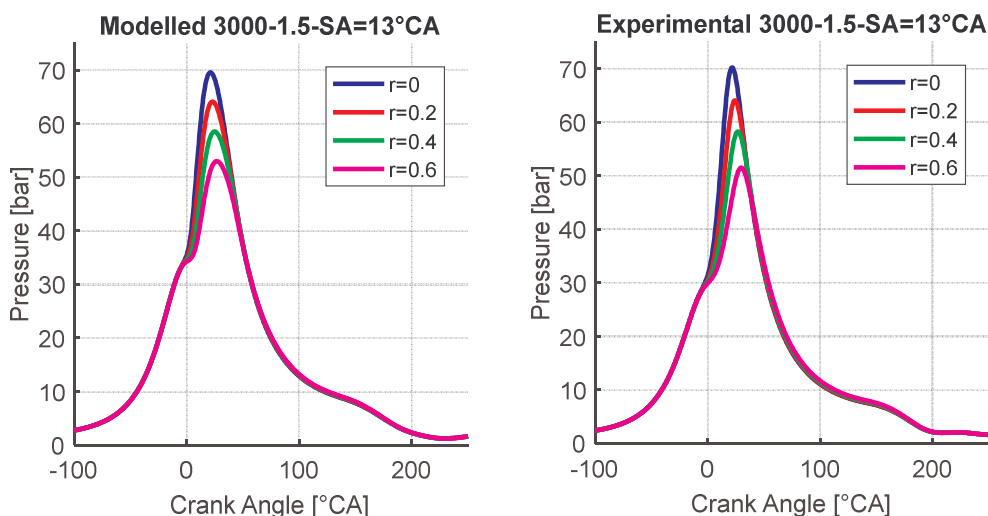


Figure 3.12 - Modelled (left) and measured (right) in-cylinder pressure average cycle, for the same spark advance and different water quantities.

In Figure 3.12, modelled and experimental in-cylinder pressure profiles are reported, for different quantities of injected water. The match between simulation and experimental data is very encouraging, in terms of water quantity variations effects on peak pressure value and position.

### 3.3.2 Experimental results

In this section the experimental results are presented, in terms of indicated quantities and exhaust temperature.

#### 3.2.2.1 Combustion phasing

Figure 3.13 confirms the significant water injection effects on combustion timing: results are very close to those reported in Figure 3.8, and again larger markers identify maximum efficiency points.

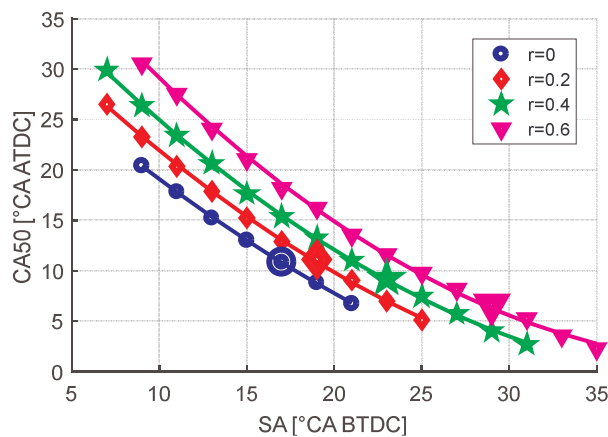


Figure 3.13 - Effect of water injection on combustion phasing. Experimental results are superimposable to model predictions (Figure 3.8): water injection reduces combustion speed and the same CA50%MFB is reached with higher Spark Advance values, as water ratio increases.

Another effect of the water injection, which can be seen also in the model results, is the shift towards lower values of CA50%MFB corresponding to maximum efficiency, as water quantity increases. In Figure 3.13 such value goes from about 11°CA ATDC for  $r = 0$  to about 6°CA ATDC for  $r = 0.6$ .

There is some incongruence between Figure 3.13 and Figure 3.8: the model and the real engine return slightly different values of CA50%MFB for the same Spark Advance. Some further effort is required for the combustion model calibration.

#### 3.2.2.2 Indicated Mean Effective Pressure

Figure 3.14 shows IMEP (Indicated Mean Effective Pressure) values. It results a slight reduction in the maximum IMEP achievable as water is injected, but this is not directly attributable to a reduction in the engine efficiency (as it can be seen in Figure 3.17), but to small variations of engine control parameters and measurement issues.



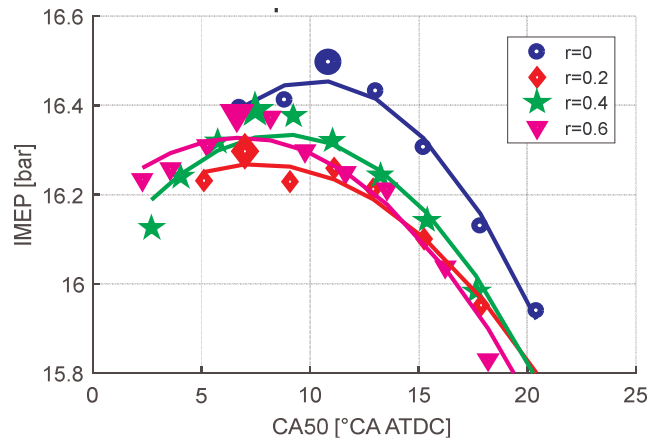


Figure 3.14 - Measured IMEP as a function of CA50%MFB, for different water quantities. Larger markers identify maximum IMEP (and efficiency) points.

### 3.2.2.3 Exhaust temperature

Exhaust temperature reduction, as underlined above, should be evaluated (at least in a first analysis) at maximum efficiency points (highlighted in Figure 3.15 by larger markers). In fact, because of water injection effect on combustion duration, exhaust temperature slightly increases as water mass increases, for the same spark advance angle.

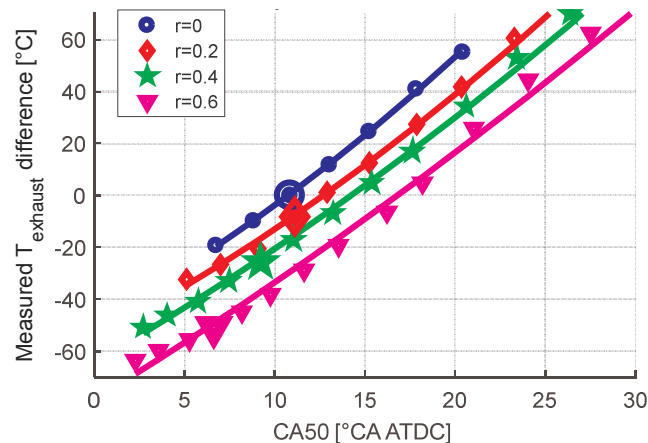


Figure 3.15 - Measured exhaust temperature reduction, depending on water ratio. Bigger markers correspond to MBT. A reduction of about 50°C is achieved with 60% of water ratio.

Supposing the highlighted point for  $r = 0$  as knock limited (i.e., supposing knock intensity to be above the admissible threshold), the achievable gain in terms of exhaust temperature reduction is even greater than 50 °C.

### 3.2.2.4 Knock

Experimental and modelled knock intensities have been superimposed in Figure 3.16, for a direct comparison. What is particularly interesting is the knock intensity reduction for the maximum efficiency points (larger markers) as water mass increases. Inconsistently, for  $r = 0.2$ , knock intensity at maximum efficiency is greater than for  $r = 0.0$ . This is probably due to an ambiguous identification of the maximum efficiency spark advance value.

The selected operating point (1500 rpm, 1,5 bar) is not considered to be knock limited, and further investigation on higher load operation is required. Anyway, a slight reduction on knock intensity as injected water mass increases is verified.

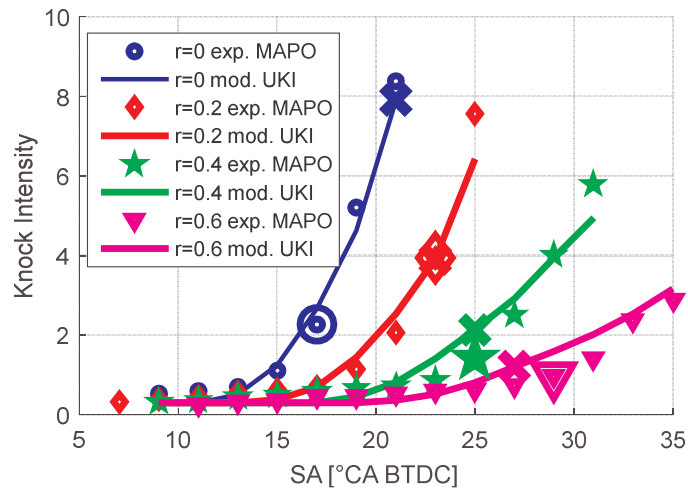


Figure 3.16 - Comparison between measured and modelled knock intensity. Bigger markers correspond to MBT (crosses represent GT ones). Modelled and experimental knock intensities are very superimposable.

Last analysis is on Brake Specific Fuel Consumption (Figure 3.17). Basically, investigated water quantities do not affect engine efficiency, confirming that effectively water enables an extension of the engine operation, with no compromises.

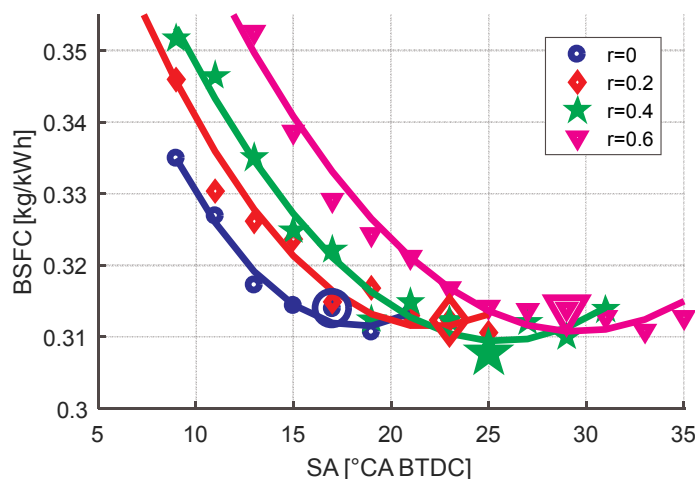


Figure 3.17 - Measured Brake Specific Fuel Consumption trends for different water ratio values. Water injection does not affect maximum achievable efficiency: minimum BSFC value is independent on the water ratio.

### 3.4 Conclusions

This preliminary investigation, both by the model evaluation and by experimental observation, confirms the effectiveness of water injection as a solution to reduce and control exhaust gas temperature and knock tendency. Both these aspects comply with the aim of reducing fuel consumption under high load conditions: on one hand it is possible to reduce or avoid mixture enrichment to limit exhaust temperature, and at the same time water injection can enable operation with maximum efficiency Spark Advance angles, due to the shift of the KLSA (Knock Limit Spark Advance), thus further contributing to exhaust gas temperature reduction.

The feasibility of port water injection implementation as a non-native layout (and so with intrinsically limited possibilities of tuning), which was the primary aim of this work, is confirmed. Operation parameters of the water injection (i.e. injection pressure and phasing) were not optimized at the test bench (and their optimization cannot be executed on the model), so room for improvement is expected. Exhaust temperature and knock intensity reduction achieved with 0.4 – 0.6 values of  $r$ , which are extremely interesting, are probably obtainable with 0.2 – 0.4 mass fractions in an optimized condition.

Water ratio should be as low as possible, to reduce water tank capacity and, mainly, to reduce refill frequency.

### 3.5 References

- [3.1] T. Pauer, M. Frohnmaier, J. Walther, P. Schenk et al., "Optimization of gasoline engines by water injection", 37th INTERNATIONAL VIENNA MOTOR SYMPOSIUM, Wien, 2016.
- [3.2] M. Thewes, H. Baumgarten, J. Scharf, G. Birmes et al., "Water Injection – High Power and High Efficiency Combined", 25th Aachen Colloquium Automobile and Engine Technology, Aachen, 2016.
- [3.3] X. Tauzia, A. Maiboom, S. Rahman Shah, "Experimental study of inlet manifold water injection on combustion and emissions of an automotive direct injection Diesel engine", *Energy*, Volume 35, Issue 9, September 2010, Pages 3628-3639, ISSN 0360-5442, <http://doi.org/10.1016/j.energy.2010.05.007>.
- [3.4] M. De Cesare, N. Cavina, L. Paiano, "Technology Comparison for Spark Ignition Engines of New Generation", submitted to 13th International Conference on Engines & Vehicles, Capri, Italy, 2017.
- [3.5] F. Hoppe, M. Thewes, H. Baumgarten, J. Dohmen, "Water injection for gasoline engines: Potentials, challenges, and solutions", *International Journal of Engine Research*, Volume 17 issue 1, page(s): 86-96, 2016, <https://doi.org/10.1177/1468087415599867>.
- [3.6] Gamma Technology Inc., 2017. GT Gamma Technology. Available at: <https://www.gtisoft.com/gt-suite/gt-suite-overview>.
- [3.7] M. Wenig, M. Grill and M. Bargende, "A New Approach for Modeling Cycle-to-Cycle Variations within the Framework of a Real Working-Process Simulation", SAE Technical Paper 2013-01-1315, 2013, doi:10.4271/2013-01-1315.
- [3.8] F. Millo, L. Rolando, E. Pautasso and E. Servetto, "A Methodology to Mimic Cycle to Cycle Variations and to Predict Knock Occurrence through Numerical Simulation", SAE Technical Paper 2014-01-1070, 2014, doi:10.4271/2014-01-1070.
- [3.9] F. Millo and C. Ferraro, "Knock in S.I. Engines: A Comparison between Different Techniques for Detection and Control", SAE Technical Paper 982477, 1998, doi:10.4271/982477.
- [3.10] N. Cavina, E. Corti, G. Minelli, D. Moro et al., "Knock Indexes Normalization Methodologies", SAE Technical Paper 2006-01-2998, 2006, doi:10.4271/2006-01-2998.
- [3.11] Z. Xudong, W. Yang, X. Shuaiqing et al., "The engine knock analysis - An overview", *Applied Energy*, Volume 92, Pages 628–636, 2012, <http://doi.org/10.1016/j.apenergy.2011.11.079>.

## 4 Knock Model

Today it is more and more important to develop new knock control strategies and new real-time predictive models, in order to enable light-knock working conditions. Knock is a non-deterministic phenomenon and its intensity is typically defined by a non-symmetrical distribution, under fixed operating conditions. A statistical approach is therefore the correct way to study knock features. As highlighted by numerous works [4.1-4.6], a statistical approach to knock phenomenon description has opened new opportunities to develop and improve the modelling activity.

Typically, intrinsically deterministic knock models need to artificially introduce Cycle-to-Cycle Variation (CCV) of relevant combustion parameters, or of cycle initial conditions, to generate different knock intensity values for a given operating condition.

The aim of this activity is to correlate KI (knock intensity) probability curves with mean combustion parameters (like maximum in-cylinder pressure or combustion phase) through an analytical function. In this way, KI distributions can be predicted by a fully deterministic combustion model, ignoring CCV.

The capabilities the water injection of knock mitigation, described in the previous chapter, are taken into account by the proposed model.

Validation is carried out by comparing experimental and calculated KI distributions.

The results of this activity have been presented in “Statistical Analysis of Knock Intensity Probability Distribution and Development of O-D Predictive Knock Model for a SI TC Engine”, SAE Technical Paper 2018-01-0858, doi: 10.4271/2018-01-0858.

### 4.1 Introduction

For a fixed operating condition, knock intensity is strongly influenced by CCV. Several studies [4.7-4.11] demonstrate that a strong relationship exists between MAPO (Maximum Amplitude of Pressure Oscillations) knock intensity index and the charge turbulent motion near the spark plug or the in-chamber temperature distribution. Physical knock models that derive from these studies can be efficiently calibrated to determine the knock onset, the Knock Limited Spark Advance (KLSA) or, more recently, to predict the trend of a MAPO percentile with respect to SA. Extending the analysis, knock models can be generally classified in two main groups:

- Knock models based on chemical kinetic mechanisms
- Knock models based on Arrhenius equation

The first ones simulate pre-flame reactions and consider every sub-reaction that involves several intermediate species, during the combustion process. This kind of models requires significant computational power and for this reason they are typically coupled with zero or quasi-dimensional combustion models. The second category refers to the induction time of the mixture and the knock onset, and its intensity is evaluated by implementing the Arrhenius equation that can be applied to several temperature regions:

$$\tau_i = A_i p^{-n_i} \exp\left(\frac{B_i}{T_u}\right) \varphi^{x_i} \quad (4.1)$$

Where  $p$ ,  $T_u$  and  $\varphi$  are pressure, temperature and equivalence ratio of unburned gas zone, while  $A_i$ ,  $n_i$ ,  $B_i$  and  $x_i$  are constants characteristic of each temperature region. This kind of models establishes the knock onset when the induction time integral (ITI) becomes equal to 1 and calculates the knock index KI using the final value of this parameter [4.12-4.14]. Such models try to define the physics of the knock process and

request lower computational efforts than those that implement chemical reactions. However, as described in the mentioned literature, they need to simulate (and therefore calibrate) the CCV and typically the Arrhenius formula is applied to three different temperature regions. Consequently, their calibration requires extensive experimental data and a big identification effort, due to the large number of calibration parameters.

As it is well-known, knock is a non-deterministic phenomenon and, for this reason, a statistical approach is needed to address the problem. In particular, MAPO probability function (PF) is characterized by a non-symmetrical distribution and it can be well-approximated with log-normal, Weibull or Gamma distributions. The first one is typically preferred, due to its few-parameters formulation and because its analytical equation is easily deducible from the Gaussian one.

In the first part of this chapter, a statistical analysis of knock intensity is carried out: for different values of SA, the probability distributions of an experimental Knock Index (KI) are normalized and self-compared, and a crucial correlation between two MAPO percentiles is found, and the characteristics of some percentiles are highlighted.

Then, a 0-D predictive knock model is proposed, which is based on a new empirical approach to directly calculate a MAPO percentile value (which is the typical approach to evaluate experimental knock intensity) or even its log-normal probability distribution, without the need of simulating CCV, and by calibrating few parameters. In fact, such model uses only two mean combustion parameters to predict knock behaviour. Beyond the calibration effort, accuracy and predictivity, physical models require the calculation of many combustion cycles to extract a single synthetic statistical index (such as a percentile value or the percentage of indexes over a threshold), which is usually the desired output. Instead, the proposed approach totally bypasses the need of a statistical basis, focusing and calculating directly the desired statistical index as a function of static operating parameters. This aspect makes this model very attractive for real-time control-oriented implementation.

## 4.2 Experimental tests

The experiments have been performed on a 4-cylinder GDI TC engine, whose main characteristics are reported in Table 4.1. In-cylinder pressure signals were sampled at 200 kHz and knock intensity was measured using MAPO as index, defined by the following expression:

$$MAPO = \max(|p_f|) \tag{4.2}$$

Where  $p_f$  is the filtered in-cylinder pressure signal: a Butterworth high-pass filter with a 5 kHz cut-off frequency has been used.

Table 4.1 – Engine characteristics.

Displaced volume	1389.9 cc (4 cylinder)
Stroke	75.6 mm
Bore	76.5 mm
Connecting Rod	144 mm
Compression ratio	10:1
Number of Valves	4
Exhaust Valve Open	580° BTDC @ 0.1 mm lift
Exhaust Valve Close	356° BTDC @ 0.1 mm lift
Inlet Valve Open	358° BTDC @ 0.1 mm lift
Inlet Valve Close	132° BTDC @ 0.1 mm lift

The experimental tests consist of several SA sweeps, for given operating conditions. Engine speed and intake manifold pressure were controlled at constant values for each tested point, and the spark advance was increased (typically starting from the calibration value) until knocking conditions were achieved. Some SA sweeps have also been performed for different values of  $\lambda$  and injected water mass, to analyse their effects on knock tendency. In particular, the water mass was controlled through the parameter  $r$ , which is the ratio between water and fuel masses injected per cycle. The detailed description of the experimental port water injection setup (PWI) is described in the previous chapter “3 Water Injection” and in [4.16]. Table 4.2 collects engine speed, intake manifold pressure,  $\lambda$  and  $r$  values for the tested engine points. For each point, a SA sweep has been performed.

Table 4.2 - Experimental engine points. For fixed RPM, intake manifold pressure,  $\lambda$  and  $r$ , a SA sweep has been performed. The nomenclature  $x1:dx:x2$  means that  $\lambda$  and  $r$  values have been varied from  $x1$  to  $x2$  with  $dx$  increment.

Engine point	Speed [RPM]	Load [mbar]	Lambda	Injected water mass ( $r$ )
1	2000	1130	1	0
2	2500	1500	1	0:0.2:0.8
3	2500	1600	1	0:0.2:0.8
4	3000	980	1	0
5	3000	1300	1	0:0.2:0.8
6	3000	1500	1	0:0.2:0.8
7	3000	1700	0.85:0.1:1.15	0
8	3000	2000	1	0
9	4000	1430	0.85:0.1:1.15	0
10	4500	1630	1	0
11	5000	1120	0.85:0.1:1.15	0
12	5000	1490	1	0

### 4.3 MAPO statistical analysis

As already mentioned, MAPO values are characterized by a non-symmetrical distribution and, in particular, log-normal, Weibull and Gamma parametric functions can well describe the statistical MAPO trend. The log-normal PF has the benefit that it is defined by a simple analytical function, which can be easily deduced from the Gaussian one (see the Appendix for more details). In other words, several properties of normal PF can also be used for manipulating and calculating parameters of MAPO curves. This approach gives the possibility to analytically describe the phenomenon in a very concise manner and, therefore, to adapt the function to different cases, by varying few parameters. In this way, a complete characterization of knock intensity can be obtained for a given engine point, and percentiles values can be easily evaluated.

In order to simplify the analysis of MAPO values, the experimental distributions of each cylinder have been compared, and the mean curves (corresponding to the mean cylinder) have been evaluated for each tested engine point.

The cylindrical MAPO probability distributions are typically distinct from each other (Figure 4.1 shows an example of such non-uniformity), probably due to different filling levels, air-to-fuel ratios, temperatures, inlet turbulence conditions, etc.

Figure 4.2 shows mean MAPO PFs for fixed operating conditions and for different spark advance angles. For increasing SA, the mean value and the standard deviation of the MAPO log-normal distribution significantly increase.



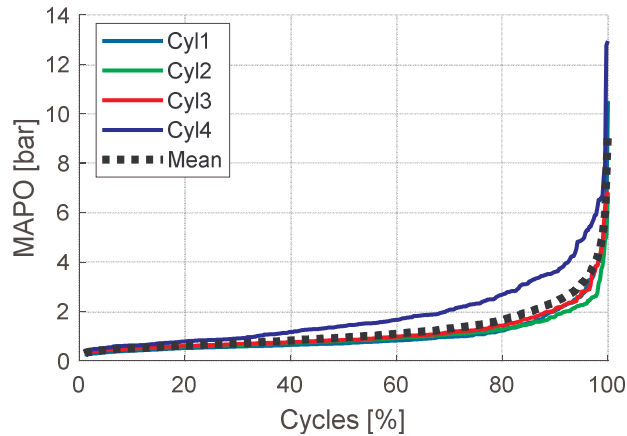


Figure 4.1 - MAPO sorted values for fixed operating conditions. Each cylinder records different MAPO values.

Several studies [4.17, 4.18] explain the similarity of MAPO PFs when they are evaluated for different values of unburned fuel mass fraction at knock onset, after their normalization with respect to a large-enough percentile. In the mentioned literature the 95<sup>th</sup> percentile is taken as reference, but the same result is achievable also with other high-enough percentiles. But, for a wide range of SA variations, normalized MAPO curves are typically too different to identify a unique probability function (Figure 4.3).

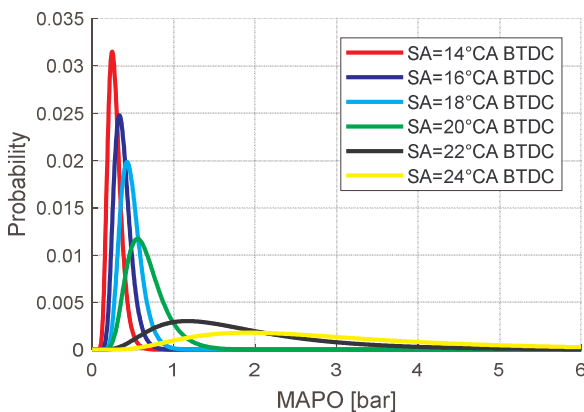


Figure 4.2 - Mean MAPO PFs for different SA.

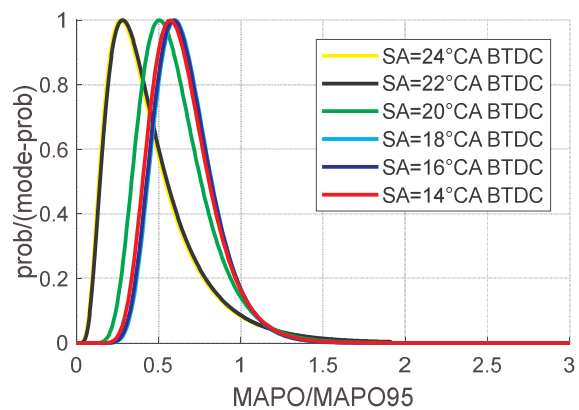


Figure 4.3 - Normalized mean MAPO PFs with respect to 95<sup>th</sup> MAPO percentile (MAPO95) and the mode probability (mode-prob).

Given such preliminary remarks, the proposed approach is to determine the MAPO PF by identifying two percentiles values (one relatively high and one relatively low), and to use them to calculate the mean value and the standard deviation of the log-normal distribution for each engine point. The choice fell on 98<sup>th</sup> (MAPO98) and 50<sup>th</sup> (MAPO50) MAPO percentiles, and a correlation between these values and some mean combustion parameters has been investigated. In particular, the 50<sup>th</sup> and the 98<sup>th</sup> percentiles are well related to each other, as shown in Figure 4.4. However, the same results are obtainable with other percentiles because this choice is somewhat arbitrary, even if, for the higher percentile, a larger value does not work well due to its higher variability. As shown in Figure 4.4, for different operating conditions (different speed, load,  $\lambda$  and  $r$ ) the 50<sup>th</sup> MAPO percentile can be calculated from the 98<sup>th</sup> one (supposing it is known) through a linear equation. In this way, knowing two percentiles, the PF mean value and the standard deviation can be identified and so the whole distribution. Figure 4.4 shows that also for very small values of the 98<sup>th</sup> percentile, the 50<sup>th</sup> one does not fall under 0.2-0.15, due to noise contribution. At the same time, it is possible inferring that when the 98<sup>th</sup> is zero (at the limit) also the 50<sup>th</sup> is null. Therefore, the correlation can be approximated through a linear function that passes through 0, with a small error increase. However, in the next part of the paper the background noise will be related to the engine speed.

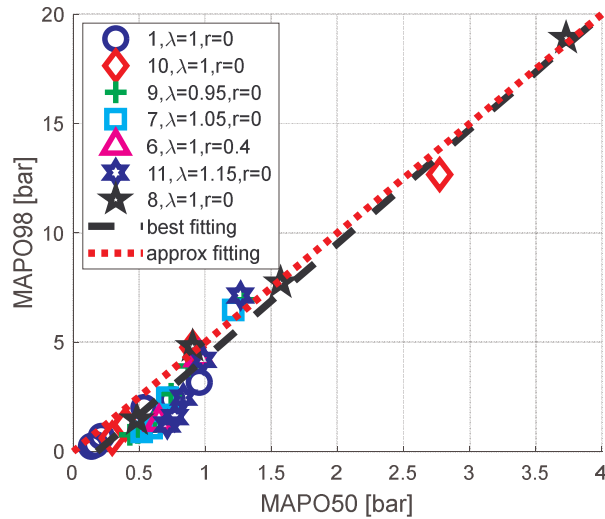


Figure 4.4 - MAPO98 and MAPO50 for some tested engine points. Referring to Table 4.2, the legend provides the number of the engine point, the lambda and the r values.

#### 4.4 Knock model

The proposed methodology involves that MAPO98 is calculated as a parametric function of two mean combustion indexes. An important objective is to use the lowest possible number of parameters to completely define the mentioned function. Some synthetic data, characteristic of engine operating point, are analysed, to identify two independent variables that are well representative of the available chemical energy inside the combustion chamber and how such energy is converted into heat (since load and spark advance are the main control parameters responsible for knock occurrence). As first independent variable the stoichiometric trapped air mass (STAM) has been selected, which is equal to the TAM when the mixture is stoichiometric or rich, and to the ratio between TAM and lambda when the mixture is lean. Equivalently, it could have been considered the stoichiometric fuel mass. This engine load evaluation is more representative of the effective load than intake manifold pressure and it does not derive from a calculation (like the cumulative heat release within the cycle, CHRnet). For this reason, it is a good choice also for a possible real-time implementation. The second independent variable has been chosen between the in-cylinder maximum pressure (Pmax) and the crank angle for which the 50% of fuel mass is burned (CA50) (and other indicated indexes not detailed here). The 98<sup>th</sup> MAPO percentile has been evaluated as a power function of all these parameters, in order to select the most robust one. In Figures 4.5 and 4.6, MAPO98 is evaluated with respect to the investigated combustion indexes for different engine speeds, loads, *lambda* and injected water masses. In Figure 4.5 it is possible to see that the variation of these parameters impacts on the values of maximum pressure for which a given MAPO98 is recorded, but it does not influence the shape of the relationship, and this is then the feature that is explored for a wide range of operating conditions. A similar behaviour can be observed in Figure 4.6, where MAPO98 is reported as a function of CA50.

The trends represented in Figures 4.5 and 4.6 can be interpolated with a power function, like the one defined by Equation (4.3):

$$y = a x^b + c \quad (4.3)$$

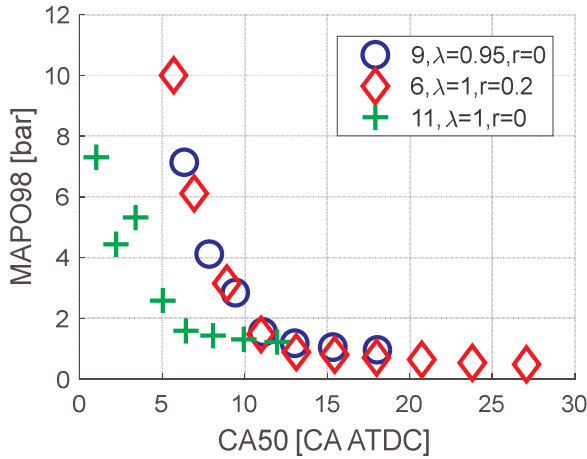


Figure 4.5 - MAPO98 as a function of maximum in-cylinder pressure for some tested engine points.

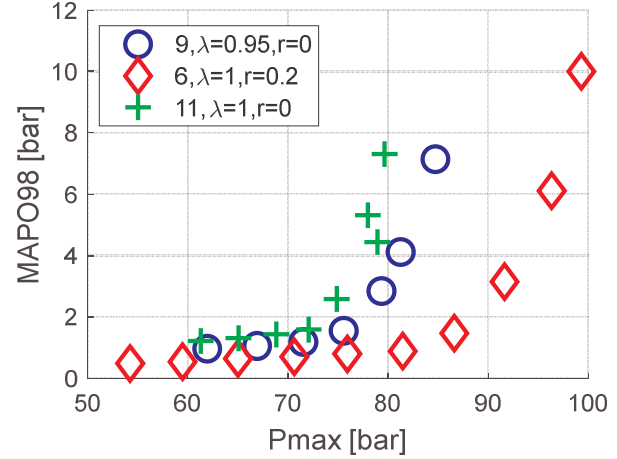


Figure 4.6 - MAPO98 as a function of and CA50 for some tested engine points

Where  $y$  is the 98<sup>th</sup> MAPO percentile and  $x$  the maximum in-cylinder pressure or the CA50. To identify the optimum couple of independent variables (STAM-Pmax or STAM-CA50) to fit the 98<sup>th</sup> percentile trend, different power functions of STAM-Pmax and STAM-CA50 are investigated, and the mean percentage error (one for each SA sweep) between experimental and calculated MAPO98 is evaluated. Equation (4.4) resulted as the five-parameters function that better fits experimental data:

$$mapo98 = (a x^b) y^{(c x+d)} + e \quad (4.4)$$

Where  $x$  is STAM and  $y$  is Pmax or CA50. It should be observed that Equations (4.3) and (4.4) do not represent physical relationships between the selected parameters. They have been chosen since they mathematically represent the best fit between MAPO98, STAM and CA50 or Pmax. Table 4.3 shows the mean percentage relative errors between experimental MAPO98 and values calculated with Equation (4.4). The error is calculated with the following equation:

$$err = \left| \frac{MAPO98 - mapo98}{MAPO98} \right| 100 \quad (4.5)$$

Where  $MAPO98$  is the experimental 98<sup>th</sup> MAPO percentile and  $mapo98$  is the one calculated with (4.4). To evaluate the errors, the optimization of five parameters is carried out for each considered variables couple. Table 4.3 reports both the mean relative error (%) and the mean absolute error (bar) between the calculated and the experimental knock level, both considering as independent variables STAM-Pmax and STAM-CA50. The table shows that best results are achieved by considering STAM-Pmax, even if the two parameters are not independent (Pmax depends on STAM, but it hides the information about CA50). To close the gap between MAPO98-Pmax curves, caused by different values of  $\lambda$  and injected water masses, some calibration parameters are added to the relationship defined by Equation (4.4). In this way, such curves are shifted and collapse in a unique one, and the effects of the mentioned variables are directly captured by the model.

Table 4.3 - Absolute and relative mean MAPO98 errors calculated using Pmax (2nd and 3rd column) and CA50 (4th and 5th column) as y variable in (4.4). For each column, the minimum error is highlighted in blue, the maximum one in orange.

Engine point ( $\lambda=1, r=0$ )	Error with STAM- Pmax [%]	Absolute error with STAM-Pmax [bar]	Error with STAM- CA50 [%]	Absolute error with STAM-CA50 [bar]
1	11.2	0.14	31.4	0.43
4	8.7	0.03	15.3	0.05
7	3.8	0.08	45.5	1.02
8	5.5	0.24	68.8	3.11
9	7.9	0.16	20.7	0.43
10	11.6	0.26	20.5	0.46
11	11.5	0.29	23.9	0.60
12	4.4	0.11	72.6	1.96

#### 4.4.1 Engine speed variation

Background noise contribution on MAPO98 is visible for non-knocking conditions and it is dependent on engine speed. Non-zero values of MAPO for non-knocking conditions are caused by combustion roughness (i.e. combustion speed). Consequently, noise increases with engine speed (the higher the engine speed, the higher the turbulence and so the time-based combustion speed). This effect can be observed for example in Figures 4.5 and 4.6: the MAPO98 value corresponding to the sharp derivative variation of the curve, is increasing from test 6 to 9 to 11 (corresponding respectively to 3000, 4000 and 5000 RPM). For the same reason, in non-knocking conditions, MAPO98 slightly increases with spark advance. Engine speed contribution can be described by the value of the parameter  $c$  of Equation (4.3). Such parameter is supposed to have a linear dependence with engine speed, which can be directly transferred to the parameter  $e$  in Equation (4.4):

$$e = RPM \ ESm \quad (4.6)$$

Where  $ESm$  is the Engine Speed Multiplier and its values (obtained by fitting independently every spark-sweep for all the tested operating conditions) resulted all very close to  $1e-4$ . Therefore, if MAPO98 and MAPO50 are reduced of  $RPM/1e4$ , all curves start approximately from the same value. At the same time, the  $ESm$  value can be optimized to maximize the linear dependence between scaled MAPO98 and MAPO50, and its identification can be carried out through the minimization of the sum of squared errors calculated with the following equation:

$$se = \sum (g(MAPO98 - RPM \ ESm) - (MAPO50 - RPM \ ESm))^2 \quad (4.7)$$

In Equation (4.7),  $se$  is the sum of squared errors and  $g$  is the inverse of the slope of the red dashed line shown in Figure 4.7. The optimum  $ESm$  value resulted in  $8.3e-5$ , and it is used for the following considerations. Such value confirms also that  $1e-4$  is a good compromise between describing the engine speed effect on the MAPO distribution and maximizing the correlation between the two percentiles. In this way, Equation (4.4) can be rewritten as follows:

$$m98 = (a \ STAM^b) \ Pmax^{(c \ STAM+d)}$$

$$m98 = mapo98 - RPM \ ESm \quad (4.8)$$

Where  $a$ ,  $b$ ,  $c$ , and  $d$  are the four calibration parameters and  $m98$  is the calculated MAPO98, scaled of the engine-speed dependent noise contribution. Equation (4.8) has been used to fit experimental data and to map the scaled MAPO98 trend. The optimum calibration parameters set has been defined by minimizing the root-mean-square of the errors (RMSEs) between experimental percentiles and calculated ones, and it is reported below:

- $ESm = 8.3e-5$  [bar/rpm]
- $a = 1.07e-27$  [ $kg^{-1}$ ]
- $b = -11.53$  [ ]
- $c = 4.40$  [ $kg^{-1}$ ]
- $d = 10.41$  [ ]

It is then convenient to define these quantities to better understand the following figures:

$$M50 = MAPO50 - RPM ESm$$

$$M98 = MAPO98 - RPM ESm$$

(4.9)

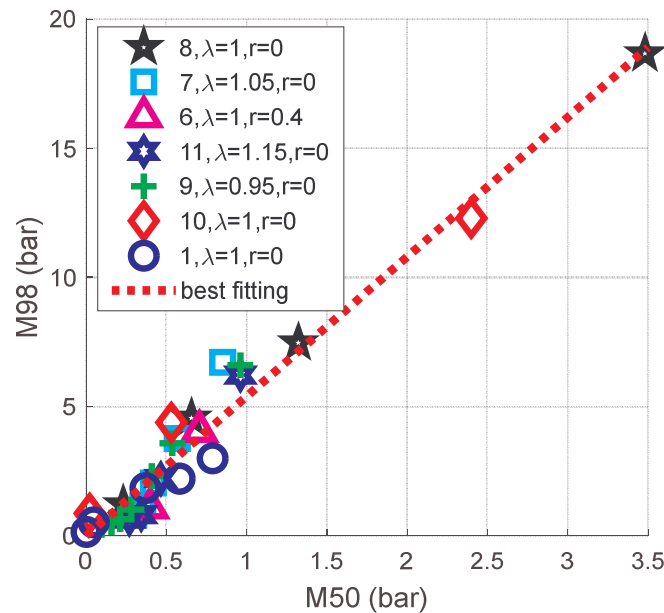


Figure 4.7 - Correlation between scaled MAPO98 (M98) and scaled MAPO50 (M50) with  $ESm$  equal to  $8.3e-5$ .

Figure 4.8 reports M98 values for three different operating points. Instead, Figure 4.9 represents the m98 map, expressed as a function of STAM and  $P_{max}$  according to the Equation (4.8), and the experimental M98 values, for different SA sweeps. This figure is also useful to highlight the reduced number of engine points requested to calibrate the knock model (this element can be deduced also from the low number of calibration parameters of Equation (4.8), which defines a smooth surface in the STAM- $P_{max}$  plane). Moreover, in Figure 4.9 a part of the map has been neglected because, for each STAM value, it exists a maximum theoretical  $P_{max}$  value. Figure 4.10 illustrates the absolute error of the data shown in Figure 4.9 (calculated and measured MAPO98, for different operating conditions and different SA). The maximum error is generally committed in correspondence with the brusque change in the curves slope.

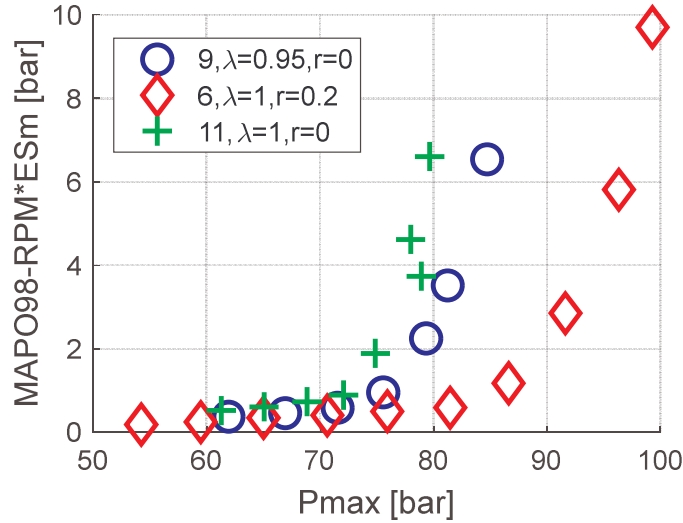


Figure 4.8 - Experimental values of MAPO98 curves reduced of RPM\*ESm.

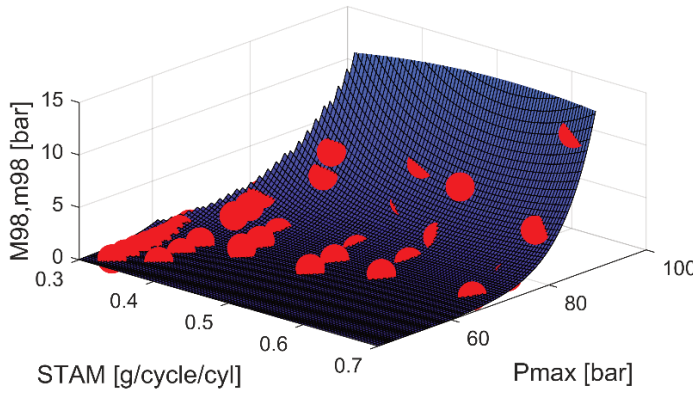


Figure 4.9 - m98 map compared with experimental data (M98, red circles).

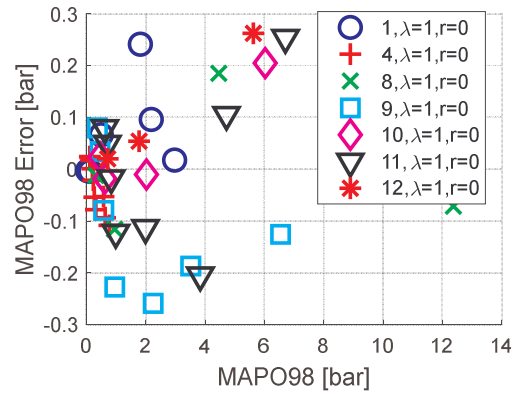


Figure 4.10 - MAPO98 absolute errors for engine points collected in the m98 map.

#### 4.4.2 MAPO50 Calculation

As mentioned above, the calculation of the scaled 50<sup>th</sup> MAPO percentile can be carried out starting from Equation (4.8), through a linear correlation. The *m50* calculation can be carried out by introducing only one new parameter in (4.8). The expression of *m50* can therefore can be defined by Equation (4.10):

$$m50 = g m98 \tag{4.10}$$

In this case the optimal value for parameter *g* is 0.17, which is the inverse of the slope of the fitting line found in Figure 4.7.

The absolute and the relative mean error between experimental and calculated 50<sup>th</sup> percentiles have then been evaluated, and the results are collected in Table 4.4. Even if errors are slightly greater than those committed in the evaluation of MAPO98 (because of the non-perfect correlation between the two percentiles, see Figure 4.7), they remain widely acceptable. Figure 4.11 represents the *m50* map obtained by using Equation (4.10) and Figure 4.12 collects the absolute errors for SA sweeps represented in the *m50* map. As for Figure 4.9, a part of the map has been neglected to exclude regions that are out of the operating range. The low number of parameters is the main cause of such errors. Moreover, MAPO50 and MAPO 98 curves are approximately linear in the lower range, and therefore the model exponential shape tends to overestimate the values corresponding to incipient knock conditions (this is clearly visible in the



following Figures 4.14 and 4.15). However, these errors are absolutely acceptable considering their limited magnitude and that they mainly affect the smaller MAPO98 and MAPO50 values.

Table 4.4 - Absolute and relative mean error between experimental and calculated MAPO50. The minimum mean error is highlighted in blue, the maximum one in orange.

Engine point ( $\lambda=1, r=0$ )	Relative error [%]	Absolute error [bar]
1	11.7	0.03
4	14.8	0.01
7	9.0	0.08
8	15.4	0.12
9	7.3	0.02
10	10.3	0.03
11	7.5	0.03
12	8.1	0.02

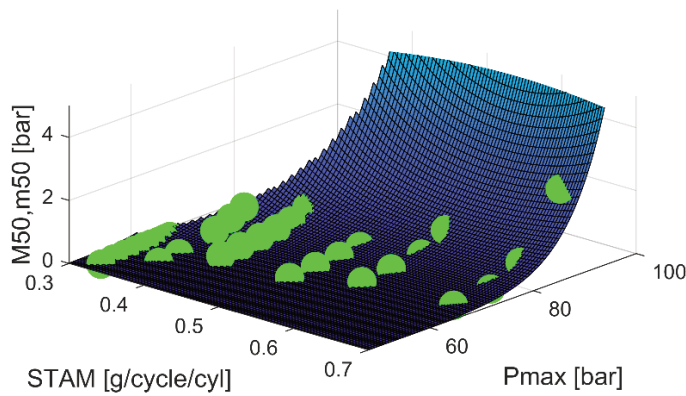


Figure 4.11 - m50 map compared with experimental points collected (M50, green circles).

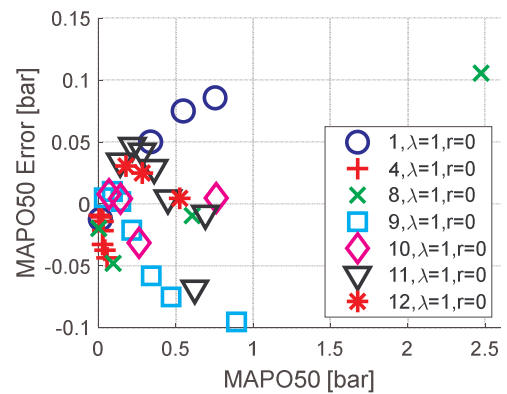


Figure 12 - MAPO50 errors for engine points in the m50 map.

#### 4.4.3 Lambda Multiplier

The mixture enrichment (generally used to lower exhaust gas temperature) can be used to suppress knock (on the contrary, mixture leaning is generally a knock enhancer). The effect of the mixture composition can be seen as a mere translation of M98 and M50 curves along the Pmax axis. Such behaviour is visible in Figure 4.13.

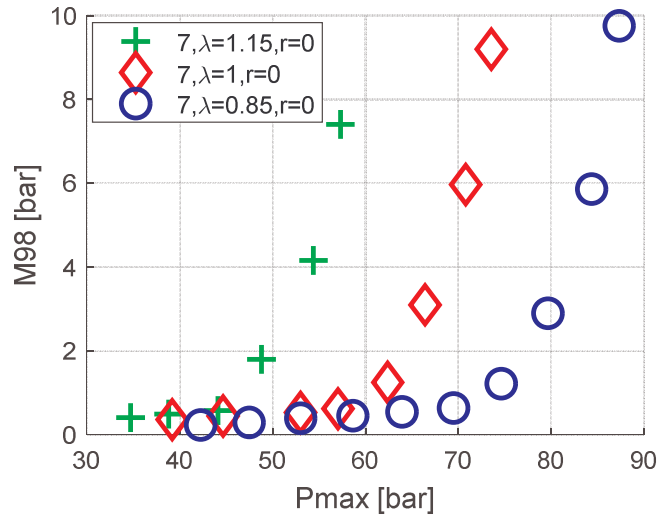


Figure 4.13 - M98 curves for fixed operating conditions and for different lambda values.

To adapt the  $m98$  model, a corrective term depending on  $lambda$  has been added to  $Pmax$ , as shown in Equation (4.11). For three engine points, the SA sweeps are carried out for different values of  $lambda$  and these data have been used to calibrate the multiplier that models these effects on MAPO percentiles. Equation (4.11) represents the correlation that was identified to model such dependencies ( $m50$  is calculated with the Equation (4.10)):

$$m98 = (a STAM^b) (Pmax + ((\lambda - 1)lm))^{(c STAM+d)} \quad (4.11)$$

Where:

- $\lambda$  is lambda
- $lm$  is the lambda multiplier and it is the calibration parameter. Its optimized value is -18.43.

In Figure 4.14, three experimental sets are compared with the curves calculated with (4.11), for three different engine points and  $lambda$  values.

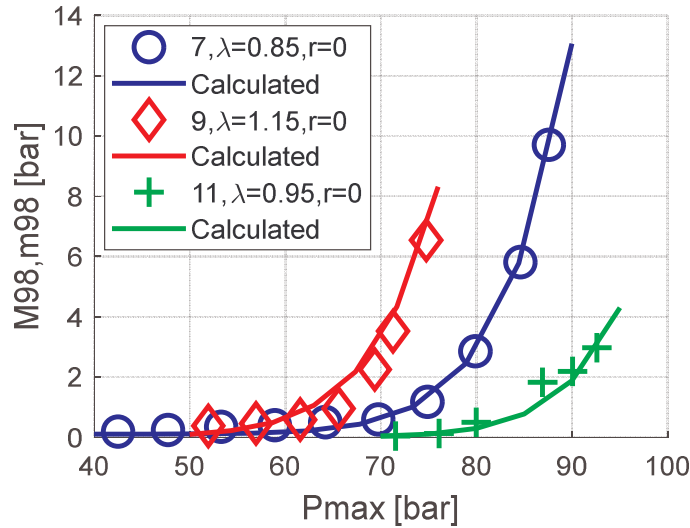


Figure 4.14 - Experimental (M98) and calculated (m98) MAPO98 for three different engine points and lambda values.

Table 4.5 shows the mean percentage errors estimated between experimental and calculated MAPO98 and MAPO50 for each *lambda* value. Also in this case, encouraging results have been obtained.

Table 4.5 - Mean percentage errors between experimental and calculated MAPO98-50, for different lambda values.

Engine point	lambda	MAPO98 error [%]	MAPO50 error [%]
7	0.85	10.7	10.0
	0.95	11.5	16.7
	1.05	12.0	9.9
	1.15	6.3	18.1
9	0.85	11.1	11.2
	0.95	10.8	9.3
	1.05	4.9	10.0
	1.15	4.4	14.4
11	0.85	8.9	12.6
	0.95	14.5	11.2
	1.05	7.0	16.98
	1.15	9.8	14.0

#### 4.4.4 Water Injection Multiplier

The same method is applied to compensate the effects generated by water injection (WI) and another calibration parameter is added to (4.11), which evolves in (4.12) (*m*50 is calculated with the Equation (4.10)):

$$m98 = (a STAM^b) (Pmax + ((\lambda - 1)lm) + (r wm))^{(c STAM+d)} \quad (4.12)$$

Where

- *r* is the ratio between injected water and fuel mass per cycle
- *wm* is the water injection multiplier. Its optimized value resulted in 16.6.

Figure 4.15 shows the comparison between experimental and calculated M98 for different values of  $r$ .

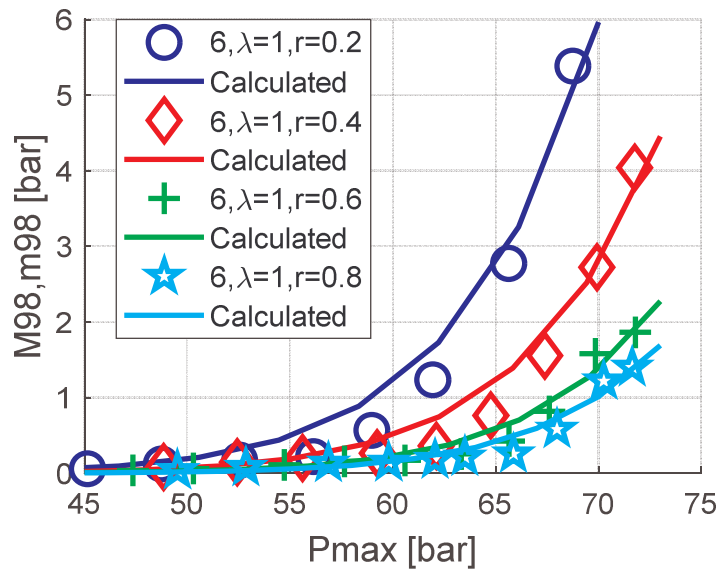


Figure 4.15 - Experimental ( $M_{98}$ ) and calculated ( $m_{98}$ ) MAPO98 for four different values of  $r$ .

Table 4.6 - Mean percentage errors between experimental and calculated MAPO98-50, when  $r$  changes.

Engine point	$r$	MAPO98 error [%]	MAPO50 error [%]
2	0.0	7.5	15.7
	0.2	12.8	21.6
	0.4	11.6	11.8
	0.6	6.14	12.1
	0.8	10.0	19.4
3	0.0	7.9	13.0
	0.2	15.5	16.0
	0.4	9.7	10.3
	0.6	12.3	18.8
	0.8	8.0	15.4
5	0.0	13.2	19.4
	0.2	9.1	12.1
	0.4	13.8	18.6
	0.6	14.3	16.1
	0.8	15.0	18.3
6	0.0	11.4	17.1
	0.2	6.2	12.3
	0.4	8.7	9.6
	0.6	16.9	20.2
	0.8	7.8	11.9

As in the previous paragraph, Table 4.6 collects mean percentage errors between experimental and calculated MAPO98 and MAPO50 for each value of  $r$ . Also the effects produced by WI can be predicted with limited errors.

## 4.5 Knock Model Results

### 4.5.1 Log-normal PDF Parameters

The following step is the calculation of the characteristic parameters of MAPO log-normal probability function. In this way, the entire distribution is known, for a fixed operating condition. The mean value ( $\mu$ ) and the standard deviation ( $\sigma$ ) are easily obtainable from two generic quantiles (such as 50<sup>th</sup> and 98<sup>th</sup> percentiles), using properties of Gaussian distributions. The final equations are the following (see the Appendix for more details):

$$\mu = \ln(m50 + RPM ESm) \quad (4.13)$$

$$\sigma = \frac{\ln(m98 + RPM ESm) - \ln(m50 + RPM ESm)}{\phi^{-1}(98)} \quad (4.14)$$

Where:

- $\mu$  is the mean value of MAPO log-normal distribution
- $\sigma$  is the standard deviation of MAPO log-normal distribution
- $\phi^{-1}(98)$  is the value assumed by the 98<sup>th</sup> percentile of the cumulative density function (CDF) of the standardized normal distribution  $Z$ , which is equal to 2.0057

Once  $\mu$  and  $\sigma$  are known, the MAPO log-normal distribution is defined. At this point, the distribution can be used, for example, to randomly generate knock intensities (if the stochastic behaviour simulation is needed), associated with the current engine operation, in a 0/1-D model, as explained in the next section. Moreover, it is also possible to calculate every desired percentile, other than the 50<sup>th</sup> or the 98<sup>th</sup>. Finally, the whole distribution can be compared to the experimental one to validate the calculation.

Some validation tests have then been run to verify the model predictivity (Table 4.7). As shown in Figure 4.16, the predicted (by the Knock Model) and the experimental MAPO sorted values are adequately superimposed for all validation engine points. Such points are characterized by lambda equal to 1 and  $r$  equal to 0.

Table 4.7 - Experimental engine points used for validation of knock model.

Engine point	Speed [RPM]	Load [mbar]	SA
13	2250	1210	28
14	3500	1200	30
15	3500	1810	12
16	4500	1110	34
17	4500	1850	12

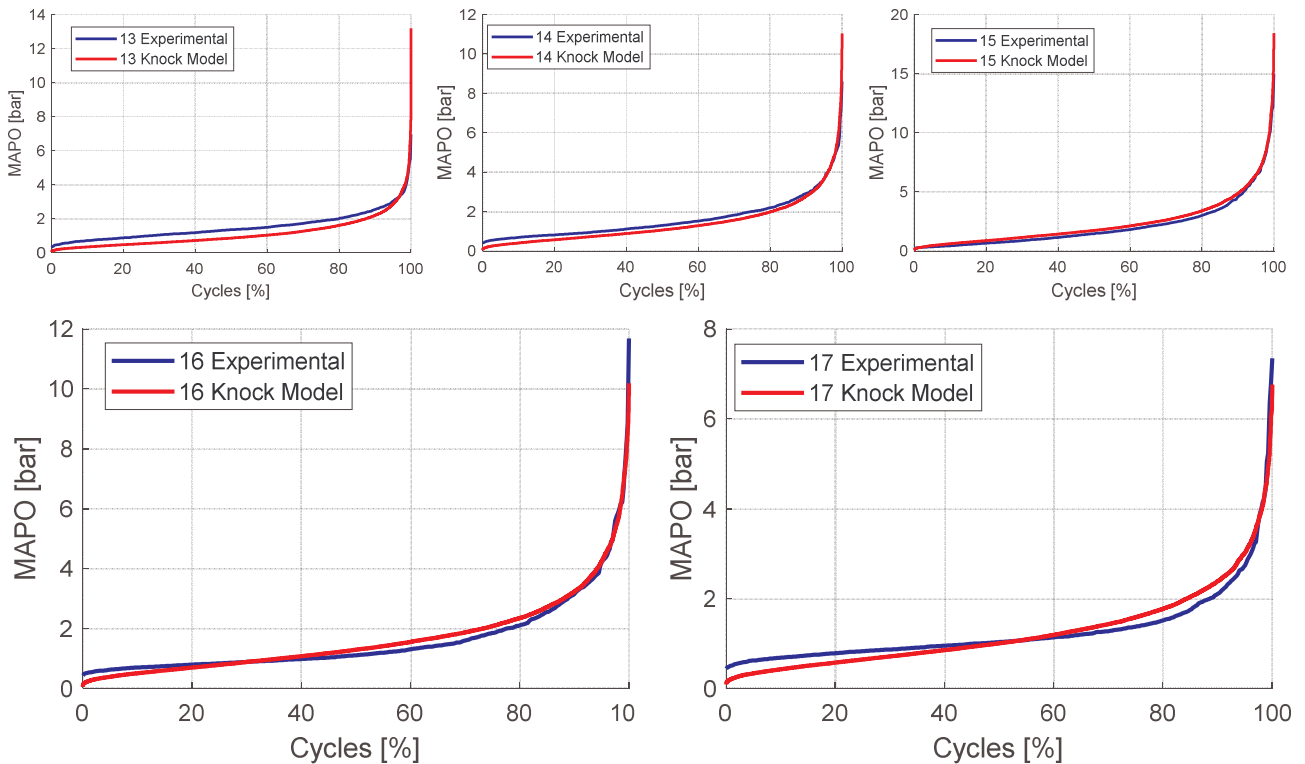


Figure 4.16 - Comparison between measured and calculated MAPO cumulative distributions for points 13 to 17.

## 4.6 Conclusions

In this activity, knock behaviour is empirically described for a given engine point, without the introduction of a CCV model. Two mean combustion indexes (stoichiometric trapped air mass and in-cylinder maximum pressure) are used and only five calibration parameters have to be optimized in order to calculate MAPO<sub>98</sub> and MAPO<sub>50</sub> in stoichiometric conditions. This methodology allows obtaining two MAPO percentiles by considering two mean combustion variables (measured or modelled) and only 5 parameters to be identified, and it can therefore be calibrated in an extremely fast and easy way. The model errors are relatively small (the maximum is about 15 %) and the model is also easily adaptable to different operating conditions (two additional parameters have been added to consider the effects of lambda and injected water mass variations on the MAPO percentiles). The equations for deducing mean value and standard deviation of MAPO log-normal probability distribution from two percentiles have been introduced and the experimental and calculated cumulative PFs have been compared over five validation points, showing a satisfactory agreement between the curves.

## 4.7 References

- [4.1] Kim, K. and Gandhi, J., "Preliminary Results from a Simplified Approach to Modelling the Distribution of Engine Knock," SAE Technical Paper 2012-32-0004, 2012.
- [4.2] Peyton Jones, J., Muske, K., Frey, J., and Scholl, D., "A Stochastic Knock Control Algorithm," SAE Technical Paper 2009-01-1017, 2009.
- [4.3] Peyton Jones, J., Spelina, J., and Frey, J., "Control-Oriented Knock Simulation," SAE Int. J. Engines 9(2):2016, doi:10.4271/2016-01-0821.



- [4.4] Spelina, J., Peyton Jones, J., and Frey, J., "Recent Advances in Knock Analysis, Simulation, and Control," SAE Int. J. Engines 7(2):2014, doi:10.4271/2014-01-1349.
- [4.5] Shahlari, A. and Ghandhi, J., "Pressure-Based Knock Measurement Issues," SAE Technical Paper 2017-01-0668, 2017, doi:10.4271/2017-01-0668.
- [4.6] Lonari, Y., Polonowski, C., Naber, J., and Chen, B., "Stochastic Knock Detection Model for Spark Ignited Engines," SAE Technical Paper 2011-01-1421, 2011.
- [4.7] Wenig, M., Grill, M. and Bargende, M., "A New Approach for Modelling Cycle-to-Cycle Variations within the Framework of a Real Working-Process Simulation," SAE Int. J. Engines 6(2):2013, doi:10.4271/2013-01-1315.
- [4.8] D'Adamo, A., Breda, S., Fontanesi, S., and Cantore, G., "A RANS-Based CFD Model to Predict the Statistical Occurrence of Knock in Spark-Ignition Engines," SAE Int. J. Engines 9(1):2016, doi:10.4271/2016-01-0581.
- [4.9] J.C. Livengood, P.C. Wu, "Correlation of auto-ignition Phenomena in Internal Combustion Engines and Rapid Compression Machines", 5<sup>th</sup> Symposium (International) on Combustion, pp.347-356, 1957.
- [4.10] A.M. Douaud and P.Eyzat, "Fou-Octane-Number Method for Predicting the Anti-Knock Behavior of Fuels and Engines", SAE Technical Paper Series, SAE 780080, 1978.
- [4.11] Worret, R., Bernhardt, S., Schwarz, F., and Spicher, U., "Application of Different Cylinder Pressure Based Knock Detection Methods in Spark Ignition Engines," SAE Technical Paper 2002-01-1668, 2002.
- [4.12] Kalghatgi, G., Algunaibet, I., and Morganti, K., "On Knock Intensity and Superknock in SI Engines," SAE Int. J. Engines 10(3):2017, doi:10.4271/2017-01-0689.
- [4.13] Corti, E., Forte, C., Bianchi, G., and Zoffoli, L., "A Control-Oriented Knock Intensity Estimator," SAE Int. J. Engines 10(4):2219-2229, 2017.
- [4.14] Millo, F., Rolando, L., Pautasso, E., and Servetto, E., "A Methodology to Mimic Cycle to Cycle Variations and to Predict Knock Occurrence through Numerical Simulation," SAE Technical Paper 2014-01-1070, 2014, doi:10.4271/2014-01-1070.
- [4.15] Gamma Technology Inc., 2017. GT Gamma Technology.
- [4.16] Cavina, N., Rojo, N., Businaro, A., Brusa, A. et al., "Investigation of Water Injection Effects on Combustion Characteristics of a GDI TC Engine," SAE Int. J. Engines 10(4):2017, doi:10.4271/2017-24-0052.
- [4.17] Ghandhi, J. and Kim, K., "A Statistical Description of Knock Intensity and Its Prediction," SAE Technical Paper 2017-01-0659, 2017, doi:10.4271/2017-01-0659.
- [4.18] Kim, K.S., "Study of Engine Knock Using a Monte Carlo Method," thesis, University of Wisconsin-Madison, 2015.

## 4.8 Appendix

The log-normal probability density function can be easily obtained from the associated Gaussian distribution:

$$Y(\mu, \sigma) = e^{(X(\mu, \sigma))}$$

(4.15)

Where:

- $Y$  is the log-normal distribution with mean value  $\mu$  and standard deviation  $\sigma$
- $X$  is the associated normal distribution with mean value  $\mu$  and standard deviation  $\sigma$

Therefore, all normal distributions can be calculated starting from the standardized normal distribution  $Z$  with mean value 0 and standard deviation 1:

$$X(\mu, \sigma) = \sigma Z(0,1) + \mu \quad (4.16)$$

Replacing the (4.16) in (4.15):

$$Y(\mu, \sigma) = e^{(\sigma Z + \mu)} \quad (4.17)$$

For its particular properties, the log-normal distribution is typically used to describe MAPO values and it is preferred to other more complex expressions. These properties can be used to calculate the mean value and the standard deviation of a log-normal distribution from two percentiles. If two percentiles of normal distribution  $X$  are given, it is possible to write:

$$P(X < x_1) = p_1 \quad (4.18)$$

$$P(X < x_2) = p_2 \quad (4.19)$$

Where:

$P$  indicates the probability

$x_i$  is the value of the percentile

$p_i$  is the value of the percentage of the percentile

Replacing (4.16) in (4.18) and (4.19):

$$P(\sigma Z + \mu < x_i) = p_i \quad (4.20)$$

Rearranging the above equation it is possible to write:

$$P\left(Z < \frac{x_i - \mu}{\sigma}\right) = p_i \quad (4.21)$$

$$p_i = \phi\left(\frac{x_i - \mu}{\sigma}\right) \quad (4.22)$$

In which  $\phi$  is the CDF of standardized normal distribution  $Z$ . By reversing Equation (4.22), a system of two equation in two variables is defined:

$$\phi^{-1}(p_i) = \frac{x_i - \mu}{\sigma}$$

(4.23)

$$\begin{cases} \phi^{-1}(p_1)\sigma + \mu = x_1 \\ \phi^{-1}(p_2)\sigma + \mu = x_2 \end{cases}$$

(4.24)

Solving the first equation for mean value, replacing it in the second one, and recalling Equation (4.15):

$$\begin{cases} \mu = \frac{x_1 \phi^{-1}(p_2) - x_2 \phi^{-1}(p_1)}{\phi^{-1}(p_2) - \phi^{-1}(p_1)} \\ \sigma = \frac{x_2 - x_1}{\phi^{-1}(p_2) - \phi^{-1}(p_1)} \end{cases}$$

For a normal PDF

(4.25)

$$\begin{cases} \mu = \frac{\ln(x_1) \phi^{-1}(p_2) - \ln(x_2) \phi^{-1}(p_1)}{\phi^{-1}(p_2) - \phi^{-1}(p_1)} \\ \sigma = \frac{\ln(x_2) - \ln(x_1)}{\phi^{-1}(p_2) - \phi^{-1}(p_1)} \end{cases}$$

For a log-normal PDF

(4.26)

In particular, if  $x_1$  is the 50<sup>th</sup> percentile and  $x_2$  is the 98<sup>th</sup>,  $\phi^{-1}(p_1) = 0$  and  $\phi^{-1}(p_2) = 2.0057$ , and the final relationship is defined by:

$$\begin{cases} \mu = \ln(x_1) \\ \sigma = \frac{\ln(x_2) - \ln(x_1)}{2.0057} \end{cases}$$

(4.26)

## Conclusions

The thesis illustrates the principal activities carried out along my 3 years long PhD course, focused on the control of knocking operation in spark-ignited engines. The topic is crucial and a proper understanding of the phenomenon is requested by the automotive industry to comply with the imposed limits on the fuel economy (and emissions), to design and produce more and more advanced and efficient powertrains. The document describes different and complementary approaches to deal with knock: from the definition of the knock levels to be applied, depending on the desired reliability, passing through the analysis of the water injection capabilities to suppress knock, up to measuring and modelling techniques to estimate knock intensity.

The proposed damage model is, in my opinion, a novel and important contribution to the calibration procedures and control strategies, since it introduces new parameters and quantities, such as piston temperature and eventually piston material properties, which are usually not considered when speaking of knock intensity. Furthermore, the topic is slightly discussed in literature. Apart from the specific results, which are not necessarily easy to transfer to different engines, the methodology and the qualitative results is what should be of interest and that can be used and applied indiscriminately.

The other activities, regarding ion current signal, water injection and knock modelling, involve spread topics, but the qualitative results and the concepts are still of interests for the application field. Once the desired knock level is established, for example by using the described knock damage model, it has to be pursued by the engine control unit. The possibility of measuring the knock intensity and the combustion phasing in all the cylinders with a trusted sensing system is of great interest and the feasibility of adopting ionization current signal to control the combustion in closed-loop has been demonstrated. A pure closed-loop strategy is not able to properly control the combustion process during transient conditions, so a model able to predict knock intensity is necessary to realize the desired conditions. The proposed knock model has a simple approach but it showed the desired behaviour and high implementability. Moreover, the methodologies used to take into account air-fuel ratio and water quantity can still be applied to other boundary, control parameters and adaptive corrections (learned from the combustion feedback) to improve robustness and accuracy.

Water injection effectiveness in reducing both knock intensity and exhaust temperature has been evaluated, with particular focus on the involved water quantity, to be able to quantify the cost-benefit ratio, since water consumption is the principal concern for this technology.